REDUCED ORDER PHYSICS BASED MODEL OF ELECTROCHEMICAL DOUBLE LAYER CAPACITORS

by

AL MUNDY

B.S.Cp.E., Clemson University, 1996

M.S.Cp.E., Syracuse University, 1999

A dissertation submitted to the Graduate Faculty of the

University of Colorado Colorado Springs

in partial fulfillment of the

requirements for the degree of

Doctor of Philosophy

Department of Electrical and Computer Engineering

2015

This dissertation for the Doctor of Philosophy degree by

Al Mundy

has been approved for the

Department of Electrical and Computer Engineering

by

_____

Gregory L. Plett, Chair

_____

M. Scott Trimboli

_____

Carlos Araujo

_____

Albert L. Batten

_____

Thottam Kalkur

_____

Date

iii

Mundy, Al (Ph.D., Engineering—Electrical Engineering)

Reduced Order Physics Based Model of Electrochemical Double Layer Capacitors

Dissertation directed by No adviser title defined Gregory L. Plett

This dissertation investigates the development and use of a reduced-order model of an Electrochemical Double Layer Capacitor. Electric vehicles have a requirement to source high currents when accelerating and to sink high currents during regenerative braking. The high levels of current during these times can potentially damage lithium-ion batteries. Using hybrid systems including *supercapacitors*, or *ultracapacitors*, is one method to mitigate the high current surges without damaging the lithium-ion cells. Designing such systems requires accurate models of both lithium-ion cells and supercapacitors; and while the study of lithium-ion cells has been in the forefront of research, the study of electrochemical cells has only recently become popular. Physics-based models can provide high accuracy of terminal conditions, as well as providing insight to the internal state, or condition of the cell. This type of model is generally mathematically complex and not as easily simulated as a circuit model. Therefore, reduced-order models have been developed that simplify the simulations, and for lithium-ion cells, have been shown to be quite useful. Physics-based models for supercapacitors are not new, but they are not nearly as common and the approach taken in this dissertation is new. The focus is on the development and implementation of reduced-order model that looks like a circuit-based mode. The result is (1) accurate, (2) simple to use, and (3) easily modifiable for application to real-world devices that can change from system to system.

The first goal of this dissertation is to develop and validate a reduced-order model based on a set of physics-based partial differential equations. The second goal is to develop a process to configure the reduced order model by using only commonly available laboratory equipment. Finally, the third goal is to demonstrate the reduced order model can be modified to account for observed behaviors in real-world devices.

The first goal is accomplished by developing a frequency-domain transfer function and, by using the discrete-time realization algorithm to create a discrete-time state-space model. The second goal is achieved by introducing a process to re-write the model in terms of

circuit-like variables easily identified from voltage and current measurements. The third goal is to obtain a full set of optimized internal parameters that can be modified as needed, based on observed behaviors.

The three goals, when combined, form a complete modeling process that can be used to easily simulate supercapacitor systems. The model can be easily updated or modified as needed. Finally, the model development parallels certain battery system models, and should be suitable to be used along-side such systems meeting the original idea of helping to mitigate high current situations for lithium-ion cells.

Dedicated to my wife, Leslie, and our two sons, Miles and Matt.

Table of Contents

List of Tables

List of Figures

CHAPTER 1

Introduction

During the last 15 years, the electric vehicle (EV) industry has seen tremendous growth and technological advances. Numerous improvements to both secondary batteries as well as complete battery systems have provided longer operating times, greater distances between charges, and improved safety. Present day EVs rely almost exclusively on advanced lithium-ion cells but despite new materials, better designs, and improved performance, these cells do posses limitations. One limitation is their inability to handle high charge/discharge currents efficiently without sustaining physical damage or permanent performance degradation. Repeated or sustained high current from hard acceleration and/or regenerative braking can result in both damage and degradation from internal heat generation and should be minimized or altogether avoided. One example of a method to avoid high current problems is to *shunt* away, or otherwise dissipate, the high currents that may be generated from regenerative braking systems. Shunting away high current however, results in lost opportunity for improved efficiency. In addition to degradation problems from excessive heat, high currents also cause generally unwanted voltage rises or drops affecting system performance. Therefore, any methods or devices that can be used to mitigate the effects of high current are potentially worth investigating and implementing mitigation systems is one goal of battery system designers.

Power density is a measure of how much power, per volume or per mass, can be delivered by an energy storage device. Energy density is similar but refers to the amount of time in which a device can deliver its power. High power density and high energy density are both desirable properties for an energy storage device but one is usually gained by sacrificing the other. Lithium-ion cells are considered to be quite energy dense but not so in terms of power density. In other words, they can deliver a constant current for a long time but are limited in how much short-term current they can deliver. They are lower in *power density*

but high in *energy density*. Supercapacitors, on the other hand, can deliver *large* amounts of current but only for a short amount of time and are thus considered to be *power dense* but not *energy dense*.

Marrying energy dense lithium-ion cells with power dense supercapacitors would seem to bring the best of both to a single energy system. The concept is not new and designers have been combining these two types of systems for several years. What has not been done until recent years has been accurate modeling of these hybrid systems. Lithium-ion cell modeling research has been ongoing for many years and in the last several years, there has been an interest in using the well established battery modeling techniques and approaches with supercapacitors.

This work identifies several common modeling approaches that have been used for both batteries and supercapacitors. Drawbacks and advantages of popular approaches approaches are described. Physics-based models are introduced as a promising approach to supercapacitor modeling, and existing techniques for modeling lithium-ion cells are used to create a reduced-order, supercapacitor model. Combining similarly prepared reduced-order models should be simple and can form the basis for creating complete battery/supercapacitor system models.

The more correct name of Electrochemical Double Layer Capacitor, abbreviated EDLC, will be used interchangeably with the terms supercapacitor, ultracapacitor, gold-capacitor, and other marketing names all referring to the same general device. EDLCs, due to their construction, can pack a very large amount of charge into a very small volumetric space and are very power dense. An EDLC the size of a soda can might be rated at 3000 or more farads. EDLCs the size of a standard C-cell can have ratings on the order of several hundred Farads. The high power density is attained at the cost of a lower operating voltage, but due to their extremely low rates of degradation, they are a popular choice for designers needing short duration, high current, sinks or sources. Finally, they can be charged and discharged on the order of 10^5 times and still not show degradation while modern lithium-ion batteries begin to show aging after only a few thousand charge cycles [3].

This work builds upon existing porous electrode EDLC models and adds methods to identify many of the relevant internal components. The discrete-time realization algorithm

as introduced by Lee [4] is used to obtain a *reduced-order model*, (ROM), in state-space form, of an EDLC from a derived frequency-domain impedance transfer function.

To set the stage for the remaining chapters, an introductory section covering the basic capacitor types and mechanisms of operation is included. EDLCs are similar in construction to lithium-ion but, in contrast, there are no redox chemical reactions. Their operation depends solely on electrostatic, non-faradaic, double layer phenomena. Following the capacitor introduction is a section describing the EDLC and its primary components.

1.1   Capacitor Basics

Capacitors, no matter the type, capacity, or working voltage, all work on the same general principle of energy storage via charge separation. Charge is separated by the application of a potential difference between two conductive materials with a non-conductive region between them. Electrostatic forces cause the two oppositely charged sides to try to equalize by recombining, and when an external conductive path is established between the two sides, the charges recombine and do work in the process.

The capacitance of a device is a measure of how much charge it can store, and at what voltage. Any introductory circuits text will likely contain the following five basic capacitor equations forming a foundation for describing capacitor behavior during various current and voltage conditions.

The first two equations describe capacitance in terms of physical properties, charge, and potential. Capacitance is based on physical properties such as the device surface area A, where charge accumulates, how much charge is stored, Q, the potential V, in volts between the two electrodes, thickness d of the dielectric and the permittivity, ε, that is a measure of how well the two electrodes sense each other electrostatically. Capacitance, in farads, is generally defined by,

$$C = \frac{Q}{V} \tag{1.1}$$

$$C = \frac{\varepsilon A}{d} \tag{1.2}$$

When current is applied to a capacitor, the resulting current-voltage relations can be stated as shown by Eqs. (1.3) and (1.4) relating the capacitance, potential, current, and time.

$$i(t) = C\frac{\mathrm{d}v}{\mathrm{d}t} \tag{1.3}$$

$$v(t) = \frac{1}{C}\int_{t_0}^{t} i(t)\mathrm{d}t + v(t_0). \tag{1.4}$$

Finally, all capacitors will block all current but and only *seem* to allow the flow of ac current. During ac operation, as they are charging and discharging, electrons flow into and out of both sides but not from side *to* side. Thus the *appearance* of allowing ac current to flow. The impedance of a capacitor, Z_C, is inversely proportional to the operating frequency thus, Z_C is small when the frequency is high, and large when the frequency is low. Equation (1.5) summarizes the impedance in the time-domain and, via the Laplace transform, in the frequency-domain. It should be noted that while the *capacitance* itself is a constant, its actual *value* does have an effect on the impedance as can be seen in impedance equation as

$$Z_C = \frac{1}{j\omega C} \xRightarrow{\mathcal{L}} \frac{1}{sC}. \tag{1.5}$$

Capacitors can be generally lumped into one of three distinct families based on their internal construction and components: solid, electrolytic, and electrochemical double layer. All are in common use across the realm of electronics and all will generally follow the above five equations[1]. The next several sections provide a brief introduction to the three general families of capacitors at a somewhat more physical level.

1.1.1   Solid Capacitors

The first family of capacitors consists of two metallic conductive plates sandwiching a dielectric made of mica, ceramic, air, or other non-conductive material. Figure 1.1 shows a representative description. When a potential difference is applied to the two conductive plates, positive and negative charge builds up on the two metal plates and energy is stored in the resulting electrostatic field. The dielectric plays an important role because if it is too thick, there will be only a small electrostatic field while if it is thin, it may breakdown

---

[1]These equations are for an ideal capacitor. This dissertation develops more realistic models of EDLCs.
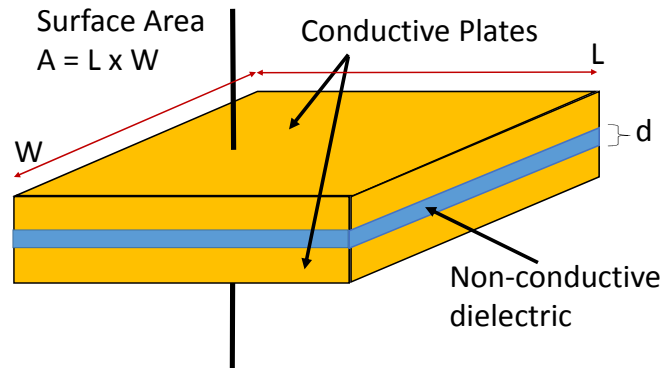
Figure 1.1: Solid capacitor

causing device failure. Capacitance is defined by Eq. 1.2 where the dielectric permittivity ε, is a measure of how well charge *senses* charge of the opposite polarity, through a dielectric with thickness d, and a cross-sectional surface area A. To increase the capacitance, the capacitor surface area A can be made larger, the dielectric can be made thinner, or a different dielectric used altogether. The problem then becomes size and voltage limitations. For high capacitance, the device can quickly become quite large and hence difficult to use in circuit board applications. If the dielectric is too thin, high voltages can puncture it thus destroying the capacitor. As a result, solid dielectric capacitors generally have small capacitance values in the f F—n F range and are most commonly used in lower voltage microelectronics applications. Solid capacitors, in general, are not polarized.

An *important* observation is that because the dielectric is solid, there are few, if any, mobile ions present in the dielectric and thus no moving parts. Neither are there any chemical reactions to accelerate aging and for these reasons solid capacitors show very few signs of aging with use and should last for many years.

1.1.2   Electrolytic Capacitors

The second family of capacitors addresses the surface area limitation by using an *etched* metal foil as the positive, or anode, current collector[2]. The dielectric is an oxide layer physically grown onto the anode. As the anode is charged, its etched surface provides a much larger surface area A, thus increasing the amount of charge that can accumulate. The negative current collector, or cathode, cannot directly be in contact with the oxide layer as the negative connection would deconstruct the oxide. Instead, either a thin paper or polymeric membrane, saturated with an electrolyte fills the gap between the oxide layer and the cathode. As the anode increases its positive charge, negative ions in the electrolyte can accumulate at the surface of the oxide layer. The large surface area A, and the thin oxide layer d, both contribute to a much higher device capacitance than solid capacitors. Figure 1.2 illustrates the construction.

Electrolytic capacitors must be operated with the correct dc polarity because, under reverse polarity, the oxide layer is likely to de-construct itself; sometimes with spectacularly loud results. With correct polarity, well grown oxide layers can generally withstand voltages as high as 600 V and for this reason were commonly used in early *vacuum tube* technology requiring high voltage for operation. Electrolytic capacitors are very common in modern electronics and generally are built in the μ F—m F range.

1.1.3   Modern Electrochemical Double Layer Capacitors

Modern EDLCs grew out of early research with electrostatically charged activated carbon structures functioning as water filters where an electric potential polarized a carbon electrode and attracted water molecules carrying ionic impurities such as a salt [6,7]. Today's EDLCs still use activated carbon for their electrodes that do not differ significantly from electrodes of the 1950s and 1960s. Of course, today's devices are now generally called EDLCs and used as actual capacitors.

Like lithium-ion cells, EDLCs consist of three major parts as illustrated in Fig. 1.3: two identical porous electrodes, a thin paper or membrane separator, and an electrolyte

---

[2]The anode in a battery is typically referred to as the negative terminal. In electrolytic capacitors however, the anode, or positive terminal, is the one on which the oxide layer is grown [5].
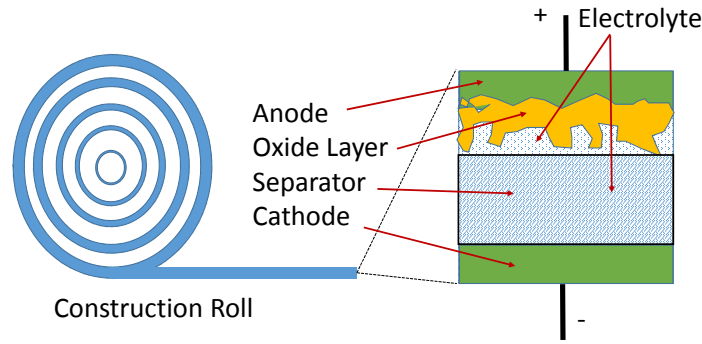
Figure 1.2: Electrolytic rolled capacitor

suffused throughout the entire device. Because the two electrodes are identical, either can be considered the *anode* and then the other becomes the *cathode*. The term *electrode* is used interchangeably to reference either from this point forward. Manufacturers, however, *suggest* there is an inherent polarization that occurs during the initial factory charging process and therefore the commercial device has polarity markings.

1.1.3.1 EDLC Electrodes

EDLCs possess a tremendous surface area A because of the porous nature of their identical electrodes. The electrodes are typically manufactured from electronically conductive activated carbon and chemically bonded to a metal foil or metal cloth fiber [8], current collector. At the microscopic level the electrode looks somewhat like a sponge as shown in Fig. 1.4(a) and thus the description *porous*. In contrast, an aluminum oxide current collector has a much more flat appearance as shown in Fig. 1.4(b) and thus a much smaller surface area.

When potential is applied between the two electrodes, electrons quickly work their way into or out of the solid part of the electrode. Opposite charges present in the electrolyte accumulate near the charges in the solid surface. It is this process that results in formation of an electric double layer (DL). Early references [9, 10] do not make distinctions between
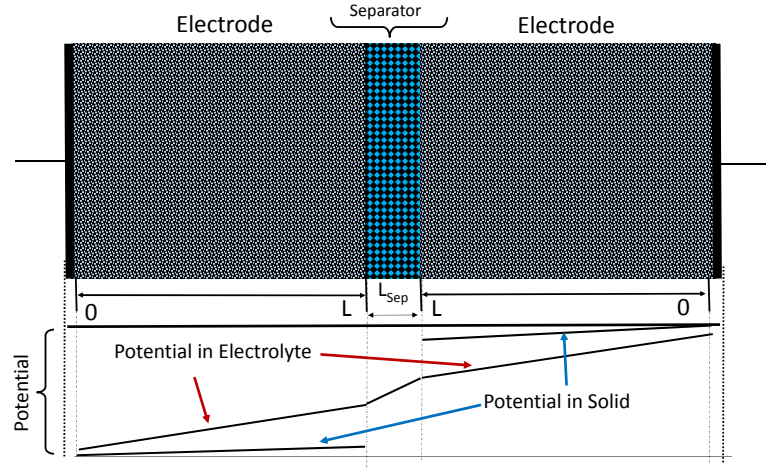
Figure 1.3: EDLC capacitor structure

EDLCs and electrolytic capacitors [11] but there is a significant difference. EDLCs do *not* posses a dielectric and, in fact, the distance d, used in the capacitance equation is generally considered to be on the order of a single ionic radius! It is precisely the extremely small distance d between the solid and solution side of the surface, and the extremely large surface area A, that maximize the capacitance equation, Eq. (1.2). Modern EDLCs the size of a typical C-cell battery can have capacitance ratings of nearly 300 F and single devices exceeding 3000 F are commercially available [12, 13].

New electrode materials and construction methods, such as using carbon nano-structures [14, 15], are continuously being studied although such research is outside the scope of this work.

1.1.3.2 EDLC Electrolytes

EDLCs contain an electrolyte permeating throughout the entire device saturating both electrodes and the separator. Its purpose is to provide ions small enough to pass through the separator and into the smallest pores present in the electrodes. It also must be able to withstand the presence of an electric field without dissociating into its atomic or molecular constituents. The electrolyte is probably the most important part of an EDLC as it can affect internal resistance, limit the maximum operating voltage, and is a key component

(a)   (b)
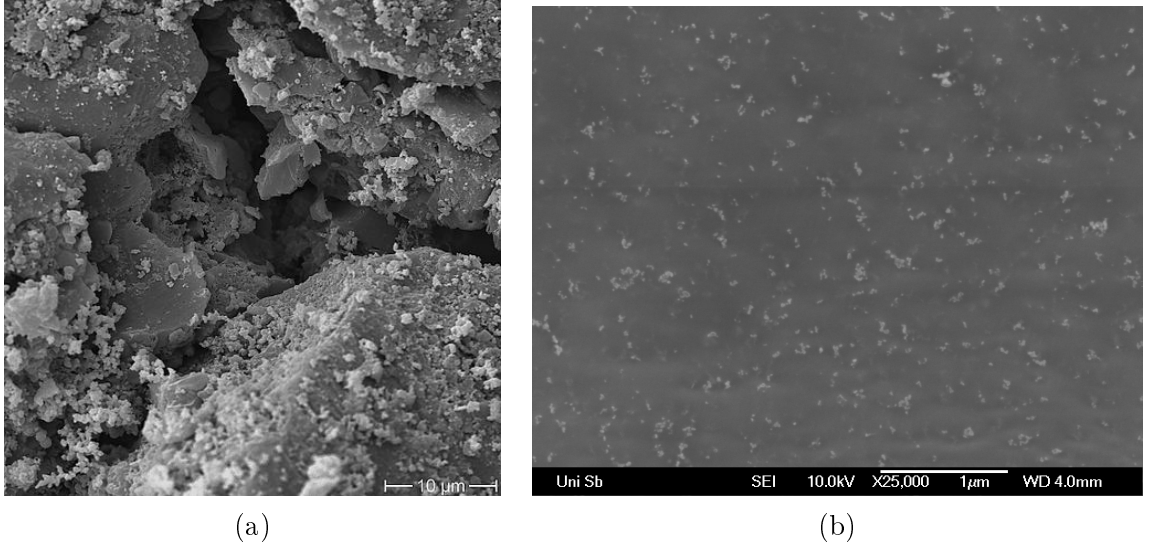
Figure 1.4:   Porous versus non-porous SEM image: (a) Activated carbon electrode [1] (b) Aluminum oxide current collector [2]

to determining the device capacitance [16]. Water is an inexpensive solvent offering good conductivity but can dissociate into gasses at rather low operating voltages and such cells generally do not exceed 1.5 V. Organic solvents such as acetonitrile offer a higher dissociation voltage and with well chosen salts such as tetraethylammonium tetrafluoroborate ((TEA-BF4) [17–19], give much higher cell voltages on the order of 2.7 V. Organic based electrolytes are not as conductive as water-based, or aqueous solutions.

Research is presently being conducted by numerous groups and individuals on solvents, salts, construction methods and materials, with the ever present goal of making a better device. While quite interesting, that is not the direction of this dissertation and modeling efforts will be limited to the conductivity of a single species present in both the electrode region as well as in the separator region.

1.1.3.3   EDLC Separators

A paper or thin-film polymeric membrane separates the two electrodes and prevents them from shorting themselves and destroying the capacitor. It must be porous and have a pore size large enough to pass both positive and negative ions from one side to the other, and also

thin to minimize contribution to internal resistance [20]. When saturated with an electrolyte, the separator also will change the electrolyte conductivity within the separator region [21].

1.1.4 Pseudo-Capacitors

An introduction to the general families of capacitors would not be complete without a brief note on *pseudo-capacitors*. Often confused with EDLCs, a *pseudo-capacitor* is a device that bridges the gap between lithium-ion cells and true EDLCs. Unlike EDLCs, *pseudo-capacitors* do not have identical electrodes but instead use activated carbon for one electrode while using a more *battery like* material such as ruthenium-oxide, for the other. Thus, they operate both electrostatically, as do EDLCs, and faradaically, as do lithium cells. Lin [22] and Popov [23] independently developed physics-based models describing the ruthenium-oxide pseudo-capacitor behavior, and it is certainly possible to extend the models in this dissertation to include faradaic processes. Pseudo-capacitors are not currently popular and are difficult to find in the commercial market. One reason is that they are more complex to manufacture and are thus more expensive than EDLCs. They also do not have the expected cycle lifetime as EDLCs. In any case, the study of pseudo-capacitors, or faradaic capacitors, is not within the focus area of this dissertation but, as they are closely related to EDLCs, may be an area in which the models developed here may be extended. Conway [24] is credited with coining the term *pseudo-capacitor*.

1.2 EDLC Properties, Pros and Cons

EDLCs are one of the most power dense devices commercially available and therefore are prime candidates for use in augmenting high-power or high current applications such as those found in EV battery systems. They are not perfect and do have their limitations and like any device, possess some undesirable properties. Tables 1.1 and 1.2 briefly describe some of the more beneficial and non-beneficial EDLC properties.

TABLE 1.1:   Beneficial properties of EDLCs

Property	Description
Power Density ($W\ m^{-3}$)	EDLCs are considered power dense devices and can deliver large amounts of current. These compact devices, gram for gram, will easily outperform a lithium-ion cell, although only for a short time, in raw power.
Cycle Life	Because there are no redox or kinetic reactions taking place in an EDLC, they are commonly capable of well over 100,000 charge/discharge cycles with little degradation and easily exceed the cycle life of a lithium-ion cell.
Internal Resistance (Ω)	With no redox reactions and no intercalation processes, the only resistance to charge movement is due to the separator, metal leads, and the resistivity of the electrolyte and activated carbon. Internal resistance is extremely low and typically is on the order of only a few mΩ.
Environmental	EDLCs are comprised of carbon electrodes, aluminum contacts, and paper separators leaving only the solvent and solute as possible hazards. The most common solvent and solute are acetonitrile and tetraethylammonium tetrafluoroborate both of which, according to material safety data sheets (MSDS), are on the very low end of hazards [25, 26].
High Current Capability	The very low internal resistance allows very high charge or discharge currents to be applied with no resulting device damage making them perfect to sink/source large amounts of current for a short time. They are therefore a potentially good choice for use in systems such as regenerative braking and burst acceleration.
Operating Temperature	EDLCs can effectively operate in the range of about -40° C to 80° C and are thus capable of operating in nearly any environment.
Minimum operating voltage	Modern EDLCs can be discharged to 0 V with no detrimental effects. Lithium-ion cells, in contrast, must remain in a much narrower operating voltage range to avoid damage.

TABLE 1.2: Non-beneficial properties of EDLCs

Property	Description
Energy Density ($W\,h\,kg^{-3}$)	EDLCs cannot store a large amount of energy and will discharge quickly in contrast to a lithium-ion cell. EDLCs have LOW energy density.
Peak operating voltage	Modern EDLCs commonly use an organic solvent such as acetonitrile which may begin to dissociate if the device voltage exceeds 2.7 V. This is in contrast to an operating voltage of lithium-ion cells that can operate upwards of 4.2 V.
Self discharge rate	EDLCs typically will self-discharge at a higher rate than electrolytic or solid capacitors.

1.3 Original Work and Organization

As EDLCs become more popular in large power and power-assist devices or vehicles that require the capability to sink and-or source high currents, there is a need for quality models that are simple to use. The models should address issues important to designers and be capable of being easily integrated with existing battery or control system models. As these new models are developed, then must also be validated against real devices to demonstrate their worthiness. Additionally, the more robust models should include methods to determine internal component and parameter values.

1.3.1 Original Work

The original work presented in this dissertation is focused around the development of a ROM obtained from a physics-based set of equations. These equations originated in the 1960s with water filter applications that utilized the electric double layer, but it was not until the late 1990s that they were collected and presented as a formal model for an EDLC [27,28]. The concept of taking a set of equations to the frequency-domain for analysis as transfer functions is not new. Using the discrete-time realization algorithm, (DRA) [4], to generate an state-space ROM of an EDLC, is however, new. The ROM generation process itself is not the primary contribution, but rather serves as a vehicle to demonstrate how the resulting ROM can be used to advance the study of EDLCs and their use in EDLC-lithium-ion energy systems. The method of representing the EDLC transfer functions in terms of measurable

circuit-element parameters, is also new, although it is really just an application of other additional well known processes.

As a result of this work, there is now a validated EDLC ROM, created using a process similar to that used for lithium-ion cells, and as both use the DRA process, they should be very compatible in further developments of combined systems.

1.3.2 Chapter Organization

Chapter 2: Background. Chapter 2 presents a brief historic account of the development of the electric double-layer model, (EDL or DL), beginning with the earliest mention in 1853 and progressing to modern models. Modern models can be considered as those presented after the 1960s and an example is given. An introduction to circuit-based models is provided as a modeling approach that attempts to represent the observed electrical operation of an EDLC through the use of electronic circuit components. Physics based models are also introduced as a way to model what really happens, based on physical first principles, inside an EDLC. A detailed physics model is explained and presented as a starting point for the ROM derivations of Chap. 3.

Chapter 3: ROM Model Derivation. Transfer functions can represent the impedance of a system in either the time-domain or frequency-domain. The physics-based partial differential equation model from Chap. 2 contains several coupled PDE equations of higher order and a process is identified to combine the PDEs into one or more transfer functions in the frequency-domain. Srinivisan and Fahramandi [27, 28] accomplished similar works, but used a somewhat different methodology. The approach taken here is more general and obtains a time-domain model without the use of trigonometric expansions and related infinite summations. Using the DRA process makes the time-domain transform quick and simple, and although Lee used the DRA for lithium-ion cells, the process also can be applied to EDLCs. Furthermore, the last section successfully validates the original full order physics-based set of PDEs, solved with a numeric solver, against the DRA-produced ROM. The validation illustrates that as long as both the ROM and the true numeric solution use the same set of parameters

and components, their resulting outputs will match. The next question then, is how to obtain sufficient parametric information when such data is not normally provided by manufacturers. Finding simple methods to determine as many parameter values as possible therefore supplies the motivation for Chap 4.

Chapter 4: Parameter Identification. This chapter introduces a method to write the EDLC transfer equations in a form that looks like the equations were obtained from a real circuit. All parameters are in terms of resistors and capacitors and values for all parts are shown to be obtainable using only measurement methods commonly available in most electronics labs. Techniques using nothing more than *voltage-current* measurements are shown to be sufficient for identifying all required parameters. These methods are not really new, but applying the methods to an EDLC and using the results to re-write transfer function has not been done. To validate the parameter identification methodology, the ROM developed in Chap 3 is used to generate a set of *control* data. The ROM is then executed using the circuit-element variation of the transfer function, and the results compared with the set of *control* data with the resulting validation being excellent. The final section of Chap. 4 introduces a method to determine the overall, or *total*, device parameters for conductivity. If internal component dimensions can be obtained, the specific conductivity values can also be derived. Chapter 5 therefore, focuses on first obtaining such dimensional information, and the repeating and validating the identification process on a commercially available device.

Chapter 5: Parameter Validation. Chapter 4 introduced a methodology whereby the transfer function is re-written in circuit element form, and by using only non-destructive tests, identified a process to obtain values for what are termed the *total value* parameters. Chapter 5 completes the process by deconstructing an EDLC and obtaining component dimensional data. The analysis methodology in Chap. 4 is then carried out on a commercially available device and actual parameter values, both specific and total, are obtained. Validation using the extracted parametric data is carried out against data from the real device. The overall results validate the general process, but certain laboratory procedures resulted in unexpected data inconsistencies and may

have skewed some data. As the errors are procedural in nature, they do not affect the process validation.

Chapter 6: Additional Considerations. Some EDLC models include heat generation and dissipation. Most are concerned with how well an EDLC can dissipate internally generated heat and what the effects this heat might have on device performance. While this information may be useful information, Chap. 6 looks specifically at how the circuit-element data obtained by the Chap. 4 methods are affected by both ambient temperature and also high current. To accomplish, the the Chap. 4 tests are carried out across the full advertised temperature range and also across the full range of advertised current. A simple method is then given to modify the ROM for both temperature and current.

Chapter 7: Future works and conclusion. As the parameter identification process was developed, several areas are noted as candidates for for future work. These include modeling of faradaic, or pseudo-capacitors, further voltammetry research, leakage current modeling, and others. The conclusion section summarizes this entire dissertation.

1.4 Summary

Chapter 1 discussed basic capacitor theory and introduced the EDLC. Some of the advantages and disadvantages of using EDLCs for various applications were briefly introduced and the final section discussed original work and the overall chapter organization. Chapter 2 provides an abbreviated history of the double-layer model development that lead to the modern EDLC models. Current modeling efforts, both circuit and physics based, are introduced and discussed. The final section of Chap. 2 details the development of a physics-based model and sets the stage for the remainder of this dissertation.

CHAPTER 2

EDLC Models and Previous Works

2.1   Introduction

There are several approaches to modeling an EDLC including *equivalent-circuit-based* models such as a simple resistance in series with a capacitance, *physics-based* models that apply first principles to develop purely mathematical models, and more esoteric approaches such as neural networks [29, 30]. Each approach has its own advantages and disadvantages respectively. Circuit-based models are easy to understand conceptually, but often have many components for which a value of each must be determined. Physics-based models are generally harder to understand conceptually; they are created with variables and parameters based on internal conditions and components. Their advantage is that they have the capability to estimate the internal state or condition of an EDLC. More esoteric models may use approaches such as neural networks to *teach* an algorithm to predict how an EDLC will behave under *learned* conditions. This dissertation only considers physics and circuit based models.

This chapter begins with a brief introduction and history of the electric double-layer and provides a foundation for modern models. Also included is a short history of the early porous electrode and the first EDLC patent filed in 1954 [9]. The history section is not intended to present a rigorous mathematical model development but rather to just illustrate how, over time, research has taken a concept and evolved it based on physical observations and experiments. It should also be noted that the various historical references have, in some cases, used different terms and naming conventions than are generally used with the more modern models of today.

Having established the DL evolutionary history, and with the operational basics from Chap. 1, it's then appropriate to more formally introduce circuit-based (CB) models and

their components, as they attempt to capture observed EDLC behaviors. A short description of the most common ideal circuit components, and also a description of conceptual non-ideal components, such as the *constant-phase-element* (CPE), concludes the section.

The final section is devoted to introducing and describing the physics-based, PDE model used throughout the remaining chapters. The internal variables and components of an EDLC are discussed as applied in the generation of a set of five coupled PDEs mathematically modeling the device.

2.2 A History of Double Layer Models

The history of the modern EDLC model begins with Hermann von Helmholtz (1821–1894) who published numerous works in several physics journals of that era. Specific historic details are somewhat open to interpretation as his publications were in German and not all have been reprinted in English [31]. There is an ongoing biographical effort by the Stanford psychology department [32] that provides some very interesting historical reading. In any case, Helmholtz is given credit for developing the earliest model of the *Electric Double Layer* now simply known as the Helmholtz DL model.

Building on Helmholtz, there were four other early researchers who further developed and refined the initial Helmholtz model: Louis Gouy, David Chapman, Otto Stern, and David Grahame [33–36]. Each contributed their own ideas to successively refined double layer models that lead to the models developed in the 1960s and now form the basis for nearly all DL and EDLC models currently in use.

The next several sections take a closer look at the contributions of these early scientists and how their efforts have led to the modern day understanding of how EDLCs operate [16, 37].

2.2.1 Helmholtz Model

Hermann von Helmholtz is credited as being the first, to formally discuss the DL concept in his numerous works with electricity, chemistry, electromagnetism, and physics. From about 1850–1880, his descriptions of the electric DL were done primarily as supporting material
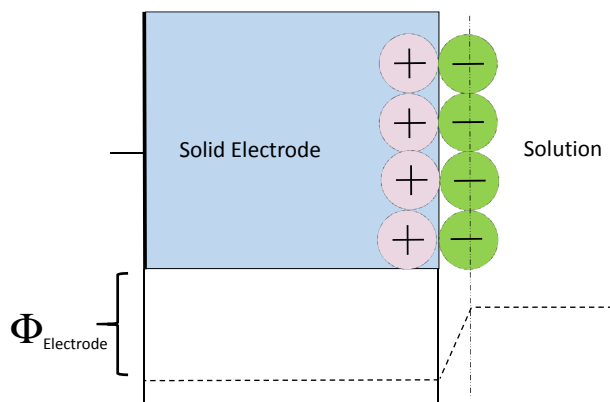
Figure 2.1:   Illustration of the original Helmholtz double layer

for what he considered more important works in physics. He recognized the double-layer as a charge-based structure appearing at the interface between a metal and an ionically conductive solution or liquid. Later, he extended the DL concept to the interface between two dissimilar metals [38]. The Helmholtz DL model is the simplest of all DL models and implies the charge capacity of a DL is governed only by the amount of charge contained in exactly two layers of charge as shown in Fig. 2.1. The model assumes all potential drop to be between the surface and the adsorbed ions on the solution side. The Helmholtz capacitance then follows directly from Eq. 1.2 given by

$$C_{\text{Helmholtz}} = \frac{A\varepsilon}{d},$$

where A is the DL surface area, ε is the electrical permittivity of the surface, and d is the radius of a solvated ion adsorbed to the surface on the solution side. The model neglects leakage and assumes adsorbed charges, both positive and negative, were fixed in position until an external path would allow a discharge. The Helmholtz theory did not adequately explain all DL features as it proposed rigid layers of opposite charges that we now know do not occur in nature. It was, however, a very good start considering the year was 1853!
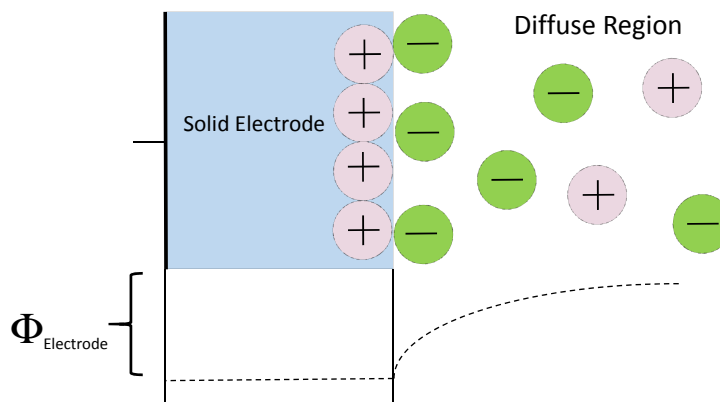
Figure 2.2: Illustration of the Gouy-Chapman model

2.2.2 Gouy-Chapman Model

In the early 20th century, Louis Gouy [34], and David Chapman [33], both working independently, recognized the capacitance of a DL was not a complete constant as Helmholtz had postulated, but rather was influenced by both the applied charging potential as well as the concentration of the ionic solution. They noticed that the capacitance was not a constant, especially at high currents and attributed the observed phenomenon to what became termed as the *diffuse* layer. In other words, instead of a fixed, single layer of charge on the solution side of the interface, they proposed the potential drop on the solution side mostly occurs in the first layer but then decays exponentially into the deeper solution region. In other words, not all of the solution charges contributing to the potential change are adsorbed to the surface but rather, some are mobile and reside some distance away from the surface in the diffuse layer.

Their reasoning led to the creation of what is now known as the Gouy-Chapman DL that includes the application of Maxwell–Boltzmann statistics along with the Poisson distribution to determine where the potential drops occur. Figure 2.2 illustrates the Gouy-Chapman model.

2.2.3 Stern-Grahame Combined Model

In the 1920s, Otto Stern combined the Helmholtz, Gouy, and Chapman models into a single model describing the electric double layer as a one ion thick surface layer, as shown in Fig. 2.3, and the remaining ions in solution as a separate region. The one ion thick layer is now known as the *Stern,* or *Helmholtz* layer, while the much larger solution region is known simply as the *diffuse layer* [36]. He considered both previous models to be partially correct and, in essence, formally combined the Helmholtz and Gouy-Chapman models. The double layer capacitance then becomes the parallel combination of the fixed Helmholtz, and diffuse Gouy-Chapman layers.

Additional developments came from work done by David Grahame [35] formally separating the solution with mobile ions into three distinct regions:

- The layer of ions adsorbed onto the surface define the *Inner Helmholtz plane*, or IHP.

- Ions near the surface but not adsorbed form the *Outer Helmholtz plane*, or OHP.

- Mobile ions located away from the surface form the larger *Diffuse layer*.

$$\frac{1}{C_{\mathrm{dl}}} = \frac{1}{C_{\mathrm{Helmholtz}}} + \frac{1}{C_{\mathrm{diffusion}}}$$

2.2.4 Present Day, or Modern, Models

In the 1960s, beginning with works from Bockris, Devanthan, and Müller [39], research in the field of activated carbon for use in water filtration became popular. The first EDLC patent was filed in 1954 [9], and although it was called a "*low voltage electrolytic capacitor*", was actually an EDLC. Physics-based models of the porous carbon electrodes were developed soon afterward and formed the basis for most of the physics-based models used today. Since that time, the activated carbon porous electrode has been refined, but the basic concepts remain the same. The name, however, has changed and today devices using identical porous carbon electrodes are simply known as *supercapacitors* or *ultracapacitors*.

The most accurate models used today are similar to the one shown in Fig. 2.4 and have several notable differences from earlier models. First, there are three regions of *potential*
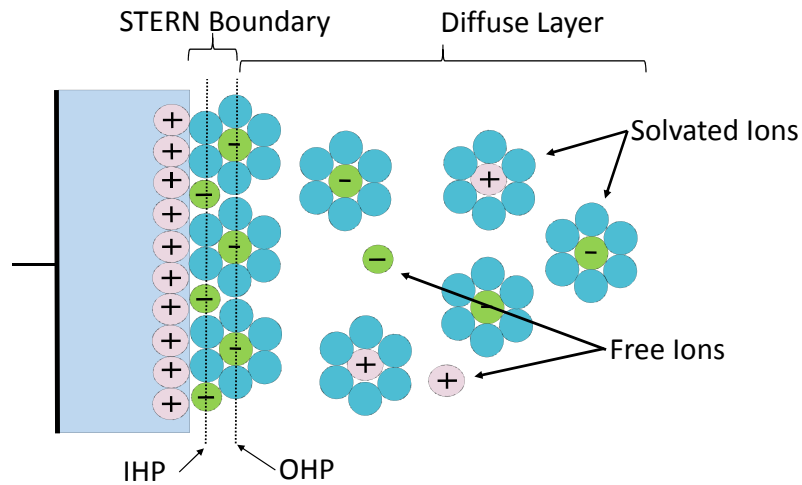
Figure 2.3:   Illustration of the Stern-Grahame model

change within the electrode: the solid region, the bulk electrolyte region, and the electrolyte region immediately adjacent to the DL surface. The electrolyte is split into two regions by the Stern boundary as shown in Fig. 2.4. There are certainly more complex and probably more accurate models being developed, but the difficulty with many of these models is that they can quickly become very complex and time consuming to use. There is a point at which further complexity and rigor, while technically correct, does not make a significant contribution. Considering that the EDLC model developed in the next chapters are are targeted towards use in EV battery systems, the model shown in Fig. 2.4 is sufficient.
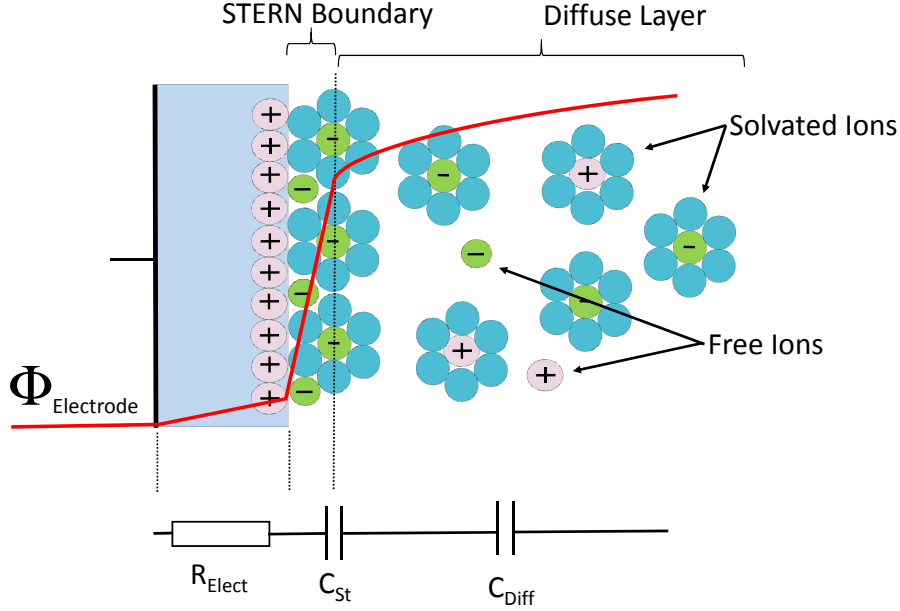
Figure 2.4: Illustration of a typical modern model

2.3 Circuit Based Models

Circuit-based models attempt to create a circuit whose output fits observed behaviors from real EDLCs. These circuits generally contain common components such as capacitors, resistors, and inductors, but may also contain conceptual components such as a Warburg impedance or constant phase element, both of which will be briefly discussed later in this section. Each component, or group of components, is intended to model a particular phenomenon or observed behavior [38].

The majority of circuit models can be grouped into several general variations [40]. First are the classical or simple Randles type cell models that attempt to model an entire cell in a somewhat generic, black box style. No attempt is made to relate specific components to actual structures. This type of circuit often consists of nothing more than a resistance in series with a capacitor-resistor pair. The second type of model *does* attempt to model

various EDLC components, such as the individual electrodes and separator. More advanced circuits might even attempt to model the structural pores or even the *size* of individual pores. Complex *ladder circuits* and *transmission-line circuits*, are also sometimes used to model internal structures. Finally, any of these circuit models might use conceptual circuit elements to handle observed behaviors not readily modeled by traditional resistors, capacitors, and inductors.

2.3.1   Model Components

Circuit models have two types of components: those that are real, such as resistors, and those that are purely conceptual, such as a Warburg impedance. Conceptual circuit elements are often used to handle behaviors not easily handled by real elements [40, 41]. Both types are briefly discussed next. Table 2.1 summarizes the three most common real circuit elements and two somewhat common conceptual elements.

Real Circuit Elements

Any circuit element that can be physically implemented by a single, real device, is considered to be a real circuit element.

Conceptual Circuit Elements

Most circuit models attempting to model an EDLC using only real circuit elements as listed Table 2.1, do a very good job until *odd* behaviors show up in real world validations. An example is a high or low frequency phase change that does not level off but seems to keep on going. The effect could be due to a low frequency diffusion process in the electrolyte, or

TABLE 2.1: Physical circuit elements

Component	Current-Voltage Relation	Impedance	Notes
Resistor (R)	$V = IR$	$Z_R = R$	Frequency Independent
Capacitor (C)	$I = C\frac{\mathrm{d}V}{\mathrm{d}t}$	$Z_C = \frac{1}{j\omega C} \Rightarrow \frac{1}{sC}$	Frequency Dependent
Inductor (L)	$V = L\frac{\mathrm{d}I}{\mathrm{d}t}$	$Z_L = j\omega L \Rightarrow sL$	Frequency Dependent
Warburg impedance (W)	-	$\frac{\sigma}{\sqrt{\omega}} - j\frac{\sigma}{\sqrt{\omega}}$	Low Frequency
Constant phase element (CPE)	-	$\frac{1}{\omega^n}e^{-\frac{\pi}{2}nj}$	-

could be related to a high frequency double layer capacitance effect. These effects can often be modeled, at least partially, by using various structures of basic circuit elements such as a successively smaller resistor and capacitor combinations. Lengthy transmission line models might also be used. If however, the real circuit elements do not adequately model the behavior, the Warburg impedance and Constant Phase Element (CPE), are two conceptual elements that are sometimes used in lieu of a sub-circuit or sometimes directly substituted for an individual element. The hope is that they can, with properly adjusted parameters, accurately model the *odd* behaviors. They cannot, however, be purchased at Radio Shack, Mouser, or even at Digi-Key because they don't really exist. They are artificial elements created specifically to handle various non-ideal behaviors. At the cost of possibly limiting simulators to ones that can handle conceptual elements, the advantages of simplicity and a better fitting circuit model can be achieved. Gamry Instruments has an excellent primer on fitting observed data using both real circuit elements as well as conceptual ones to create very accurate equivalent circuit models [42].

None of the models developed in this dissertation include CPEs or Warburg impedance elements, and are unlikely to ever contain such elements. Using this type of circuit element defeats the purpose of physics-based models, and if there are specific behaviors not accounted for in the model, the model itself needs to be modified. Handling unexpected behaviors in real world EDLCs is, for now, left as an area for additional work as described in Chap. 7. Regardless of the modeling, the two most popular conceptual are *briefly* described next [43–45].

Constant Phase Element (CPE)

A CPE is a conceptual circuit often used to replace an imperfect, double layer capacitor in an equivalent circuit model. There are more than one commonly used impedance expressions for the CPE. One commonly used equation is

$$Z_{\text{CPE}} = \frac{1}{\omega^n} e^{-\frac{\pi}{2} n j},$$

where the constant n describes how much the CPE behaves like a true capacitor.

Warburg Impedance ($\mathbf{Z_W}$)

The Warburg impedance circuit element models charge carrier movement by diffusion to large surface area electrodes. It appears in Nyquist plots of real versus complex impedance, at low frequencies. Its impedance is commonly modeled by

$$Z_W = \frac{\sigma}{\sqrt{\omega}} - j\frac{\sigma}{\sqrt{\omega}}.$$

2.3.2 Classical Equivalent Circuit Model

The simplest classical model of an EDLC, illustrated in Fig. 2.5, and commonly known as the Randles cell, is a good starting point to discuss equivalent circuit-based models. It is an okay model for simple simulations but rapidly loses usefulness when increased accuracy is desired. The circuit has a series resistance, often called an equivalent series resistance, or (ESR), that is usually below $100\,\text{m}\Omega$, and a parallel, or leakage resistance, on the order of $100\,\text{k}\Omega$ or more. The measured capacitance is the total double layer EDLC capacitance, although an actual EDLC has two double layers in series with one for each electrode. Using only the circuit elements shown in Fig. 2.5, the simple model provides a very good first order approximation of an EDLC.

(a)   (b)
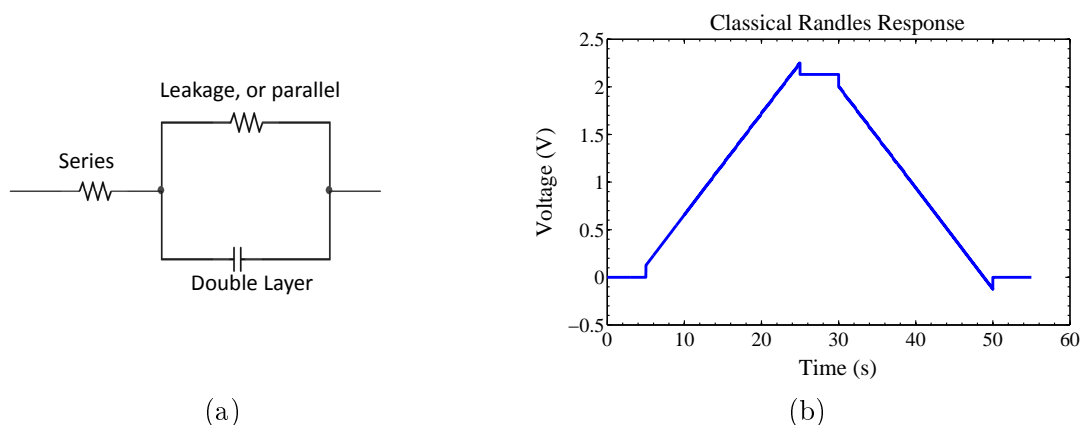
Figure 2.5: Classical Randles cell equivalent model: (a) Schematic (b) Pulse input response
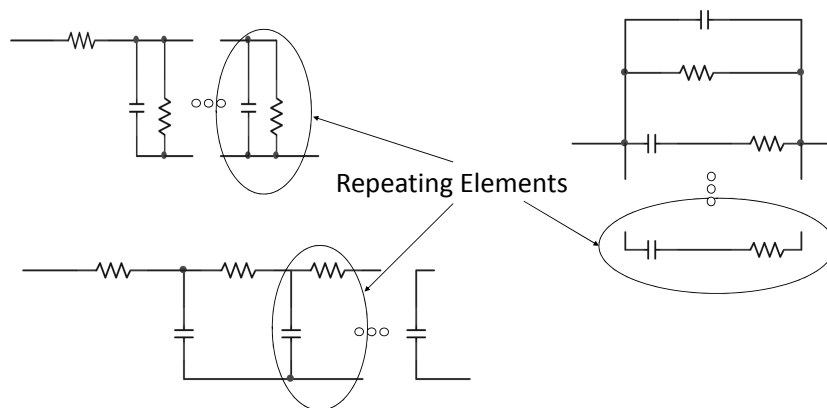
Figure 2.6: Examples of equivalent circuit electrode models

2.3.3 Parallel Branch and Transmission Line Models

Parallel branch and transmission line models generally do a better job of approximating the true behavior of EDLCs by using capacitor-resistor pairs to model the internal structure of individual pores within a porous electrode. As there are many pores, the pore-circuit models need to somehow be combined into only a few sub-circuits, although these circuits may be repeated. The many approximate pore-circuit elements are then combined in some fashion to create a circuit structure that can approximate an EDLC quite well. Warburg impedance elements and CPEs are not usually included, but may be used to replace some of the circuit elements. Three simple examples of a circuit created to model a single electrode are shown in Fig. 2.6.

One of the primary difficulties with any circuit model, is that values for every single element must be obtained. This can be done easily when only several circuit elements exist but can become quite a challenge when higher element counts of 20, 30, or even more elements are considered.
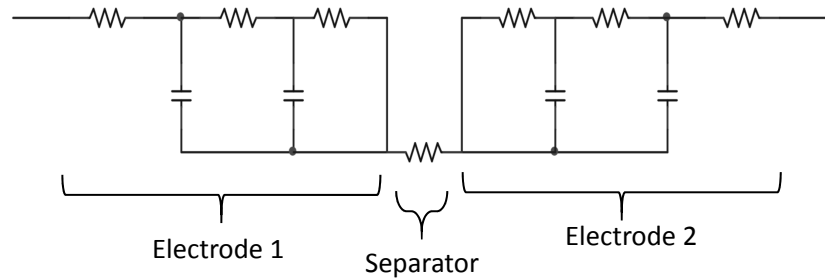
Figure 2.7: Example full EDLC circuit model

2.3.4 Full Circuit Model

The Randles cell in Fig. 2.5 is intended to model an entire EDLC while those shown in Fig. 2.6 model a single electrode. The electrode only models do not account for the separator and also must be used two at a time, increasing the complexity even further. Figure 2.7 shows a relatively simple model of a complete EDLC including the separator and a pair of electrodes. Deriving a transfer function on a circuit of this complexity can certainly be accomplished, but would become much more difficult if additional resistor-capacitor pairs were added.

2.4 A Word on Safety

When simulating a circuit using Spice or MATLAB, it is highly unlikely that one's computer will explode due to a simulation giving an over-voltage condition, nor is the user likely to be shocked by a simulated part. Real devices, however, are not necessarily so forgiving and with the high currents that can potentially be delivered, safety must be considered. EDLCs are very power dense and have a very low internal resistance. Thus, if the terminals are shorted, extreme heat can be generated and a fire could potentially result. Imagine a fully

charged, 3000 F EDLC left in someone's baggage on an airplane. Something shifts during flight and a belt buckle shorts the terminals. The EDLC discharges through the buckle and a fire results. Thus, care must be taken when handling and storing EDLCs.

In the lab, care needs to be taken to avoid equipment damage. Attempting to measure the resistance, or short-circuit current, using a typical multi-meter, can easily blow a fuse or even damage the measuring device. Additional care should also be taken when applying even small voltages to an EDLC. Consider the current if even 1 V terminal difference is directly applied to EDLC having an internal resistance of only $10\,\mu\Omega$. 100,000 A. Zowie!

2.5 The Modern EDLC and Physics-Based Models

Physics-based (PB) models are formed from physical first principals and are generally governed by a set of partial differential equations (PDEs), modeling the system and the dynamics of its components. Posey and Morozumi [6] were among the first to present theoretical mathematical descriptions for the galvanostatic and potentiostatic charging/discharging behavior of one-dimensional porous electrodes in solution. Their 1966 paper is the basis for nearly all of the present day physics-based models considering only non-faradaic[1] processes and specifically not including faradaic[2] ones.

It is also worth describing a one-dimensional electrode. To keep the mathematics simple, current and voltages are considered only in the x direction. Realistically, charge carriers will move in all three dimensional directions but the net, or total charge flow across the electrode is a function of its one dimensional location in the electrode. Extending the model to include additional dimensions may be useful when modeling heat generation and heat flow as heat can exit/enter from any direction.

In 1971, Johnson and Newman [7], developed a set of physics-based PDEs to model a porous carbon electrode for use in the desalinization of water as it adsorbed and de-adsorbed ions on its *extensive* surface. These ideas were expanded by Newman [46, 47], in the 1970s, who was among the first to develop equations specifically addressing both primary and

---

[1]Non-faradaic refers to a charge/discharge process that includes only electrostatic phenomena.

[2]Faradaic refers to a charge/discharge process that includes both electrostatic and oxidation-reduction phenomena.

secondary electrochemical cells. This work would lead to further refinement and additional works specifically addressing the EDLC.

In 1990, Yeu and White [48] developed a mathematical model of a lithium-polypyrrole cell. Their work was loosely based on earlier physics models, but it was their *mathematical process* that led to numerous works regarding many different electrochemical devices.

Farahmandi developed the first impedance model for an EDLC in 1997 [27], and filed a patent for a manufacturing process in 2000 [8]. Subsequently, additional publications took different approaches with slightly different goals but they came up with similar results. One of them consisted of a physics-based model of an EDLC without faradaic processes [28], while another specifically included faradaic processes [22].

It is these publications and studies from the late 1990s that provide the starting point for the new work in this dissertation.

2.5.1   EDLC Structure

The structure of an EDLC is similar to that of a lithium-ion cell with several notable differences. An EDLC consists of two *identical* electrodes and a separator. EDLCs rely entirely on non-faradaic current, meaning there are no oxidation or reduction reactions taking place. The porous separator, allows ions to move from one electrode to the other while preventing any electronic connection. Figure 1.3 illustrates the general structure of a typical porous carbon electrode based, EDLC.

Each electrode can be considered as a *continuum,* comprising both solid and electrolyte materials. In other words, both the solid and electrolyte are considered to be separate, but continuous, across the entire electrode length. When charged, a potential difference exists between the terminals but it is only during the actual charging and dis-charging times that interesting changes occur within the device. As current flows, a potential drop is developed due to internal resistance. The bottom half of Fig. 2.8 illustrates the general change in potential for each region across the entire EDLC.
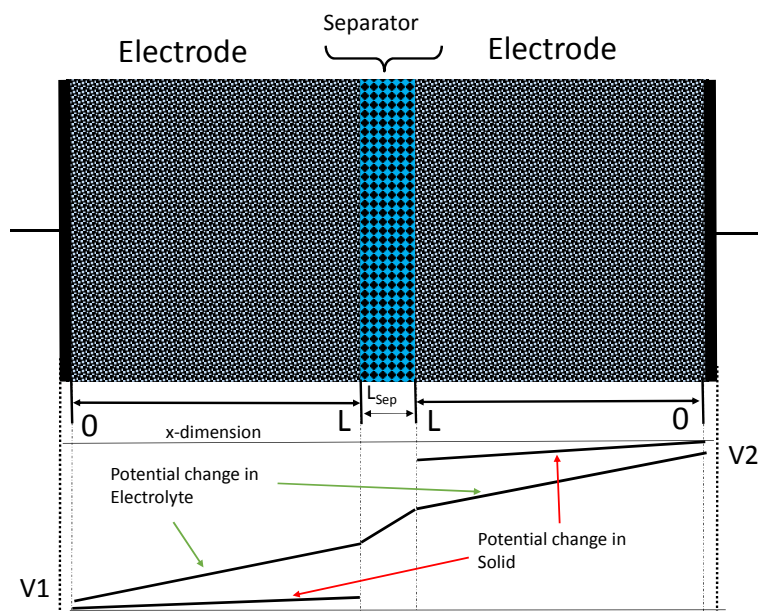
Figure 2.8: Complete EDLC structural model

2.5.2 Parameters and Variables within the EDLC

Parameters are generally considered to be the constants in a model while variables are expressed in terms of parameters. Parameters may include physical attributes such as lengths, widths, and specific conductivities. Variables, on the other hand, are measured in terms of parameters and are quantities that may vary over time and space such as the electrode potential at any given point, x, within the electrode.

2.5.2.1 EDLC Parameters

Parameters are values assigned to constants within an EDLC. They may change from one device to another, but within a single device, are assumed to be fixed quantities. The following are of importance and used often in the derivations and models to follow in later chapters:

- Electrode and separator length. Denoted as L and L_{sep}, these are the distances between the current collector and the separator, and the distance between the two sides of the separator.

- Conductivity in the electrode continuum. Denoted σ and κ, for the solid and electrolyte respectively, these constants have units of S m^{-1}, and thus σ and κ are both *specific* conductivity values and not total device values.

- Conductivity in the separator. Denoted κ_{sep}, it is the separator conductivity and also has the units S m^{-1}. The electrolyte in the separator is the same as that in the electrodes but the separator-electrolyte interaction may result in a different specific conductivity value.

- Double-layer surface area. Denoted by lowercase a and having units of m^2, this parameter should not be confused with the cross sectional area A. The DL surface area is the huge physical surface area that results from using porous electrodes.

- Specific capacitance of an electrode. Denoted by C and having units of F m^{-2}, it is easily confused with the total device capacitance C_{total}, and the total electrode capacitance $C_{\text{electrode}}$.

2.5.2.2   EDLC Variables

Variables, as used in the EDLC model, depend on either spatial position x within the electrode, with time t, or on the application of an external current or potential. Additional variables are added later, but for now, these are the ones to be aware of:

- Electrode potential as a function of time and location. Denoted $\phi_{\text{s}}(x, t)$ and $\phi_{\text{e}}(x, t)$ where x denotes a physical location along the horizontal dimension of the model, and t denotes time. The subscript indicates whether the variable pertains to the solid or electrolyte portion of the electrode.

- Current density in the electrode continuum. Denoted by i_{s} or i_{e} , and having units of A m^{-2}, this is the amount of current, per square meter, both electronic and ionic, and is dependent on the conductivity parameters as well as the potential variables..

- Interfacial current density, i_{dl}. With units of Am^{-2}, this is the amount of current entering or leaving the DL and is directly related to the current density in the electrode continuum.

- Volume averaged current density. In the initial set of PDE equations, current density is shown as $\varepsilon_s i_s$ and $\varepsilon_e i_e$. The ε term refers to the volume percentage in the electrode. In other words, given an average amount of electrode, the ε term simply conveys what percentage is electrolyte and what percentage is solid. This notation, while technically correct, is ignored by both Farahmandi and Srinivisan who simply used i_s or i_e as a notational simplification. For the models presented here, there is no need to make a distinction between the solid and solution therefore the convention of ignoring the the ε term will be continued, and for the remainder of this dissertation, the terms i_s or i_e will mean exactly the same as $\varepsilon_s i_s$ and $\varepsilon_e i_e$.

- Time t. Time is incremented in units of $1\,ms$ for the majority of the simulations.

- Temperature T. Temperature is not considered until Chap. 6 and unless otherwise noted, will be assumed to be room temperature, $20^{\circ}\,C$.

2.5.3   Governing Equations

The parameters and variables in the previous section can be used to construct a set of five governing equations to mathematically describe the double-layer for a single electrode. Partially developed by the earlier works, the equations were first collected as a *set* by Farahmandi [27] and Srinivisan [28]. They are shown here in their original form but will be somewhat modified at the start of Chap. 3.

$$\varepsilon_s i_s = -\sigma \frac{\partial \phi_s(x,t)}{\partial x} = -\sigma \nabla \phi_s \tag{2.1}$$

$$\varepsilon_e i_e = -\kappa \frac{\partial \phi_e(x,t)}{\partial x} = -\kappa \nabla \phi_e \tag{2.2}$$

$$I_{cell} = \varepsilon_s i_s + \varepsilon_e i_e \tag{2.3}$$

$$\frac{\partial \varepsilon_s i_s(x,t)}{\partial x} = -\frac{\partial \varepsilon_e i_e(x,t)}{\partial x} = a i_{dl} \tag{2.4}$$

$$i_{dl} = -C \frac{\partial \left(\phi_s(x,t) - \phi_e(x,t) \right)}{\partial t}. \tag{2.5}$$

Equations (2.1) and (2.2) are point forms of Ohm's Law, describing the *effective,* or volume averaged, electrode current density at any linear position x within the electrode region. All current in the solid is electronic as indicated by the subscript s while all current in the electrolyte is ionic and denoted by the subscript e. Equation (2.3) defines the total cell current density as the combination of ionic and electronic current densities.

Two boundary conditions should also be noted. The first is at the *current collector-electrode* boundary, where all current is electronic and accounted for by i_s. Secondly, at the *separator-electrode* boundary, all current is ionic and accounted for by i_e.

Conservation of charge requires that for any given location within the electrode, the divergence of ionic current, electronic current, and DL current must sum to zero leading to Eq. (2.4). The variable a is the interfacial surface area across which the double layer is formed as described earlier. Finally, Eq. (2.5) describes the double-layer current density in terms of the generalized capacitor using Eq. (1.1).

2.5.4 Assumptions

When implementing the set of PDEs, there are several assumptions that can be made to simplify the model and also to simplify the analysis process without significantly changing the model outputs. The assumptions currently used are:

- There is no material transport between the solid and electrolyte. Operation is 100% electrostatic.

- Faradaic processes are zero, that is, there are no redox chemical reactions in either electrode.

- All current in the solid carbon part of the electrode is electronic while all current in the solution part is ionic.

- The concentration of ions within the electrolyte is constant and uniform throughout the electrodes.

- Temperature is constant throughout the cell and does not change with time, current, or potential.

- Specific capacitance is constant over the voltage and temperature window of operation.

- The metal foil current collectors, lead wires, and other non-electrode parts are considered to have negligible resistance and contribute nothing to potential changes within the EDLC.

- The two porous electrodes are identical in every way.

2.6   A Word on Notation and Convention

In the following chapters, there are several notational assumptions and also some interchangeable terms. They are summarized here:

- The terms *solution* and *electrolyte* are used interchangeably to refer to the electrolyte.

- The term *electrode* can refer to either the positive or negative electrode. Unless otherwise noted, the two electrodes are identical and no distinction is made.

- The terms DL, and EDL, both mean the double-layer and are used interchangeably.

- The term *estimate* refers to a measurement, assumption, or educated guess, and means the best available data will be used.

- Laplace domain terms are denoted with an *overbar*. Some terms do not have frequency dependent components and are identical in the time and Laplace domain and so the overbar notation should help to eliminate any confusion.

- Resistance is the inverse of conductance and with this in mind, the terms *resistance, conductance, resistivity,* and *conductivity* may be interchanged where convenient to do so without explicitly stating the inverse equation every time.

All numeric plots, unless otherwise noted, have been converted or imported to MATLAB for formatting and printing purposes. To help clarify the differences in data sources, the following color convention, except where otherwise noted, is used for the remainder of this dissertation:

- RED plots - used for plots generated from MATLAB simulations.

- BLUE plots - used for plots containing data captured from real EDLC tests.

- BLACK - used for COMSOL and other data sources besides MATLAB generated and real devices.

2.7   Summary

Chapter 2 presented a brief history of the electric double-layer illustrating its development from the very basic first model to the generally accepted modern models. Circuit-based models attempting to reproduce observed EDLC behaviors and structure of the DL were presented as the first method of modeling. A second modeling method, physics-based, was presented next. Physics-based models have the advantage of being able to predict the internal state, or condition of an EDLC, whereas circuit models do not.

The final part of this chapter introduced the physics-based model that will be used as the basis for the derivations in the next chapter.

CHAPTER 3

A Reduced Order Model of an
Electrochemical Double Layer Capacitor

3.1 Introduction

In Chap. 2, both circuit-based and physics-based models were described. CB models have
the advantage of being relatively easy to understand and simulate but may have the disad-
vantage of a large component count with each component needing to have a value identified.
Additionally, CB models do not posses the ability to predict the state or condition of vari-
ables and parameters internal to the device being modeled. Physics-based models, while
more mathematically complex, can provide an insight to how the device is operating by pro-
viding a view of its internal condition, or state, at any point within the device. Therefore,
it seems that PB models that can provide simulation data on par with CB models and also
include internal state information, are the better choice. Developing such a model is the
primary goal of this chapter.

The model developed by the end of this chapter begins with the five governing equations
from the end of Chap. 4 and derives several transfer functions that are used to develop the
final impedance transfer function of an entire EDLC. The final transfer function, and its
time-domain state-space counterpart, form the basis from which all reduced-order models
in the remainder of this dissertation are derived.

The model developed in this chapter uses only a small number of parameters that
are generally not present on current data sheets. Obtaining parametric data then becomes
a problem. Chapter 4 will introduce a method to identify all needed parameters using
only non-destructive techniques and tests. For now, the parameters used have been chosen
somewhat arbitrarily.

To obtain the EDLC transfer function, the approach taken by Srinivisan and Wiedner is modified to both generalize and clean up some notational inconsistencies. In addition to the full cell model, several transfer functions for the current and potential in both the solution and solid are obtained during the derivation process. Only the full cell transfer function is used; the others are noted for later reference and will be of use in future work that specifically considers internal states and conditions.

Chapter 3 is split into three main sections:

1. The five governing equations are combined and used to develop transfer functions for the EDLC.

2. A numeric methods solver, COMSOL, is used to simulate the original set of governing equations and obtain a full order model (FOM).

3. The Discrete-time Realization Algorithm, as presented by Lee, is used to create a reduced-order model.

Concluding Chap. 3 is a validation comparing the reduced-order model (ROM), against the numerically exact (FOM). The very positive results of the comparison between ROM and FOM, and possible sources of error, are discussed.

3.2 A One-Dimensional Model of an EDLC Having Identical Porous Electrodes

Using the five PDE equations introduced in final section of Chap. 2, Srinivisan and Wiedner developed a Laplace-domain, impedance transfer function model for an entire EDLC [28]. The approach taken here is similar but more general in nature and cleans up notational discrepancies as described earlier.

First, the five equations are normalized in space and only then are they combined and used to derive the Laplace-domain transfer function for the potential within a single electrode. The model will then be extended such that it is able to predict the potential at any point within the entire EDLC. All of the work here is considered one-dimensional

but could be easily extended to two or three dimensions if required. The variables and parameters used were described in Chap. 2 and unless otherwise noted, are not re-described.

3.2.1 Governing Equations for a Porous Electrode

Before starting the derivation, there are some minor changes to make to the original five governing equations as presented in Chap 2. First, Eqs. (2.1) and (2.2) are normalized in length by the substitution $\xi = \frac{x}{L}$ allowing L to become a system parameter. Next, the subscripts used by Srinivisan are changed from the numbers 1 and 2, to the letters e and s to represent the electrolyte and solid parts of the electrode. Also, the current and potential functions all have arguments of (ξ,t), length and time, unless otherwise noted. Thus, with these modifications, the equations from the end of Chap. 2 become:

$$i_{\mathrm{s}} = -\frac{\sigma}{L}\frac{\partial\phi_{\mathrm{s}}(\xi,t)}{\partial\xi} \tag{3.1}$$

$$i_{\mathrm{e}} = -\frac{\kappa}{L}\frac{\partial\phi_{\mathrm{e}}(\xi,t)}{\partial\xi} \tag{3.2}$$

$$I_{\mathrm{cell}} = i_{\mathrm{s}} + i_{\mathrm{e}} \tag{3.3}$$

$$\frac{1}{L}\frac{\partial i_{\mathrm{s}}(\xi,t)}{\partial\xi} = -\frac{1}{L}\frac{\partial i_{\mathrm{e}}(\xi,t)}{\partial\xi} = ai_{\mathrm{dl}} \tag{3.4}$$

$$i_{\mathrm{dl}} = -C\frac{\partial\left(\phi_{\mathrm{s}}(\xi,t) - \phi_{\mathrm{e}}(\xi,t)\right)}{\partial t}. \tag{3.5}$$

The *specific* capacitance C is considered a constant as are the carrier concentrations in both the electrolyte and solid parts of the electrode. Temperature is not considered until Chap. 6. The first step then, is to combine equations to obtain a single expression containing the elements of all five equations.

3.2.2 The Transfer Function of a Porous Electrode

Beginning with the identity $(\kappa + \sigma = \kappa + \sigma)$ and multiplying both sides by ai_{dl} gives

$$ai_{\mathrm{dl}}(\kappa + \sigma) = \kappa ai_{\mathrm{dl}} + \sigma ai_{\mathrm{dl}}.$$

Substituting the two forms of ai_{dl} from Eq. (3.4) gives

$$ai_{\mathrm{dl}}(\kappa + \sigma) = \frac{\kappa}{L}\frac{\partial i_{\mathrm{s}}}{\partial\xi} - \frac{\sigma}{L}\frac{\partial i_{\mathrm{e}}}{\partial\xi}$$

and substituting Eqs. (3.1) and (3.2)

$$ai_{\mathrm{dl}}(\kappa+\sigma) = -\frac{\kappa\sigma}{L^2}\frac{\partial^2\phi_{\mathrm{s}}}{\partial\xi^2} + \frac{\kappa\sigma}{L^2}\frac{\partial^2\phi_{\mathrm{e}}}{\partial\xi^2}.$$

Substituting the capacitor equation, Eq. (3.5), and rearranging leads to

$$a\left[-C\frac{\partial(\phi_{\mathrm{s}}-\phi_{\mathrm{e}})}{\partial t}\right](\kappa+\sigma) = \frac{\kappa\sigma}{L^2}\left(-\frac{\partial^2\phi_{\mathrm{s}}}{\partial\xi^2} + \frac{\partial^2\phi_{\mathrm{e}}}{\partial\xi^2}\right)$$

$$a\left[-C\frac{\partial(\phi_{\mathrm{s}}-\phi_{\mathrm{e}})}{\partial t}\right](\kappa+\sigma) = -\frac{\kappa\sigma}{L^2}\left(\frac{\partial^2\phi_{\mathrm{s}}}{\partial\xi^2} - \frac{\partial^2\phi_{\mathrm{e}}}{\partial\xi^2}\right)$$

$$a\left[C\frac{\partial(\phi_{\mathrm{s}}-\phi_{\mathrm{e}})}{\partial t}\right] = \frac{\kappa\sigma}{L^2(\kappa+\sigma)}\left(\frac{\partial^2(\phi_{\mathrm{s}}-\phi_{\mathrm{e}})}{\partial\xi^2}\right).$$

Defining the overpotential between the solid and electrolyte at any given point by

$$\eta(\xi,t) = \phi_{\mathrm{s}} - \phi_{\mathrm{e}}$$

gives

$$aC\frac{\partial\eta(\xi,t)}{\partial t} = \frac{\kappa\sigma}{L^2(\kappa+\sigma)}\frac{\partial^2\eta(\xi,t)}{\partial\xi^2}, \tag{3.6}$$

and further defining

$$\tilde{\eta}(\xi,t) = \eta(\xi,t) - \eta(0,t), \tag{3.7}$$

to account for any initial conditions, Eq. (3.6) becomes

$$aC\frac{\partial\tilde{\eta}(\xi,t)}{\partial t} = \frac{\kappa\sigma}{L^2(\kappa+\sigma)}\frac{\partial^2\tilde{\eta}(\xi,t)}{\partial\xi^2},$$

and then with some rearranging gives

$$\frac{\partial^2\tilde{\eta}(\xi,t)}{\partial\xi^2} = \frac{L^2aC(\kappa+\sigma)}{\kappa\sigma}\frac{\partial\tilde{\eta}(\xi,t)}{\partial t}. \tag{3.8}$$

Equation (3.8) now contains the elements of all five governing equations and can be solved by the use of Laplace transforms. The Laplace transform of Eq. (3.8) can be found from online tables of transforms, or, can be manually worked out in a painful process including integration by parts [49]. Either way, the general solution is

$$\mathcal{L}\left[\frac{\partial^2 u(x,t)}{\partial x^2} = \frac{\partial u(x,t)}{\partial t}\right] \Longrightarrow U_{xx}(x,s) = sU(x,s) - u(x,0),$$

and when applied to Eq. (3.8) gives

$$\mathcal{L}\left[\frac{\partial^2 \tilde{\eta}(\xi,t)}{\partial \xi^2}\right] = s\frac{L^2 aC(\kappa+\sigma)}{\kappa\sigma}\frac{\partial \overline{\tilde{\eta}}(\xi,s)}{\partial \xi} - 0,$$

where the *overbar* indicates a variable in the Laplace-domain. Making a further substitution of $\Upsilon(s) = \sqrt{\frac{sL^2 aC(\kappa+\sigma)}{\kappa\sigma}}$ for equation clarity, the equation becomes

$$\frac{\partial^2 \overline{\tilde{\eta}}(\xi,s)}{\partial \xi^2} = \Upsilon^2(s)\frac{\partial \overline{\tilde{\eta}}(\xi,s)}{\partial \xi}. \tag{3.9}$$

Note the $\Upsilon(s)$ term also contains an expression for the parallel ratio of the solid and electrolyte conductivities, $\frac{(\kappa+\sigma)}{\kappa\sigma}$, that will be useful for later analysis.

Equation (3.9) can be solved by recognizing it has the same general form as the well known heat equation whose generic solution can be obtained from lookup tables as

$$\overline{\tilde{\eta}}(\xi,s) = C_1 e^{\sqrt{\Upsilon^2(s)}\xi} + C_2 e^{-\sqrt{\Upsilon^2(s)}\xi},$$

and by using the two hyperbolic identities $\cosh = \frac{e^x + e^{-x}}{2}$ and $\sinh = \frac{e^x - e^x}{2}$, becomes

$$\overline{\tilde{\eta}}(\xi,s) = C_1 \cosh(\Upsilon(s)\xi) + C_2 \sinh(\Upsilon(s)\xi). \tag{3.10}$$

The two constants C_1 and C_2 must now be chosen such that they satisfy the boundary conditions noted earlier in Chap. 2. One boundary is where the current collector interfaces with the electrode and the second is where the electrode interfaces with the separator. At the first boundary, where $x = 0$, all current is electronic meaning $i_e = 0$ while at the second boundary, where $x = L$, all current is ionic and thus $i_s = 0$. These boundary conditions allow the derivation of two expressions for the overpotential η, one in terms of i_s and the other in terms of i_e, that can be used to solve Eq. (3.10).

The next task is to divide out the current in Eq. (3.10) because that, in essence, is the transfer function. Beginning with Eq. (3.3), the applied cell current, equations for i_s and i_e are now derived.

$$I_{\text{cell}} = i_s + i_e.$$

Manipulating this equation twice, gives two nearly identical equations with reversed i_s and i_e

$$\frac{i_e}{I_{cell}} = 1 - \frac{i_s}{I_{cell}}, \tag{3.11}$$
$$\frac{i_s}{I_{cell}} = 1 - \frac{i_e}{I_{cell}}.$$

Substituting Eqs. (3.1) and (3.2) into the above two gives

$$\frac{i_e}{I_{cell}} = 1 + \frac{\sigma}{I_{cell}L}\frac{\partial \phi_s}{\partial \xi}$$
$$\frac{i_s}{I_{cell}} = 1 + \frac{\kappa}{I_{cell}L}\frac{\partial \phi_e}{\partial \xi},$$

and using the previously defined overpotential $\eta = \phi_s - \phi_e$, they become

$$\frac{i_e}{I_{cell}} = 1 + \frac{\sigma}{I_{cell}L}\frac{\partial(\eta + \phi_e)}{\partial \xi}$$
$$\frac{i_s}{I_{cell}} = 1 + \frac{\kappa}{I_{cell}L}\frac{\partial(\phi_s - \eta)}{\partial \xi}.$$

Rearranging to isolate the η terms and again substituting with Eqs. (3.1) and (3.2) gives

$$\frac{i_e}{I_{cell}} = 1 + \frac{\sigma}{I_{cell}L}\frac{\partial \eta}{\partial \xi} + \frac{\sigma}{I_{cell}L}\frac{\partial \phi_e}{\partial \xi} = 1 + \frac{\sigma}{I_{cell}L}\frac{\partial \eta}{\partial \xi} - \frac{\sigma}{I_{cell}\kappa}i_e$$
$$\frac{i_s}{I_{cell}} = 1 + \frac{\kappa}{I_{cell}L}\frac{\partial \phi_s}{\partial \xi} - \frac{\kappa}{I_{cell}L}\frac{\partial \eta}{\partial \xi} = 1 - \frac{\kappa}{I_{cell}\sigma}i_s - \frac{\kappa}{I_{cell}L}\frac{\partial \eta}{\partial \xi}.$$

The electrolyte current i_e is then solved for in terms η to give the *solution current* in the electrode

$$\frac{i_e}{I_{cell}} + \frac{\sigma}{I_{cell}\kappa}i_e = 1 + \frac{\sigma}{I_{cell}L}\frac{\partial \eta}{\partial \xi}$$
$$i_e + \frac{\sigma}{\kappa}i_e = I_{cell} + \frac{\sigma}{L}\frac{\partial \eta}{\partial \xi}$$
$$i_e(1 + \frac{\sigma}{\kappa}) = I_{cell} + \frac{\sigma}{L}\frac{\partial \eta}{\partial \xi}$$
$$i_e = \frac{\kappa}{(\kappa + \sigma)}I_{cell} + \frac{\kappa\sigma}{L(\kappa + \sigma)}\frac{\partial \eta}{\partial \xi} \tag{3.12}$$

and repeated for the *solid current,* also in terms of the overpotential η, is

$$\frac{i_s}{I_{cell}} - \frac{\kappa}{I_{cell}\sigma}i_s = 1 - \frac{\kappa}{I_{cell}L}\frac{\partial\eta}{\partial\xi}$$

$$i_s - \frac{\kappa}{\sigma}i_s = I_{cell} - \frac{\kappa}{L}\frac{\partial\eta}{\partial\xi}$$

$$i_s(1 - \frac{\kappa}{\sigma}) = I_{cell} - \frac{\kappa}{L}\frac{\partial\eta}{\partial\xi}$$

$$i_s = \frac{\sigma}{(\sigma - \kappa)}I_{cell} - \frac{\sigma\kappa}{L(\sigma - \kappa)}\frac{\partial\eta}{\partial\xi}. \tag{3.13}$$

Solving for $\frac{\partial\eta}{\partial\xi}$ in both the solid and solution currents yields

$$\frac{\sigma\kappa}{L(\kappa + \sigma)}\frac{\partial\eta}{\partial\xi} = i_e - \frac{\kappa}{(\kappa + \sigma)}I_{cell}$$

$$\frac{\partial\eta}{\partial\xi} = \frac{(\kappa + \sigma)L}{\sigma\kappa}i_e - \frac{L}{\sigma}I_{cell}, \tag{3.14}$$

and

$$\frac{\sigma\kappa}{L(\sigma - \kappa)}\frac{\partial\eta}{\partial\xi} = \frac{\sigma}{(\sigma - \kappa)}I_{cell} - i_s$$

$$\frac{\partial\eta}{\partial\xi} = \frac{L}{\kappa}I_{cell} - \frac{L(\sigma - \kappa)}{\sigma\kappa}i_s. \tag{3.15}$$

Equations (3.14) and (3.15) are now used with the boundary conditions for i_s and i_e as previously described. The Laplace transform is taken on both sides, again using the overbar notation for Laplace and the tilde notation for initial conditions. Equations (3.14) and (3.15) then become

$$\frac{\partial\bar{\bar{\eta}}}{\partial\xi} = \frac{(\kappa + \sigma)L}{\sigma\kappa}\bar{i_e} - \frac{L}{\sigma}\overline{I_{cell}} \tag{3.16}$$

$$\frac{\partial\bar{\bar{\eta}}}{\partial\xi} = \frac{L}{\kappa}\overline{I_{cell}} - \frac{L(\sigma - \kappa)}{\sigma\kappa}\bar{i_s}. \tag{3.17}$$

When $\xi = 0$, all current in Eq. (3.3) is attributed to i_s and $i_e = 0$. Evaluating Eq. (3.16) at $\xi = 0$, gives the expression

$$\left.\frac{\partial\bar{\bar{\eta}}}{\partial\xi}\right|_{\xi=0} = -\frac{L}{\sigma}\overline{I_{cell}}, \tag{3.18}$$

and when $\xi = L$, all current in Eq. (3.3) is attributed to i_e, $i_s = 0$, and Eq. (3.17) is evaluated at $\xi = L$ giving

$$\left.\frac{\partial\bar{\bar{\eta}}}{\partial\xi}\right|_{\xi=L} = \frac{L}{\kappa}\overline{I_{cell}}. \tag{3.19}$$

The derivative of Eq. (3.10) is easily determined to be

$$\frac{\partial \bar{\bar{\eta}}}{\partial \xi} = C_1 \Upsilon(s) \sinh(\Upsilon(s)\xi) + C_2 \Upsilon(s)\cosh(\Upsilon(s)\xi), \tag{3.20}$$

and Eqs (3.18) and (3.19), can now be directly used to obtain C_1 and C_2. First evaluating Eq. (3.20) at $\xi = 0$, and noting $\sinh(0) = 0$ and $\cosh(0) = 1$, gives

$$\left.\frac{\partial \bar{\bar{\eta}}(\xi,s)}{\partial \xi}\right|_{\xi=0} = -\frac{L}{\sigma}\overline{I_{\text{cell}}} = C_1 \Upsilon(s)\sinh(0) + C_2 \Upsilon(s)\cosh(0)$$

$$= 0 + C_2 \Upsilon(s)(1)$$

$$= C_2 \Upsilon(s),$$

and the first constant

$$C_2 = -\frac{L}{\sigma \Upsilon(s)}\overline{I_{\text{cell}}}.$$

Repeating for $\xi = 1$ and substituting for C_2 gives

$$\left.\frac{\partial \bar{\bar{\eta}}(\xi,s)}{\partial \xi}\right|_{\xi=1} = \frac{L}{\kappa}\overline{I_{\text{cell}}} = C_1 \Upsilon(s)\sinh(\Upsilon(s)) - \frac{L}{\sigma \Upsilon(s)}\overline{I_{\text{cell}}}\Upsilon(s)\cosh(\Upsilon(s))$$

$$= \frac{L}{\kappa}\overline{I_{\text{cell}}} = C_1 \Upsilon(s)\sinh(\Upsilon(s)) - \frac{L}{\sigma}\overline{I_{\text{cell}}}\cosh(\Upsilon(s)),$$

and then solving for C_1

$$\frac{L}{\kappa}\overline{I_{\text{cell}}} + \frac{L}{\sigma}\overline{I_{\text{cell}}}\cosh(\Upsilon(s)) = C_1 \Upsilon(s)\sinh(\Upsilon(s))$$

$$\frac{\frac{L}{\kappa}\overline{I_{\text{cell}}} + \frac{L}{\sigma}\overline{I_{\text{cell}}}\cosh(\Upsilon(s))}{\Upsilon(s)\sinh(\Upsilon(s))} = C_1$$

$$C_1 = \frac{\sigma L + \kappa L\cosh(\Upsilon(s))}{\kappa \sigma \Upsilon(s)\sinh(\Upsilon(s))}\overline{I_{\text{cell}}}.$$

Substituting C_1 and C_2 back into Eq. (3.10) to obtain

$$\bar{\bar{\eta}} = C_1\cosh(\Upsilon(s)\xi) + C_2\sinh(\Upsilon(s)\xi)$$

$$\bar{\bar{\eta}} = \frac{\sigma L + \kappa L\cosh(\Upsilon(s))}{\kappa \sigma \Upsilon(s)\sinh(\Upsilon(s))}\overline{I_{\text{cell}}}\cosh(\Upsilon(s)\xi) - \frac{L}{\sigma \Upsilon(s)}\overline{I_{\text{cell}}}\sinh(\Upsilon(s)\xi).$$

then factoring out the current $\overline{I_{\text{cell}}}$, combining fractions, and expanding the numerator gives

$$\frac{\bar{\bar{\eta}}}{\overline{I_{\text{cell}}}} = \frac{\sigma L + \kappa L\cosh(\Upsilon(s))}{\kappa \sigma \Upsilon(s)\sinh(\Upsilon(s))}\cosh(\Upsilon(s)\xi) - \frac{L}{\sigma \Upsilon(s)}\sinh(\Upsilon(s)\xi)$$

$$\frac{\bar{\bar{\eta}}}{\overline{I_{\text{cell}}}} = \frac{[\sigma L + \kappa L\cosh(\Upsilon(s))]\cosh(\Upsilon(s)\xi) - L\kappa\sinh(\Upsilon(s))\sinh(\Upsilon(s)\xi)}{\kappa \sigma \Upsilon(s)\sinh(\Upsilon(s))}$$

$$\frac{\bar{\bar{\eta}}}{\overline{I_{\text{cell}}}} = \frac{\sigma L\cosh(\Upsilon(s)\xi) + \kappa L\left[\cosh(\Upsilon(s))\cosh(\Upsilon(s)\xi) - \sinh(\Upsilon(s))\sinh(\Upsilon(s)\xi)\right]}{\kappa \sigma \Upsilon(s)\sinh(\Upsilon(s))},$$

and finally using the trig identity $\cosh(x)\cosh(xy) - \sinh(x)\sinh(xy) = \cosh(x - xy)$, where $x = \Upsilon(s)$ and $y = \xi$ yields the Laplace-domain expression

$$\frac{\bar{\bar{\eta}}(\xi,s)}{\overline{I_{\text{cell}}}} = L\frac{\sigma\cosh(\Upsilon(s)\xi) + \kappa\cosh\left[\Upsilon(s)(1-\xi)\right]}{\sigma\kappa\Upsilon(s)\sinh(\Upsilon(s))}. \tag{3.21}$$

Equation (3.21) is exactly the *Laplace-domain-potential* for any point within an electrode. It does not however, extend to the potential difference across the electrode. Neither does it make a distinction between the solution and solid parts of the electrode.

Before considering the entire electrode, it is worth noting the cross sectional area A remains contained in $I_{\text{cell}} = \frac{i_{\text{app}}}{A}$ but can be removed at any time and the applied current used instead as shown by

$$\frac{\bar{\bar{\eta}}(\xi,s)}{\overline{i_{\text{app}}}} = L\frac{\sigma\cosh(\Upsilon(s)\xi) + \kappa\cosh\left[\Upsilon(s)(1-\xi)\right]}{A\sigma\kappa\Upsilon(s)\sinh(\Upsilon(s))}.$$

3.2.3   Transfer Function for an Entire EDLC

To derive an expression for the potential across an entire EDLC, both electrodes and the separator need to be considered. The electrodes are assumed to be identical except in polarity thus allowing the total EDLC voltage to be written as the sum of two electrode voltages plus the separator voltage and given by

$$v_{\text{cell}} = 2v_{\text{electrode}} + v_{\text{sep}}.$$

The separator is considered to be entirely ohmic and only contributes a voltage when the EDLC is charging or discharging thus

$$v_{\text{sep}} = I_{\text{cell}}\frac{L_{\text{sep}}}{\kappa_{\text{sep}}}.$$

The voltage rise/drop across each electrode is the change across both the solid and solution phases of the electrode from the point in the solid when $\xi = 0$ to the point in the electrolyte when $\xi = L$ shown by

$$v_{\text{electrode}} = \phi_{\text{s}}\big|_{\xi=0} - \phi_{\text{e}}\big|_{\xi=1},$$

which can be further split into two sections by adding/subtracting the term $\phi_{\text{e}}\big|_{\xi=0}$, then expanding and rearranging to obtain

$$v_{\text{electrode}} = \left(\phi_{\text{e}}\big|_{\xi=0} - \phi_{\text{e}}\big|_{\xi=1}\right) + \left(\phi_{\text{s}}\big|_{\xi=0} - \phi_{\text{e}}\big|_{\xi=0}\right).$$

The second term is recognized as $\eta(\xi,t)|_{\xi=0}$, which has been already derived and is substituted

$$v_{\text{electrode}} = \left(\phi_e|_{\xi=0} - \phi_e|_{\xi=1} \right) + \eta(\xi,t)|_{\xi=0} . \tag{3.22}$$

To find an expression for ϕ_e, the full electrode equation Eq. (3.21) is differentiated

$$\frac{\partial \overline{\tilde{\eta}}}{\partial \xi} = \overline{I_{\text{cell}}} L \frac{\sigma \Upsilon(s) \sinh(\Upsilon(s)\xi) - \kappa \Upsilon(s) \sinh\left[\Upsilon(s)(1-\xi)\right]}{\sigma \kappa \Upsilon(s) \sinh(\Upsilon(s))}$$

and substituted into the Laplace transform of the solution current using equation Eq. (3.12)

$$\overline{i_e} = \frac{\kappa}{(\kappa+\sigma)} I_{\text{cell}} + \frac{\kappa\sigma}{L(\kappa+\sigma)} \frac{\partial \overline{\eta}}{\partial \xi}$$

$$\overline{i_e} = \frac{\kappa}{(\kappa+\sigma)} \overline{I_{\text{cell}}} + \frac{\kappa\sigma}{(\kappa+\sigma)L} L \frac{\sigma \Upsilon(s) \sinh(\Upsilon(s)\xi) - \kappa \Upsilon(s) \sinh\left[\Upsilon(s)(1-\xi)\right]}{\sigma \kappa \Upsilon(s) \sinh(\Upsilon(s))} \overline{I_{\text{cell}}}$$

$$\frac{\overline{i_e}}{\overline{I_{\text{cell}}}} = \frac{\kappa}{(\kappa+\sigma)} + \frac{\sigma \sinh(\Upsilon(s)\xi) - \kappa \sinh\left[\Upsilon(s)(1-\xi)\right]}{(\kappa+\sigma)\sinh(\Upsilon(s))}, \tag{3.23}$$

and is repeated for the solid current from Eq. (3.13) giving

$$\overline{i_s} = \frac{\sigma}{(\sigma-\kappa)} \overline{I_{\text{cell}}} - \frac{\sigma\kappa}{L(\sigma-\kappa)} \frac{\partial \overline{\eta}}{\partial \xi}$$

$$\overline{i_s} = \frac{\sigma}{(\sigma-\kappa)} \overline{I_{\text{cell}}} - \frac{\sigma\kappa}{L(\sigma-\kappa)} L \frac{\sigma \Upsilon(s) \sinh(\Upsilon(s)\xi) - \kappa \Upsilon(s) \sinh\left[\Upsilon(s)(1-\xi)\right]}{\sigma \kappa \Upsilon(s) \sinh(\Upsilon(s))} \overline{I_{\text{cell}}}$$

$$\frac{\overline{i_s}}{\overline{I_{\text{cell}}}} = \frac{\sigma}{(\sigma-\kappa)} - \frac{\sigma \sinh(\Upsilon(s)\xi) - \kappa \sinh\left[\Upsilon(s)(1-\xi)\right]}{(\sigma-\kappa)\sinh(\Upsilon(s))}. \tag{3.24}$$

Equations (3.23) and (3.24) are the transfer functions for the solid and solution parts of the electrode. These two equations are now substituted into Eqs. (3.1) and (3.2) and with a bit of manipulation will give the electrolyte and solid transfer functions. The general process first does the substitution

$$-\frac{\kappa}{L} \frac{\partial \overline{\phi_e}(\xi,t)}{\partial \xi} = \frac{\kappa}{(\kappa+\sigma)} \overline{I_{\text{cell}}} + \frac{\sigma \sinh(\Upsilon(s)\xi) - \kappa \sinh\left[\Upsilon(s)(1-\xi)\right]}{(\kappa+\sigma)\sinh(\Upsilon(s))} \overline{I_{\text{cell}}}$$

$$\frac{\partial \overline{\phi_e}(\xi,t)}{\partial \xi} = -\frac{L}{\kappa} \left[\frac{\kappa}{(\kappa+\sigma)} \overline{I_{\text{cell}}} + \frac{\sigma \sinh(\Upsilon(s)\xi) - \kappa \sinh\left[\Upsilon(s)(1-\xi)\right]}{(\kappa+\sigma)\sinh(\Upsilon(s))} \overline{I_{\text{cell}}} \right]$$

$$\frac{\partial \overline{\phi_e}(\xi,t)}{\partial \xi} = -\frac{L}{(\kappa+\sigma)} \overline{I_{\text{cell}}} - \frac{L\sigma \sinh(\Upsilon(s)\xi) - L\kappa \sinh\left[\Upsilon(s)(1-\xi)\right]}{\kappa(\kappa+\sigma)\sinh(\Upsilon(s))} \overline{I_{\text{cell}}}, \tag{3.25}$$

and then integrates the result across the electrode from $\xi = 1$ to $\xi = 0$, in the case of the electrolyte, to yield the electrolyte transfer function between the ends of the electrode as

$$\int_1^0 \frac{\partial \overline{\phi_e}(\xi,t)}{\partial \xi} d\xi = \int_1^0 \left(-\frac{L}{(\kappa+\sigma)} \overline{I_{\text{cell}}} - \frac{L\sigma \sinh(\Upsilon(s)\xi) - L\kappa \sinh[\Upsilon(s)(1-\xi)]}{\kappa(\kappa+\sigma)\sinh(\Upsilon(s))} \overline{I_{\text{cell}}} \right) d\xi$$

$$\left(\overline{\phi_e}|_{\xi=0} - \overline{\phi_e}|_{\xi=1} \right) = \frac{L}{\kappa+\sigma} \overline{I_{\text{cell}}} - \frac{L(\kappa-\sigma)\tanh\left(\frac{\Upsilon(s)}{2}\right)}{\Upsilon(s)\kappa(\kappa+\sigma)} \overline{I_{\text{cell}}} \tag{3.26}$$

$$\frac{\overline{\phi_e}}{\overline{I_{\text{cell}}}} = \frac{L}{\kappa+\sigma} - \frac{L(\kappa-\sigma)\tanh\left(\frac{\Upsilon(s)}{2}\right)}{\Upsilon(s)\kappa(\kappa+\sigma)} \tag{3.27}$$

Equation (3.22) can now be evaluated and the separator term added such that

$$v_{\text{cell}} = 2v_{\text{electrode}} + v_{\text{sep}}$$

$$v_{\text{cell}} = 2\left[\left(\phi_e|_{\xi=0} - \phi_e|_{\xi=1} \right) + \eta(\xi,t)|_{\xi=0} \right] + I_{\text{cell}} \frac{L_{\text{sep}}}{\kappa_{\text{sep}}}$$

$$v_{\text{cell}} = 2\left[\phi_e + \eta(\xi,t)|_{\xi=0} \right] + I_{\text{cell}} \frac{L_{\text{sep}}}{\kappa_{\text{sep}}}$$

and finally substituting Eqs. (3.21) and (3.27) in the Laplace-domain gives

$$\overline{V_{\text{cell}}} = \frac{2L}{\kappa+\sigma} \overline{I_{\text{cell}}} - \frac{2L(\kappa-\sigma)\tanh\left(\frac{\Upsilon(s)}{2}\right)}{\Upsilon(s)\kappa(\kappa+\sigma)} \overline{I_{\text{cell}}}$$
$$L\frac{\sigma\cosh(\Upsilon(s)\xi) + \kappa\cosh[\Upsilon(s)(1-\xi)]}{\sigma\kappa\Upsilon(s)\sinh(\Upsilon(s))} \overline{I_{\text{cell}}} \Bigg|_{\xi=0} + \overline{I_{\text{cell}}} \frac{L_{\text{sep}}}{\kappa_{\text{sep}}}.$$

The final steps are to replace $\overline{I_{\text{cell}}}$ with $\frac{\overline{i_{\text{app}}}}{A}$ and divide out $\overline{i_{\text{app}}}$ giving

$$\frac{\overline{V_{\text{cell}}}}{\overline{i_{\text{app}}}} = -\frac{2L}{A(\kappa+\sigma)} - \frac{2L(\kappa-\sigma)\tanh\left(\frac{\Upsilon(s)}{2}\right)}{A\Upsilon(s)\kappa(\kappa+\sigma)} + \frac{L_{\text{sep}}}{A\kappa_{\text{sep}}}$$
$$+ 2\frac{L\sigma\cosh(\Upsilon(s)\xi) + \kappa L\cosh(\Upsilon(s) - \Upsilon(s)\xi)}{A\sigma\kappa\Upsilon(s)\sinh(\Upsilon(s))} \Bigg|_{\xi=0}$$

Evaluating the last term at $\xi = 0$ and recalling $\cosh(0) = 1$ gives

$$\frac{\overline{V_{\text{cell}}}}{\overline{i_{\text{app}}}} = \frac{2L}{A(\kappa+\sigma)} - \frac{2L(\kappa-\sigma)\tanh\left(\frac{\Upsilon(s)}{2}\right)}{A\Upsilon(s)\kappa(\kappa+\sigma)} + 2\frac{L\sigma\cosh(0) + \kappa L\cosh(\Upsilon(s)0)}{A\sigma\kappa\Upsilon(s)\sinh(\Upsilon(s))} + \frac{L_{\text{sep}}}{A\kappa_{\text{sep}}}$$

$$\frac{\overline{V_{\text{cell}}}}{\overline{i_{\text{app}}}} = \frac{2L}{A(\kappa+\sigma)} - \frac{2L(\kappa-\sigma)\tanh\left(\frac{\Upsilon(s)}{2}\right)}{A\Upsilon(s)\kappa(\kappa+\sigma)} + 2\frac{L\sigma + \kappa L\cosh(\Upsilon(s))}{A\sigma\kappa\Upsilon(s)\sinh(\Upsilon(s))} + \frac{L_{\text{sep}}}{A\kappa_{\text{sep}}}. \tag{3.28}$$

Again combining and simplifying beginning with the elimination of the tanh term gives

$$\frac{\overline{V_{\text{cell}}}}{\overline{i_{\text{app}}}} = \frac{2L}{A\left(\kappa+\sigma\right)} + \frac{L_{\text{sep}}}{A\kappa_{\text{sep}}}$$
$$+ 2\frac{[L\sigma + \kappa L\cosh(\Upsilon(s))]\left((\kappa+\sigma) - L\sigma(\kappa-\sigma)\left[\frac{cosh(\Upsilon(s))-1}{\sinh(\Upsilon(s))}\right]\sinh(\Upsilon(s))\right)}{A\Upsilon(s)\kappa\sigma(\kappa+\sigma)\sinh(\Upsilon(s))},$$

then cancel the sinh terms and start to expand

$$\frac{\overline{V_{\text{cell}}}}{\overline{i_{\text{app}}}} = \frac{2L}{A\left(\kappa+\sigma\right)} + \frac{L_{\text{sep}}}{A\kappa_{\text{sep}}} + 2\frac{[L\sigma + \kappa L\cosh(\Upsilon(s))]\left((\kappa+\sigma) - (\kappa L\sigma - L\sigma^2)[\cosh(\Upsilon(s)) - 1]\right)}{A\Upsilon(s)\kappa\sigma(\kappa+\sigma)\sinh(\Upsilon(s))}.$$

Now finish expanding

$$\frac{\overline{V_{\text{cell}}}}{\overline{i_{\text{app}}}} = 2\frac{L\kappa\sigma + \kappa^2 L\cosh(\Upsilon(s)) + \kappa\sigma L\cosh(\Upsilon(s)) - \kappa\sigma L\cosh(\Upsilon(s)) + \kappa\sigma L + L\sigma^2\cosh(\Upsilon(s))}{A\Upsilon(s)\kappa\sigma(\kappa+\sigma)\sinh(\Upsilon(s))}$$
$$+ \frac{2L}{A\left(\kappa+\sigma\right)} + \frac{L_{\text{sep}}}{A\kappa_{\text{sep}}},$$

before collecting like terms to obtain the final Laplace-domain transfer function as

$$\frac{\overline{V_{\text{cell}}}}{\overline{i_{\text{app}}}} = \frac{2L}{A\left(\kappa+\sigma\right)} + \frac{L_{\text{sep}}}{A\kappa_{\text{sep}}} + \frac{4L\kappa\sigma + 2L(\kappa^2+\sigma^2)\cosh(\Upsilon(s))}{A\Upsilon(s)\kappa\sigma(\kappa+\sigma)\sinh(\Upsilon(s))}. \tag{3.29}$$

Equation (3.29) can now be used to determine the voltage across the entire EDLC when a current is applied. $\Upsilon(s)$ is repeated for convenience

$$\Upsilon(s) = \sqrt{s\frac{L^2aC\left(\kappa+\sigma\right)}{\kappa\sigma}} = \left(\sqrt{s}\right)\sqrt{\frac{L^2aC\left(\kappa+\sigma\right)}{\kappa\sigma}}. \tag{3.30}$$

3.2.4 Additional Transfer Function Notes

The above process developed a Laplace-domain transfer function for the impedance across an entire EDLC cell including two electrodes and the separator. During the derivation, additional transfer functions for the solution and solid currents were also developed as Eqs. (3.23) and (3.24). A transfer function was also obtained for the electrolyte part of the electrode, see Eq. (3.27). These additional transfer functions are not used anywhere in this dissertation but may be appropriate for use in other works studying the internal dynamics of EDLCs. The additional transfer functions can be used to predict the potential at any point or boundary within the super-capacitor and while currently only derived for a 1-d model, could also be extended to two or three dimensions.

The transfer functions all remain in the frequency-domain and will need to be transformed to the time-domain for relevant simulations. These transfer functions, however, contain transcendental terms not so easily transformed and if the transform route most commonly taken is followed, series expansions, truncations, and infinite sums must be employed to give meaningful results. An alternate method will therefore be used to generate a discrete-time state-space model that is simple to simulate. First however, a numeric solution to the original five equations will be presented as a method of validation.

3.3   Full Order Model Simulation

The original five governing equations can be numerically solved using a full order model (FOM) solver such as COMSOL. The numerically exact solution can be used to validate other solution methods. The COMSOL FOM consists of three distinct but contiguous regions forming a continuum of two identical electrodes and a separator. Each of the five equations are treated differently in each of the three regions

3.3.1   FOM Modeling Regions

To implement the FOM in COMSOL, the five governing equations must be tailored to fit a format that COMSOL knows how to handle. The EDLC is divided into three distinct regions containing the two electrodes and separator. All model parameters are present in all regions but are assigned different meanings and values for each region. For example, the capacitance in the separator region doesn't really exist but as other parameters may be expressed with the separator capacitance as a factor, it is set to unity thus having no real effect in that region. The general reformulation process, to make things COMSOL friendly, is given next.

3.3.1.1   Equations for the Potential ϕ_s, in the Carbon part of the Electrodes

First, rewrite Eqs. (3.4), and (3.5) as

$$\frac{\partial i_s}{\partial x} = a i_{dl}$$

$$i_{dl} = -C \frac{\partial (\phi_s - \phi_e)}{\partial t}.$$

Then combine by eliminating the common i_{dl} term to give

$$\frac{1}{a}\frac{\partial i_{\mathrm{s}}}{\partial x} = -C\frac{\partial \phi_{\mathrm{s}}}{\partial t} + C\frac{\partial \phi_{\mathrm{e}}}{\partial t},$$

then substituting Eq. (2.1) gives

$$\frac{1}{a}\frac{\partial}{\partial x}(-\sigma\frac{\partial \phi_{\mathrm{s}}}{\partial x}) = -C\frac{\partial \phi_{\mathrm{s}}}{\partial t} + C\frac{\partial \phi_{\mathrm{e}}}{\partial t}.$$

Next re-arranging and re-notating, the equation becomes

$$-C\frac{\partial \phi_{\mathrm{s}}}{\partial t} = -C\frac{\partial \phi_{\mathrm{e}}}{\partial t} - \frac{1}{a}\frac{\partial}{\partial x}(\sigma\frac{\partial \phi_{\mathrm{s}}}{\partial x})$$

$$\frac{\partial \phi_{\mathrm{s}}}{\partial t} = \frac{\partial \phi_{\mathrm{e}}}{\partial t} + \frac{1}{aC}\frac{\partial}{\partial x}(\sigma\frac{\partial \phi_{\mathrm{s}}}{\partial x})$$

$$aC\frac{\partial \phi_{\mathrm{s}}}{\partial t} - \nabla \cdot \sigma(\frac{\partial \phi_{\mathrm{s}}}{\partial x}) = aC\frac{\partial \phi_{\mathrm{e}}}{\partial t},$$

and finally normalizing to L, the final form suitable for implementing in *both* electrodes is

$$aCL\frac{\partial \phi_{\mathrm{s}}}{\partial t} - \nabla \cdot (\frac{\sigma}{L}\frac{\partial \phi_{\mathrm{s}}}{\partial x}) = aCL\frac{\partial \phi_{\mathrm{e}}}{\partial t}. \tag{3.31}$$

3.3.1.2 Equations for the Potential ϕ_{e}, in the Electrolyte Part of the Electrodes

By a nearly identical approach, an equation for the potential in the electrolyte part of the two electrodes, ϕ_{e} is developed as

$$aCL\frac{\partial \phi_{\mathrm{e}}}{\partial t} - \frac{\kappa}{L}\nabla \cdot \left(\frac{\partial \phi_{\mathrm{e}}}{\partial x}\right) = aCL\frac{\partial \phi_{\mathrm{s}}}{\partial t}, \tag{3.32}$$

and can be used for both of the two electrodes.

3.3.1.3 Equations for the Separator

The potential in the separator is entirely contained in the electrolyte potential ϕ_{e} because the solid electrode region does not extend into the separator. Therefore, in the separator region, the equation becomes

$$aCL\frac{\partial \phi_{\mathrm{e}}}{\partial t} - \frac{\kappa}{L}\nabla \cdot \left(\frac{\partial \phi_{\mathrm{e}}}{\partial x}\right) = 0. \tag{3.33}$$

Neither the solid current density i_{s}, nor the solid potential ϕ_{s}, have meaning in the separator region hence Eq. (3.31) does not exist in the separator. The capacitance C is redefined to the value 1, and the DL surface area a is redefined to zero leaving only the separator resistance defined by

$$R_{\mathrm{sep}} = \frac{L_{\mathrm{sep}}}{\kappa_{\mathrm{sep}}}$$

3.3.1.4 Boundary Values and Initial Conditions

Both potentials, ϕ_s and ϕ_e, are initially set to zero at all locations across the electrodes and separator. Boundary conditions need to be set at the current collector-electrode interface where $x = 0$ and the separator-electrode interface where $x = L$.

At the current collector-electrode interface, all applied current is electronic and is entirely contained in i_s therefore

$$\frac{\partial \phi_s}{\partial x}\bigg|_{x=0} = -\frac{i_s L}{\sigma A}$$

and at the separator-electrode interface, all applied current is electronic and is entirely contained in i_e therefore

$$\frac{\partial \phi_e}{\partial x}\bigg|_{x=L} = -\frac{i_e L}{\kappa A}.$$

3.3.2 FOM Simulation Results

A step input simulation using somewhat arbitrary parameter values was performed with COMSOL. The results can be seen in Fig. 3.1. The magnitude of the step input is somewhat deceiving because the simulation uses current per unit surface area and not the total applied current.
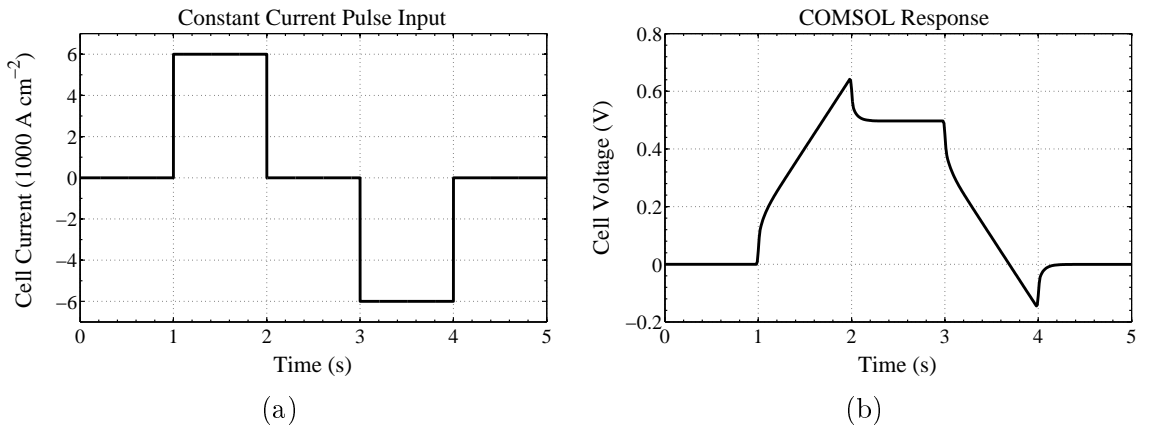
Figure 3.1: COMSOL simulation: (a) Input (b) Output

3.4 Developing the reduced-order Model

The transfer functions developed as Eqs. (3.29), (3.28), (3.27), (3.25), and (3.24) are somewhat complex but not to the point of being overwhelming. Adding additional variables such as temperature might increase the complexity somewhat, but the equations would still be manageable. Transforming the equations back to the time domain is the next problem. The frequency-domain form is good for certain simulations but time-domain simulations are needed.

Equation (3.29) is in the Laplace-domain and needs to be transformed back into the time-domain. The difficulty in this case, is that it contains hyperbolic functions. Hyperbolic, as well as standard trigonometric functions, are combinations of exponential functions and obtaining closed form time-domain representation requires the truncation of an infinite sum. Srinivisan, in his 1999 efforts, breaks the transfer function into several fractions and then uses trigonometric expansion to handle each of the transcendental functions [28]. Series truncation is then used to enable simulations to be accomplished.

This dissertation uses an alternate method. To obtain a time-domain state-space realization of the transfer function, a process introduced by Lee [4], is used. Lee used the deterministic Ho-Kalman algorithm [50], developed in the mid 1960s, to take a discrete-time pulse response and transform it into a discrete-time state-space system. The process is now known as the discrete-time realization algorithm (DRA). The DRA was originally developed for use with lithium-ion cells but because EDLCs are very similar to lithium-ion cells, it is easily adapted to handle an EDLC. The result is a reduced-order model in the time-domain, *state-space* form. The general process, while not the primary focus, is based on the idea that with knowledge of a systems impulse response, everything is known about the system to predict its output given any input.

The next several sections detail the DRA process as applied to Eq. (3.29) and the chapter ends with a successful validation of the new, theoretical ROM (T-ROM), against the FOM.

3.4.1 Discrete-Time Realization Algorithm

The four basic steps in obtaining a ROM using the DRA are given next:

1. Sample the continuous-time transfer function, $H(s)$, or Eq. (3.29), in the frequency domain at a frequency T_s, and take the inverse discrete Fourier transform (IDFT) to get an *approximation* to the continuous time impulse response $h(t)$.

    (a) Use a Bode plot or other methods to determine an adequate sampling frequency, T_s.

    (b) If an integrator pole at $s = 0$ is indicated, remove pole by the residue method before sampling $H(s)$.

2. Compute the continuous-time step response, $h_{\text{step}}(t)$, values from the continuous-time impulse response $h(t)$ by a summation process.

3. Compute the discrete-time unit-pulse response $h[k]$ from the continuous-time step response $h_{\text{step}}(t)$.

4. Generate a discrete-time state-space realization using the deterministic Ho–Kalman algorithm. This algorithm returns the reduced-order A, B, and C matrices from the discrete-time pulse response sequence in Step 3. The order of the system is determined from the ordered singular values of the Hankel matrix computed as part of the algorithm. The D matrix is found by the initial value theorem.

5. Re-insert the integrator pole from the pre-conditioning step, if necessary.

3.4.1.1 DRA Step 1

A Bode plot of Eq. (3.29) shows it is unstable near the origin due to an integrator pole at the origin and can be seen in Fig. 3.2(a). The integrator pole makes the system unstable and also unsuitable for the application of the DRA. To correct the stability problem, the integrator pole is removed by finding the function residue and subtracting it from the transfer function $H(s)$. Multiplying an s term with $H(s)$ cancels the pole, and taking the limit as s approaches zero leaves only the residue. The residue, divided by s, is subtracted from $H(s)$
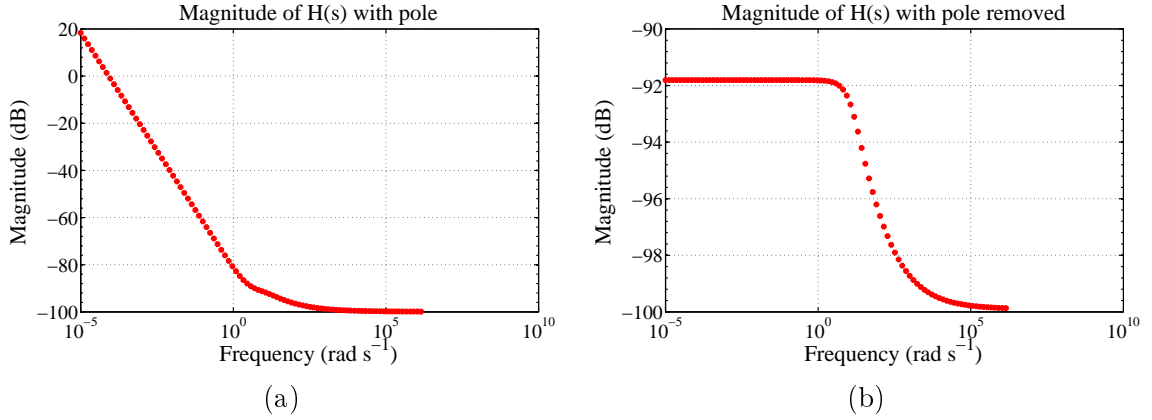
Figure 3.2: Bode plot of transfer functions: (a) $H(s)$ with pole (b) $H^*(s)$ with pole removed

leaving $H^*(s)$, that is now suitable for application of the DRA process. The residue will be re-added later, to the C term, in the DRA process.

The residue of Eq. (3.29) is easily be determined using Mathematica as

$$Res_0 = \lim_{s \to 0} sH(s) = \frac{2}{CaL}$$

and to obtain $H^*(s)$

$$H^*(s) = H(s) - \frac{Res_0}{s}, \tag{3.34}$$

or in expanded form as

$$H^*(s) = \frac{2L}{A(\kappa + \sigma)} + \frac{L_{\text{sep}}}{A\kappa_{\text{sep}}} + \frac{4L\kappa\sigma + 2L(\kappa^2 + \sigma^2)\cosh(\Upsilon(s))}{A\Upsilon(s)\kappa\sigma(\kappa + \sigma)\sinh(\Upsilon(s))} - \frac{2}{sCaL}.$$

Graphically, this is illustrated by the Bode plots shown in Fig. 3.2. In (a), as the frequency approaches zero, $H(s)$ clearly grows towards infinity indicating the presence of an integrator pole at the origin. Plot (b), is the same system but with the pole removed and shows $H^*(s)$, as exactly the same plot but with integrator pole removed. The pole will be added back in to the C-term at the end of the DRA process. $H^*(s)$ can now be sampled and a continuous time result obtained. Note the high frequency region is unchanged in both plots with a lower limit near -100 dB.

The next DRA step requires the continuous-time impulse response so the transfer function with pole removed, or $H^*(s)$, is re-sampled using the bilinear transfrom at 100 kHz,
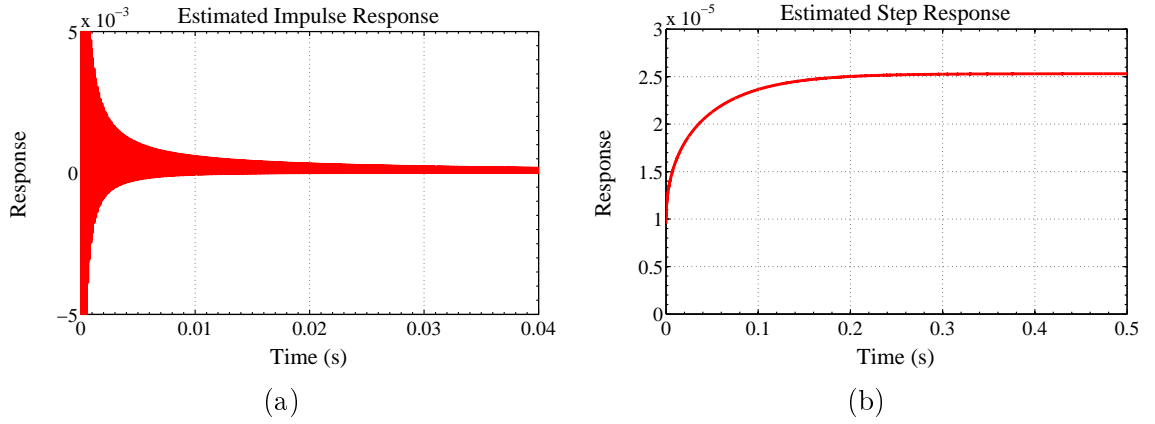
Figure 3.3: Approximate responses: (a) Impulse (b) Step

and the inverse DFT is performed to obtain an estimated continuous-time impulse response as shown in Fig. 3.3(a).

3.4.1.2 DRA Step 2

An estimated time-domain step response can be obtained by cumulatively summing the estimated impulse response. It can also bee seen that Fig. 3.3uses two time scales because the initial decay of the impulse is very fast.

3.4.1.3 DRA Step 3

The Ho–Kalman deterministic algorithm requires the discrete time pulse response as shown in Fig. 3.4. Therefore the estimated continuous-time step response $h_{\text{step}}(t)$, is sampled to compute the discrete-time unit-pulse response

$$h_{\text{Pulse}}[k] = h_{\text{step}}[k] - h_{\text{step}}[k-1].$$
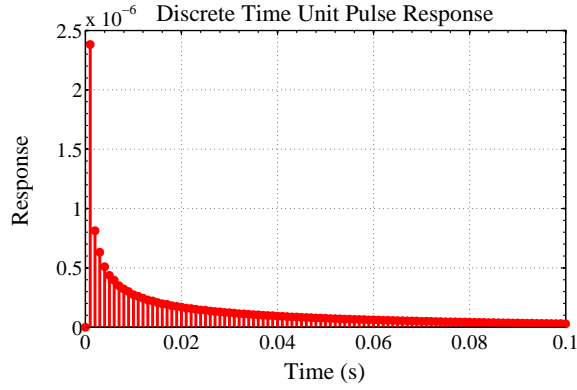
Figure 3.4: Discrete time pulse response

TABLE 3.1: Singular values with RMS error

n	1	2	3	4	5	6
RMS Error	$19.27\,\mathrm{mV}$	$6.59\,\mathrm{mV}$	$2.81\,\mathrm{mV}$	$2.48\,\mathrm{mV}$	$2.485\,\mathrm{mV}$	$2.492\,\mathrm{mV}$

3.4.1.4   DRA Step 4

The final step in the DRA is to create a state-space realization from the approximate discrete-time pulse response from Step 3. The deterministic Ho–Kalman algorithm can then be used to obtain a state-space realization with the standard form of

$$x[k+1] = Ax[k] + Bu[k]$$
$$y[k] = Cx[k] + Du[k].$$

The method relies heavily on work first presented in 1966 by Ho and Kalman [50], and a recent application of those methods by Lee [4,50], in order to describe the EDLC in state-space form. The order of the model can be estimated by evaluating the singular values. In this case, the first six SVDs are sufficient to describe the system. Additional values can be included, however they contribute very little to the final result and are not considered further.

Figure 3.5 shows the first 50 singular values but since the plot is not clear what number to use for n, Table 3.1 is used to obtain an n value of 5 or 6 as simulations using higher values for n do not show significant improvements to the final result. Therefore, an n of 6 is used in the final step of the DRA process.
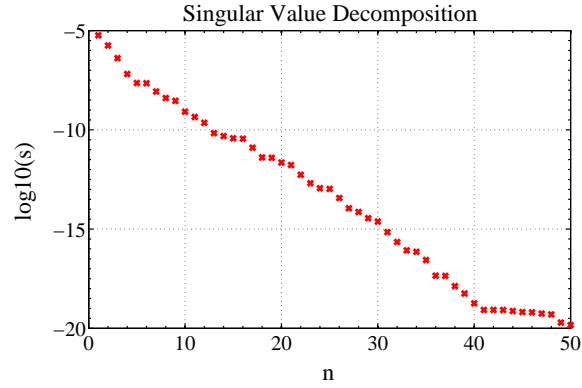
Figure 3.5: Plot of 50 SVD values

Finally, the integrator pole previously removed, is reinserted into the C matrix by prepending the residue, $Res_0 = \frac{2}{CaL}$, at the beginning of the matrix. The D term is then obtained by finding the limit

$$D = \lim_{s \to \infty} H^*(s) = \frac{2L\kappa_{\mathrm{sep}} + L_{\mathrm{sep}}(\kappa + \sigma)}{\kappa_{\mathrm{sep}}(\kappa + \sigma)}.$$

The final DRA model state-space representation matrices *A, B, C, and D* are summarized as

$$A = \begin{bmatrix} 1 & 0 & 0 & 0 & 0 & 0 \\ 0 & 0.8945 & 0.2309 & 0.0596 & -0.01132 & 6.4016 \times 10^{-4} \\ 0 & 0.2039 & 0.3728 & -0.3306 & 0.1017 & -0.0067 \\ 0 & 0.0596 & -0.3306 & 0.6112 & 0.2492 & -0.0297 \\ 0 & -0.0132 & 0.1017 & 0.2492 & 0.5197 & 0.1761 \\ 0 & -6.4016 \times 10^{-4} & 0.0067 & 0.0297 & -0.1761 & -0.6748 \end{bmatrix}$$

$$B = \begin{bmatrix} 0.0010 \\ -0.0010 \\ 0.0011 \\ 2.0116 \times 10^{-4} \\ -2.1005 \times 10^{-5} \\ 8.8184 \times 10^{-7} \end{bmatrix}$$

$$C = \begin{bmatrix} 8.2869 \times 10^{-5} & -0.0010 & 0.0011 & 2.0116 \times 10^{-4} & -2.1005 \times 10^{-5} & 8.8184 \times 10^{-7} \end{bmatrix}$$

$$D = \begin{bmatrix} 1.0117 \times 10^{-5} \end{bmatrix}$$

3.5 Reduced Order Model versus Full Order Model Validation

To validate the DRA process, the RMS error between the FOM and the DRA generated ROM is calculated giving an error of about 2.4mV. The primary region contributing to the error can be seen in Fig. 3.6(b), (c), and (d). The majority of the error can be attributed to the way in which COMSOL handles discontinuities. A second source of error is from the DRA process itself. Step 4 uses a truncation of the singular value matrix causing the ROM to remain small but at the cost of a small amount of accuracy loss. Third, as the error is calculated over a specific *time*, errors occuring at time x, are likely to be present from that point on thus skewing the error calculation. Chapter 4 will introduce an improved method to calculate error.
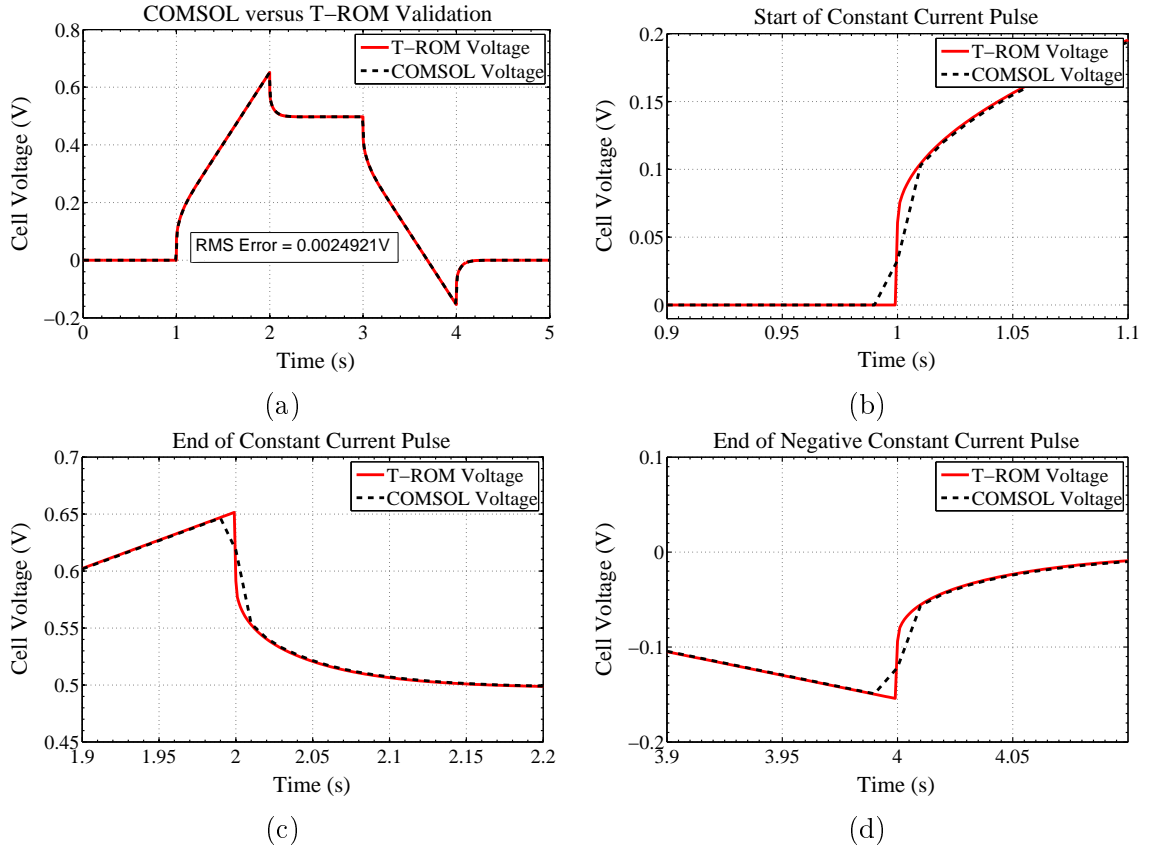
Figure 3.6: ROM versus FOM Validation: (a) Full comparison, (b) Zoom to maximum error region

As the primary source of error has been identified as a simulation artifact and occurs only near discontinuity points, the error is not considered relevant.

3.6 Summary

Chapter 3 began with a set of five interrelated PDE equations governing the voltage across an EDLC when excited by a current. These equations formed the basis for the derivation of a set of transfer functions capable of modeling an EDLC in the time or frequency domains. The transfer function for the complete EDLC was transformed to a time-domain state-space model and used to validate the entire DRA process as applicable to an EDLC. Additional transfer functions were developed during the derivation process but were not put through

the DRA process. These additional transfer functions can, as needed, be used to predict the states of variables or internal components at any location or time within the EDLC.

Chapter 3 developed a ROM of the complete EDLC and successfully validated the ROM against the numeric solution produced by the PDE solver COMSOL. As seen in Fig. 3.6, the ROM validates quite nicely against the FOM.

The estimated parameter values used here were obtained from multiple sources but in general, remain somewhat arbitrary and do not represent any specific device. As long as the same parameter set is used, however, the results from the FOM and ROM should be nearly identical. If however, validation is required against a real device, actual parameter values are needed and therein lies the problem. This level of parametric data is generally not available from data sheets and provides the motivation for develop a method, shown in Chap. 4 by which internal parameter values can be estimated from simple current-voltage measurements.

CHAPTER 4

Identification of EDLC Parameters

4.1 Introduction

In Chap. 3, several EDLC transfer functions were developed, and using the DRA process, a
state-space realization ROM was obtained and successfully validated against a FOM. The
model however, does not directly apply to any specific EDLC. Some of the parameters are
assumed from earlier works while others are just guesses based on handbook data, product
data sheets, and online reference tables. For the pure purpose of validating the ROM creation
process against the FOM, these somewhat arbitrary parameters are sufficient but for real
applications, real parameter values are needed. Creating a useable ROM representation
of a real device therefore, requires having accurate and, if possible, validated parameters.
Chapter 4 addresses this requirement by demonstrating a process through which parameters,
identified from simple current and voltage measurements, can be used to develop a set of
parameters, sufficiently accurate, to create and execute a ROM that matches the behavior
of a real device.

The general identification process is first carried out on a simple Randles cell to demon-
strate the general procedure. Next, a method to express the EDLC transfer functions in
terms of circuit elements, such as resistors and capacitors, is presented. Then, with the
transfer function written in terms of measurable circuit elements, a measured value ROM,
or M-ROM, can easily be created matching the original device. Furthermore, using the mea-
sured data, a method of determining the internal parameter set will also be discussed and
illustrated. Thus, two sets of data are obtained: (a) the measured circuit-form data suitable
for creating a M-ROM, and (b) data that can be used to populate the internal parameter
list as shown in Table 4.1.

First however, as part of any parameter identification, there is a validation requirement. To obtain a set of *control data,* the ROM from Chap. 3 is executed with a constant current pulse as input thus generating the needed *control* set of current-voltage data points as shown in Fig. 3.6(a). The control data now forms a basis from which measurements can be taken and parameters extracted. As the true parameter values are known, they provide the validation data used to compared against the measured data. The data extracted from current and voltage measurements, will also be shown to be sufficient to execute the M-ROM without any knowledge of the parameter values in Table 4.1.

Finally, because there may be modeling applications that *do* require the actual physical parameter values, a best fit non-linear least squares optimization process is used to refine the internal parameters extracted from the measured data. Chapter 5 then expands the identification process by deconstructing a commercially available device and obtaining the needed dimensional information to identify nearly all of the Table 4.1 parameter values.

4.1.1 Parameters of Interest

Chapter 3 used the parameters listed in Table 4.1 to execute the ROM and FOM simulations. Temperature is not considered a device parameter although its effect will discussed in Chap. 6. For now, none of the models include temperature. The cross sectional area A, is also added but was normalized out of the Chap. 3 simulations. It will be useful however, as other parameters are extracted. Brief parameter descriptions are included following the parameter table.

Conductivity

Conductivity in an EDLC is primarily a function of how well ions or electrons are able to move in the electrolyte or solid regions of the electrode and how well ions can move across the separator region. The *specific* conductivity in activated carbon, σ, has the highest value as electrons can move within the carbon material easily. The specific conductivities for the electrolyte are κ and κ_{s} denoting the electrode and separator regions. Both regions are saturated with the same acetonitrile solution but the solid material in each region is affected differently thus the two conductivity parameters.

TABLE 4.1: Original parameter values

Parameter	Description	Estimated T-ROM values	Units	Data Source
σ	Effective solid conductivity in the electrode	2000	$\mathrm{s\,m^{-1}}$	[51,52]
κ	Effective electrolyte conductivity in the electrode	5	$\mathrm{s\,m^{-1}}$	[19]
L	Length of electrode	0.0001173	m	Measured
C	Capacitance per unit area	0.0833	$\mathrm{F\,m^{-2}}$	Estimated
L_s	Length of separator	2.5	$\mu\mathrm{m}$	Measured
κ_s	Effective conductivity in the separator	5	$\mathrm{s\,m^{-1}}$	Set to κ
a	Specific interfacial electrode area	2.47×10^9	$\mathrm{cm^2\,cm^{-3}}$	Estimated
A	Cross sectional area	248	$\mathrm{cm^2}$	Measured

Electrode Dimensions

Length, width, and height of the electrode and separator play a role when determining specific current. The electrodes can be measured in three dimension giving length, width, and height. The dimensional values are used to estimate the cross sectional area A. Length, as used in the majority of this dissertation, refers to the very small distance between the current collector and separator and can easily be confused, in terminology, with the width or height. These dimensions are not to be confused with the DL interfacial surface area a.

As an additional note, the model is described as 1-d. When applying the model to a real device though, the extension to a third dimension is not significant to the current density or electrode potential and therefore can remain 1-d even though it is used to represent a 3-d device.

Capacitance

The specific capacitance C as used in the table refers to the DL capacitance of a single electrode. Equation (1.2) may be *carefully* used for total device capacitance with the ε term being contained in the capacitance per unit area from the Table 4.1.

Double Layer Interfacial Surface Area

The specific interfacial surface area a, is the actual surface area separating the solid and electrolyte. It cannot be easily measured and Chap. 5 will present a process to estimate its value.

4.2 Circuit Element Representation

EDLCs can be represented by both physics and circuit based models. Circuit-based models are common, relatively easy to simulate, and transfer functions can be readily obtained using well known methods. Physics models would seem to have a disadvantage as they don't have a circuit from which to obtain a transfer function. With a circuit-element based transfer function, all that is needed to perform simulations are the circuit element values. This chapter demonstrates a method to rewrite the transfer functions from Chap. 3, in a form that *looks* like it was obtained from an actual circuits. Voltage and current measurements are taken from an EDLC waveform and used to obtain values sufficient to populate the new circuit-model. An M-ROM is then created and is shown to accurately model an EDLC. The next section illustrates the general idea using a simple Randles cell before applying the process to an EDLC.

4.2.1 Randles Cell Example

A Randles cell is probably the simplest circuit used to model EDLCs. It's not actually a very good model, but is ideal for illustrating the parameter identification *process* that will later be used on much more complex models.

To begin, the circuit as shown in Fig. 4.1(a) is simulated using Spice. The input is the same constant current pulse as used in Chap. 3 consisting of a 0 V rest time followed by the input constant current pulse. The output is shown in Fig. 4.1(b). The circuit was simulated with $R_s = 50\,m\Omega$, $R_p = 1\,M\Omega$, and $C = 150\,F$. The input current pulse amplitude was set to 10 A. R_s is the series or ESR resistance, R_p is the leakage or parallel resistance and must be present for the Spice model to simulate. C is the device capacitance.
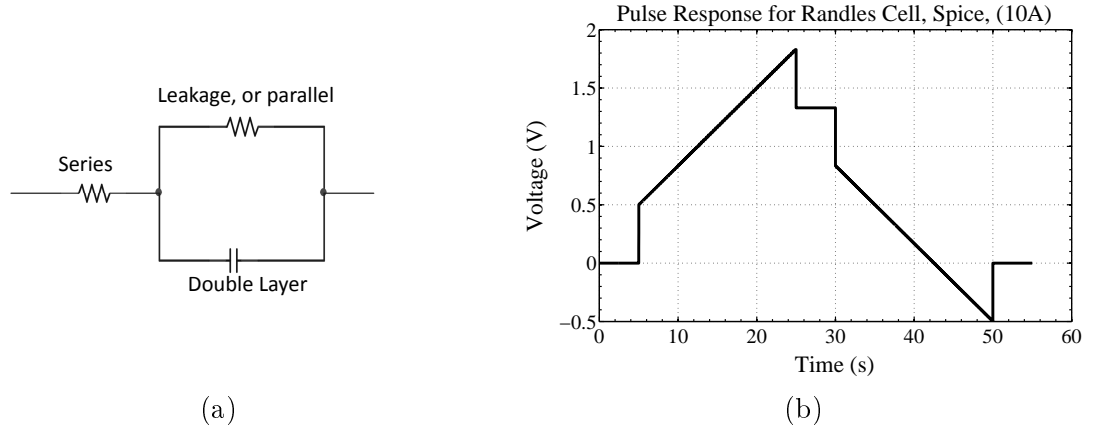
Figure 4.1: Randles cell: (a) Schematic (b) Pulse response
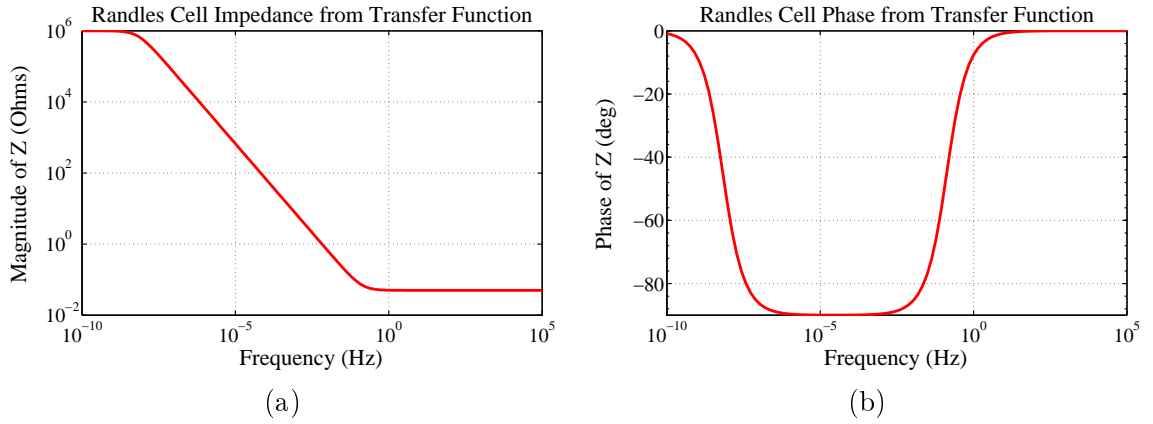
Figure 4.2: Bode plot of Randles cell: (a) Magnitude of impedance (b) Phase

The simulation output looks somewhat like the outputs of the ROM and FOM from Chap. 3. Its certainly a simplified model and clearly lacks the more realistic shapes of the FOM or ROM. Although the Randles cell could be improved by adding additional components, the goal is to simply illustrate the analysis process and therefore the basic circuit is sufficient.

The transfer function for the circuit can be easily determined as

$$Randles_{\text{impedance}} = \frac{sCR_{\text{s}}R_{\text{p}} + R_{\text{s}} + R_{\text{p}}}{sCR_{\text{p}} + 1}, \tag{4.1}$$

and as long as the three parameter values are known, Spice or MATLAB, can easily generate a Bode plot as shown in Fig. 4.2.

If the transfer function is known but the parameter values are not , current and voltage measurements, along with frequency data, can be used to obtain the parameter values. This is especially useful for a known, or partially known, transfer function of a circuit in a black box. Assume a Randles circuit was constructed by someone and left in a locked black box with only one wire in and one wire out. Can the component values be obtained using only these two test leads along with some voltage and current measurements? Obviously, the answer is yes and the process is now shown.

4.2.2 Randles Cell Analysis

Assuming the transfer equation Eq. (4.1), sans component values, is known to be accurate, the pulse plot, impedance plot, and phase plot, can all easily be obtained through simple lab tests.

First, the pulse plot in Fig. 4.1(b), shows a noticeable jump of $500\,\mathrm{mV}$ at the instant the pulse is applied. Knowing the applied current is $10\,\mathrm{A}$, and with Ohm's law, a resistance of about $50\,\mathrm{m\Omega}$ is estimated. Second, during the middle of the pulse when the current is constant, the voltage seems to increases in a linear fashion and Eq. (1.3), used with the dc current of $10\,\mathrm{A}$, can be applied to estimate the capacitance as

$$C = I_{\mathrm{dc}} \frac{\mathrm{d}t}{\mathrm{d}v} = (10\,A) \left(\frac{(25-5)\,\mathrm{s}}{(1.83-.5)\,\mathrm{V}} \right) = 150\,\mathrm{F}. \tag{4.2}$$

The Bode plot in Fig. 4.2 indicates that at very high and very low frequencies, the impedance is entirely resistive having the two values $10^6\,\Omega$ and $50\,\mathrm{m\Omega}$. Finally, the transfer function can be solved easily for C

$$Randles_{\mathrm{impedance}} = \frac{sCR_{\mathrm{s}}R_{\mathrm{p}} + R_{\mathrm{s}} + R_{\mathrm{p}}}{sCR_{\mathrm{p}} + 1}$$
$$C = \frac{sCR_{\mathrm{p}}R_{\mathrm{s}} + R_{\mathrm{s}} + R_{\mathrm{p}}}{sR_{\mathrm{p}}Randles_{\mathrm{impedance}}},$$

and now evaluated at any desired s to give a value for C identical to Eq. (4.2).

In the Randles cell example, using only data from the pulse response and EIS plots, nearly exact values are obtained that match the Randles circuit. If uncertainty exists in the newly extracted component values, the measured data can be optimized against the true data and adjusted until the simulation data and real data match.

The relevant question is whether the same approach can be taken with the physics-based ROM developed in Chap. 3. No circuit elements exist in the transfer function and the original set of PDE equations did not come from a physical circuit.

4.3   Circuit Elements as Applied to the EDLC

Table 4.1 lists eight internal parameters not directly measurable using standard electronics lab equipment. Values for some of the eight might be obtained by physical tests including X-ray diffraction, (XRD), scanning electron microscopy (SEM), or maybe a well placed phone call to the manufacturer. A much simpler approach would be preferred.

If the transfer equation for an EDLC can be re-written in terms of only resistors and capacitors, and if values for those components can be obtained, as was done for the Randles cell example, the problem would be much simpler. This section derives a process to develop a circuit-element like transfer function and demonstrates how values can be obtained for the resulting resistor and capacitor model. The process is similar to that done for the Randles cell.

As there are no circuit elements directly used in the transfer function, the first task is to define several circuit elements that can be used to transform the transfer equation into a form that *looks* like it was obtained from a circuit. To obtain actual values, groups of internal parameters are considered. If the voltage at specific simulation times is measured, and combined with a known dc current, a value for resistance or capacitance can be calculated and assigned to a *group* of internal parameters. The resulting circuit-like values are used to then populate the circuit-element version of the transfer function. The ROM created from the measured value transfer equation is given the term M-ROM.

A a concluding note in the analysis, the metal current collectors, wire leads, and metal contact tabs are assumed to have purely ohmic resistance values on the order of $2.7 \times 10^{-8} \, \text{m}\Omega$ [53,54]. They are therefore informally lumped together with the ohmic separator resistance but do not contribute significantly to its actual value.

4.3.1 Separator Resistance

The separator consists of a porous paper or other membrane saturated with electrolyte such that ions in the electrolyte are able to pass through but electrons are not. The conductivity of the separator is a function of the electrolyte ion mobility and size, the porosity of the separator, and its physical structure. For simplicity, all of these factors are combined into a single *specific* conductivity value. The separator resistance is typically small, is considered entirely ohmic, is always present, and is considered a constant. The length in the x direction, the EDLC cross sectional area, and the electrolyte conductivity in the separator, are all combined to produce a *total* value for the separator resistance as

$$R_{\text{sep}} = \frac{L_{\text{sep}}}{A\kappa_{\text{sep}}}. \tag{4.3}$$

Although R_{sep} is purely ohmic and a constant, it cannot be directly measured as there is no physical access to the separator. A quick unit analysis shows the units of R_{sep} are ohms as the *specific* conductivity, is in $\text{s}\,\text{m}^{-1}$.

4.3.2 Instantaneous Resistance

When a current is suddenly applied to an EDLC, as with a step input, there is an immediate response in the EDLC voltage. This response, also known as the impulse response, occurs mathematically, immediately following the change in input. By evaluating the EDLC transfer function at an infinite, or at least very high frequency, an expression for the *instantaneous resistance* can be obtained as

$$R_{\text{i}} = \lim_{s \to \infty} \left[\frac{2L}{A\left(\kappa + \sigma\right)} + \frac{L_{\text{sep}}}{A\kappa_{\text{sep}}} + \frac{4L\kappa\sigma + 2L\left(\kappa^2 + \sigma^2\right))\cosh(\Upsilon(s))}{A\Upsilon(s)\kappa\sigma(\kappa + \sigma)\sinh(\Upsilon(s))} \right]$$

$$R_{\text{i}} = \frac{2L}{A\left(\kappa + \sigma\right)} + \frac{L_{\text{sep}}}{A\kappa_{\text{sep}}}.$$

The initial value theorem states that when frequency is infinite, time is zero and therefore R_{i} is denoted the instantaneous resistance. Note that R_{sep} is included in the equation as it has no frequency component, which is the definition of a constant. A second method of obtaining the instantaneous resistance is to consider not only R_{sep}, but also the resistance in a single electrode characterized by the parallel combination of the solid and electrolyte

conductivities. The electrode length and cross sectional area are used to obtain an expression for the instantaneous resistance of a single electrode while R_{sep} is only added when the entire cell is considered

$$R_{\text{instant}} = \frac{L}{A\,(\kappa + \sigma)}, \tag{4.4}$$

and for the full EDLC cell, two electrodes and the separator are combined giving exactly the same result as the initial value theorem method. The final instantaneous resistance is therefore defined as

$$R_{\text{i}} = \frac{2L}{A\,(\kappa + \sigma)} + R_{\text{sep}}. \tag{4.5}$$

4.3.3 Steady State Resistance

When an ideal capacitor is charged or discharged with a *constant current*, by definition, its voltage will increase or decrease in a linear fashion. If the slope of increase or decrease is known, and the current is known, the device capacitance is easily calculated. For non-ideal capacitors, there is an internal resistance that causes a potential offset from the ideal. If the difference between the ideal and real is taken during the middle of a step input, an estimate for the *steady-state* resistance can be made.

Additionally, by the the *final-value* theorem, evaluating Eq. (3.29) at zero or very low frequency gives the time domain expression for a non-changing input. The time domain evaluation is exactly the steady-state, or dc resistance, of the EDLC. The resulting *steady-state* resistance equation is then given as

$$
\begin{aligned}
R_{\text{steady}} &= \lim_{s \to 0} \left[\frac{2L}{A\,(\kappa + \sigma)} + \frac{L_{\text{sep}}}{A\kappa_{\text{sep}}} + \frac{4L\kappa\sigma + 2L\left(\kappa^2 + \sigma^2\right))\cosh(\Upsilon(s))}{A\Upsilon(s)\kappa\sigma(\kappa + \sigma)\sinh(\Upsilon(s))} \right] \\
R_{\text{steady}} &= \frac{2L\,(\kappa + \sigma)}{3A\kappa\sigma} + R_{\text{sep}}.
\end{aligned} \tag{4.6}
$$

One additional note is that R_{sep} cannot be directly measured but because it is a part of both the steady-state and instantaneous resistance values, it is temporarily assigned a value of

$$R_{\text{sep}} = \frac{R_{\text{i}}}{2}$$

Now, three resistance values have been defined in terms of only the eight internal parameters. Capacitance will follow next, but first, a short discussion concerning the internal resistance. One of the initial EDLC assumptions was that the electrolyte concentration is constant. While in general this is true, the concentration of ions, in time, can change near the edge of an impulse. When the EDLC has been at rest for a long time, charge carriers are uniformly distributed throughout the EDLC. But when current is first applied, carriers near the electrode boundaries quickly move can easily move away from the boundaries and after a very short time, the boundary regions are depleted of carriers and must obtain new ones from deeper within the electrode. After some arbitrary amount of time, a steady flow of carriers is formed.

4.3.4 Capacitance

To estimate the device capacitance, the charge or discharge slope during steady-state operation is measured. Then, assuming a constant dc current I is being applied, Eq. (1.3) can be used with the slope $\frac{dv}{dt}$ to determine the device capacitance. Equation (1.3) from Chap. 1 is

$$i(t) = C\frac{dv}{dt},$$

where the charging, steady-state slope is $\frac{dv}{dt}$ and when used with a dc current, the overall, or total device capacitance can be determined by

$$C_{\text{total}} = \frac{I_{\text{dc}}}{\text{slope}_{\text{ss}}}. \tag{4.7}$$

Because there are two double-layers, one for each electrode, they are effectively in series with regards to the entire EDLC. The capacitance for each electrode then is effectively doubled giving

$$C_{\text{electrode}} = \frac{2I_{\text{dc}}}{\text{slope}_{\text{ss}}}. \tag{4.8}$$

Using the *specific* capacitance C, the *specific* DL surface area a, and the volume of the electrode, $L \times A$, the electrode and total EDLC capacitance can be written using only four of the eight EDLC parameters from Table 4.1 as

$$C_{\text{electrode}} = aACL, \tag{4.9}$$

and

$$C_{\text{total}} = \frac{aACL}{2}. \tag{4.10}$$

These last two equations can be easily confused and care must be taken to ensure the correct capacitance is used. The ROM and FOM use $C_{\text{electrode}}$ while C_{total} is the actual measured value.

At this point, three measurable parameters, R_{ss}, R_{i}, and C_{total}, have been introduced as measurable quantities, and one parameter, R_{sep}, has been assigned a somewhat arbitrary value of one half R_{i}.

The next task is to re-derive the transfer equation in terms of *only* these four values and *none* of the parameters from Table 4.1.

4.3.5 Re-derivation of Transfer Functions using Circuit Elements

Re-writing Eq. (3.29) using only the variables R_{ss}, R_{i}, R_{sep}, and $C_{\text{electrode}}$, will make the transfer function look like it was obtained from a real circuit. The process begins with rearranging the $\Upsilon(s)$ term to use $C_{\text{electrode}}$

$$\Upsilon(s) = \sqrt{s\frac{L^2 aAC\,(\kappa+\sigma)}{\kappa\sigma}}$$

$$\Upsilon(s) = \sqrt{s\frac{L\,(aACL)\,(\kappa+\sigma)}{\kappa\sigma}}$$

$$\Upsilon(s) = \sqrt{s\frac{LC_{\text{electrode}}\,(\kappa+\sigma)}{\kappa\sigma}}.$$

Next, some simple algebra creates a term looking like Eq. (4.6)

$$\Upsilon(s) = \sqrt{sC_{\text{electrode}}\frac{3}{2}\left(\frac{2L\,(\kappa+\sigma)}{3\kappa\sigma} + R_{\text{sep}} - R_{\text{sep}}\right)},$$

which is now re-written as

$$\Upsilon(s) = \sqrt{sC_{\text{electrode}}\frac{3}{2}\,(R_{\text{ss}} - R_{\text{sep}})}.$$

Now substitute the rewritten $\Upsilon(s)$ into Eq. (3.29) and re-write

$$\frac{\overline{V_{\text{cell}}}}{\overline{I_{\text{cell}}}} = \frac{2L}{(\kappa+\sigma)} + \frac{L_{\text{sep}}}{\kappa_{\text{sep}}} + \frac{4L\kappa\sigma + 2L(\kappa^2 + \sigma^2)\cosh(\Upsilon(s))}{\Upsilon(s)\kappa\sigma(\kappa+\sigma)\sinh(\Upsilon(s))}.$$

Replacing the second term with R_{sep} and expanding the third term gives

$$\frac{\overline{V_{\text{cell}}}}{\overline{I_{\text{cell}}}} = \frac{2L}{(\kappa+\sigma)} + R_{\text{sep}} + \frac{4L\kappa\sigma + (2L\kappa^2 + 2L\sigma^2)\cosh(\Upsilon(s))}{\Upsilon(s)\kappa\sigma(\kappa+\sigma)\sinh(\Upsilon(s))}$$

$$\frac{\overline{V_{\text{cell}}}}{\overline{I_{\text{cell}}}} = \frac{2L}{(\kappa+\sigma)} + R_{\text{sep}} + \frac{4L}{\Upsilon(s)(\kappa+\sigma)\sinh(\Upsilon(s))} + \frac{(2L\kappa^2 + 2L\sigma^2)\cosh(\Upsilon(s))}{\Upsilon(s)\kappa\sigma(\kappa+\sigma)\sinh(\Upsilon(s))}.$$

Add and subtract R_{sep} terms, rearrange, and again expand

$$\frac{\overline{V_{\text{cell}}}}{\overline{I_{\text{cell}}}} = \frac{2L}{(\kappa+\sigma)} + R_{\text{sep}} - R_{\text{sep}} + \frac{2L}{(\kappa+\sigma)}\frac{2}{\Upsilon(s)\sinh(\Upsilon(s))}$$
$$+ \left(\frac{2L(\kappa^2 + 2\kappa\sigma - 2\kappa\sigma + \sigma^2)}{\kappa\sigma(\kappa+\sigma)}\right)\frac{\coth(\Upsilon(s))}{\Upsilon(s)} + R_{\text{sep}}.$$

Substitute R_{i} and continue to expand

$$\frac{\overline{V_{\text{cell}}}}{\overline{I_{\text{cell}}}} = (R_{\text{i}}) - R_{\text{sep}} + \left(\frac{2L}{(\kappa+\sigma)}\right)\frac{2}{\Upsilon(s)\sinh(\Upsilon(s))}$$
$$+ \left(\frac{2L((\kappa+\sigma)^2 - 2\kappa\sigma)}{\kappa\sigma(\kappa+\sigma)}\right)\frac{\coth(\Upsilon(s))}{\Upsilon(s)} + R_{\text{sep}},$$

and adding a few more R_{sep} terms gives

$$\frac{\overline{V_{\text{cell}}}}{\overline{I_{\text{cell}}}} = (R_{\text{i}} - R_{\text{sep}}) + \left(\frac{2L}{(\kappa+\sigma)} + R_{\text{sep}} - R_{\text{sep}}\right)\frac{2}{\Upsilon(s)\sinh(\Upsilon(s))}$$
$$+ \left(\frac{2L(\kappa+\sigma)^2 - 4L\kappa\sigma}{\kappa\sigma(\kappa+\sigma)}\right)\frac{\coth(\Upsilon(s))}{\Upsilon(s)} + R_{\text{sep}}$$

$$\frac{\overline{V_{\text{cell}}}}{\overline{I_{\text{cell}}}} = (R_{\text{i}} - R_{\text{sep}}) + (R_{\text{i}} - R_{\text{sep}})\frac{2}{\Upsilon(s)\sinh(\Upsilon(s))}$$
$$+ \left(\frac{2L(\kappa+\sigma)}{\kappa\sigma} - \frac{4L}{(\kappa+\sigma)}\right)\frac{\coth(\Upsilon(s))}{\Upsilon(s)} + R_{\text{sep}}.$$

Some final factoring, additional R_sep terms, and substitutions yields a transfer function parametrized with only R_ss, R_i, R_sep, and C_total.

$$\frac{\overline{V_\text{cell}}}{\overline{I_\text{cell}}} = (R_\text{i} - R_\text{sep})\left(1 + \frac{2}{\Upsilon(s)\sinh(\Upsilon(s))}\right)$$
$$+ \left(\frac{2L(\kappa+\sigma)}{\kappa\sigma} - 2\left(\frac{2L}{(\kappa+\sigma)} + R_\text{sep}\right) + 2R_\text{sep}\right)\frac{\coth(\Upsilon(s))}{\Upsilon(s)} + R_\text{sep} \qquad (4.11)$$

$$\frac{\overline{V_\text{cell}}}{\overline{I_\text{cell}}} = (R_\text{i} - R_\text{sep})\left(1 + \frac{2}{\Upsilon(s)\sinh(\Upsilon(s))}\right)$$
$$+ \left(3\left(\frac{2L(\kappa+\sigma)}{3\kappa\sigma} + \frac{R_\text{sep}}{3} - \frac{R_\text{sep}}{3}\right) - 2R_\text{i} + 2R_\text{sep}\right)\frac{\coth(\Upsilon(s))}{\Upsilon(s)} + R_\text{sep} \qquad (4.12)$$

$$\frac{\overline{V_\text{cell}}}{\overline{I_\text{cell}}} = (R_\text{i} - R_\text{sep})\left(1 + \frac{2}{\Upsilon(s)\sinh(\Upsilon(s))}\right) + (3(R_\text{ss} - R_\text{sep}) - 2R_0 + 2R_\text{sep})\frac{\coth(\Upsilon(s))}{\Upsilon(s)}$$
$$+ R_\text{sep} \qquad (4.13)$$

$$\frac{\overline{V_\text{cell}}}{\overline{I_\text{cell}}} = (R_\text{i} - R_\text{sep})\left(1 + \frac{2}{\Upsilon(s)\sinh(\Upsilon(s))}\right) + (3R_\text{ss} - 2R_\text{i} - R_\text{sep})\frac{\coth(\Upsilon(s))}{\Upsilon(s)} + R_\text{sep}. \quad (4.14)$$

While it may not be directly obvious, the transfer equation from Chap. 3, Eq.(3.29), and the measured value equation just derived, Eq. (4.14), can be shown to be mathematically equivalent by equating, substituting the parameter value equations for R_ss, R_i, R_sep, and $C_\text{electrode}$, and canceling or eliminating terms until the identity is obtained.

4.4 Circuit Element Measurement

With the full EDLC transfer function now written in terms of only four circuit-element parameters, values for these elements need to be obtained. There are three common methods that might be used. The first, as shown earlier for the Randles cell, can be done by applying a step input to the device and taking voltage measurements. Then as the dc current is known, Ohm's law, is sufficient to estimate the required data. Electrochemical Impedance Spectroscopy, (EIS), is a method of obtaining Bode plot data for a real device. EIS data can be used to refine the step response data and easily validate the accuracy of frequency-domain transfer functions. A third test, known as voltammetry, can be used to identify physical behaviors and is briefly described, but for now, is not required for data estimation. Voltammetry is an area in which further study may prove useful.

To illustrate the measurement process, the ROM obtained in Chap. 3 will be used to create a set of output data for a constant current pulse input. This data will form the *control* set. Measurements will be taken from the output as it were generated from a real EDLC and an M-ROM will be created. If the output of the M-ROM matches the output of the ROM, the process will be considered validated. The control ROM input and output will look similar to Fig. 3.1. The next several sections discuss the measurements and the development of the M-ROM.

4.4.1   Step Response

Applying a constant current pulse input results in a step response that can be used to directly determine the four needed parameters. A constant current pulse signal is applied to the EDLC ROM as shown in Fig. 3.1. The full cycle output and three zoomed version are shown in Fig. 4.3. Figure 4.3(b) is used to estimate the instantaneous resistance, Fig. 4.3(c) is used for the capacitance, and Fig. 4.3(d), for the steady-state resistance. The red plots in Fig. 4.3 were all generated using the truth or T-ROM, as generated in Chap. 3.

As indicated in the three plots, three circuit-element values R_{ss}, R_i, and C_{total}, are estimated and summarized as

$$R_{ss} = 25.5 \, \mu\Omega$$

$$R_i = 10.1 \, \mu\Omega$$

$$C_{total} = 12072 \, F,$$

and, as defined earlier, an arbitrary value of one half of R_i will be used for R_{sep} and is given by

$$R_{sep} = 5.5 \, \mu\Omega.$$

All *circuit-like* elements have now been identified and are used to create an M-ROM. The M-ROM output, when stimulated with a constant current input, is plotted against the T-ROM output as shown in Fig. 4.4. Clearly they are nearly identical although the RMS error shown in Fig. 4.4(a) is a bit deceiving as it is across both a charge and discharge cycle, and also includes rest time. The overall error, though, is quite small and can be nearly all
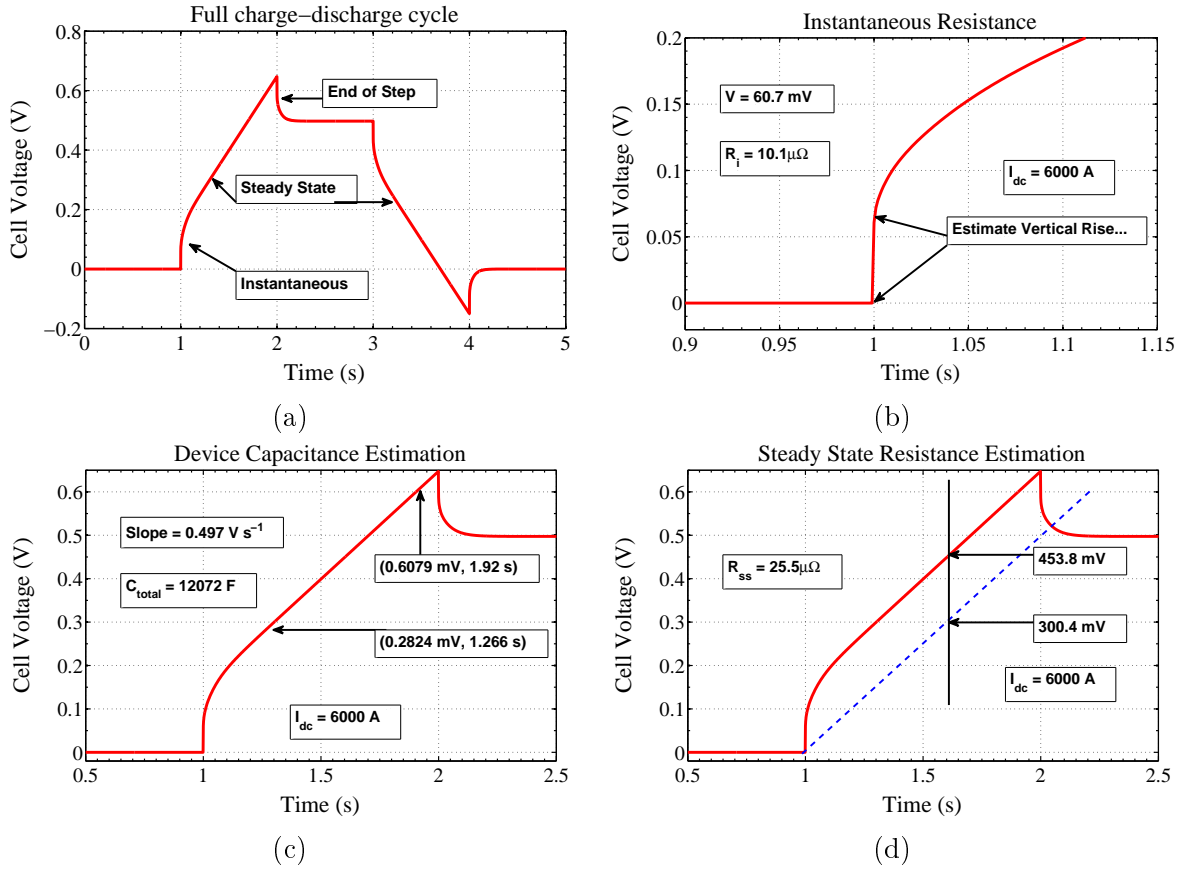
Figure 4.3:   EDLC pulse input response: (a) Full charge-discharge cycle (b) Zoom of the instantaneous voltage rise (c) Capacitance determination during steady-state (d) Zoom illustrating the steady-state resistance
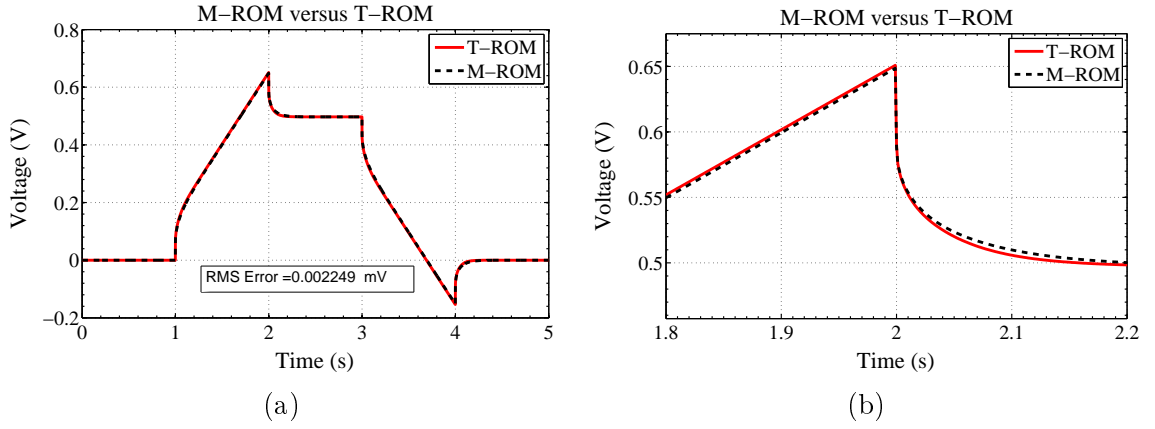
Figure 4.4: M-ROM versus T-ROM: (a) Full cycle (b) Zoom to max error region

attributed to measurement inaccuracies. Regardless of the error source, the results suggest that as long as the simulations are run in exactly the same manner, the outputs should match very well. A significant problem though, is evident if there is even a slight difference in timing from one ROM to the next. A 5 ms error out of 5 s does not seem significant but when calculating RMS error, timing errors are cumulative meaning that a shift in one signal, can suggest a large error, when in actuality, the error is very minor except for a small shift in time. The timing problem, however, provides a nice segue to the next section.

4.4.2 Electrochemical Impedance Spectroscopy

Electrochemical Impedance Spectroscopy is a non-destructive, small signal procedure similar to the small signal analysis used to characterize amplifier circuits. When applied to a real device, EIS measures the impedance over a wide range of frequencies and generates frequency, complex impedance, real impedance, and phase data. The data is typically used to create Bode[1] and Nyquist[2] plots.

A detailed description of EIS is outside the scope of this dissertation but very good application notes and tutorials can be found online, [55–59], in published literature [60,61],

---

[1]Bode plots generally consists of a phase vs frequency plot and an impedance magnitude vs frequency plot.

[2]Nyquist plots show the relation of real (X) impedance against (Y) imaginary impedance. These plots do not directly indicate frequency other than the left side is generally *higher* in frequency than the right side.
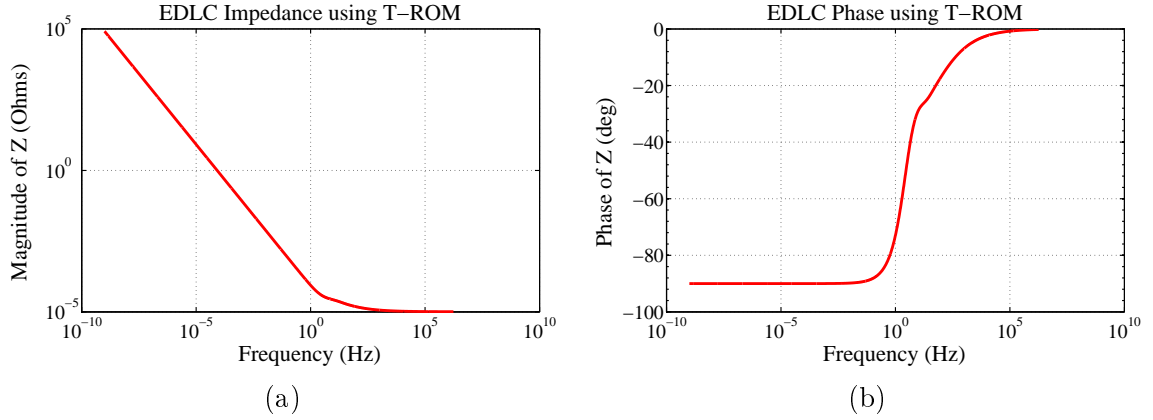
Figure 4.5: EIS for the T-ROM: (a) Impedance, (b) Phase

and in current textbooks [37,62]. EIS can be easily applied to circuit models using MATLAB or Spice to conduct frequency sweeps and analysis.

4.4.2.1 Obtaining EIS Data

EIS data consists of frequency, voltage, current, and phase information and additional information is easily be derived. EIS normally indicates a real device is being tested but the same results can obtained via simulation of test circuits or transfer functions by simply evaluating the circuit or transfer function over a range of frequencies. A nice example is the simulation and resulting Bode plot of the transfer equation Eq. (3.29) shown in Fig. 4.5. The parameters use are the same as used to create the T-ROM part of Fig. 4.4. The high frequency phase plot indicates the impedance is nearly all resistive at high frequencies while the integrator pole as noted in Chap. 3 is seen evident as the impedance grows exponentially as the frequency decreases towards dc.

A *bump* in the phase plot near 10 Hz is noted but at this time, no explanation is given.

EIS data for a simulation is easy to obtain and data for a real device can also be obtained. Real devices, however, require lengthy tests if low frequency behavior is desired. Testing at 1 mHz, requires nearly 17 minutes for a full test cycle. Decreasing the frequency to1 μHz , increases the cycle test time to about two weeks.

4.4.2.2 Utilizing EIS Data

EIS data has the advantage of not being time dependent. It simply gives phase and impedance information across a range of frequencies. Therefore, EIS data is ideal for the process of *optimization*. Starting with the four measured values, easily obtained from a time-domain plot, the M-ROM transfer function can be used to create a set of simulated EIS data. EIS data can be also obtained from the *control* system, or T-ROM transfer equation. The two sets of EIS data can then be compared and the four measured values manipulated to obtain a best match. The same process can be used with EIS and measured data from a real EDLC.

4.4.2.3 Individual Parameter Extraction

Direct observation of the Bode plot in Fig. 4.5 indicates a high frequency impedance of about $10^{-5}\,\Omega$ which is almost exactly the same as the measured value for the instantaneous resistance R_i. The steady-state resistance is not so easily obtained as there is an integrator pole as indicated by the exponentially increasing impedance magnitude as the frequency decreases.

Actual parametric data however, is not so easily extracted, but by using total values and the optimized data, accurate estimates can be made of grouped parameters. Details on this process are given in Sect. 4.5.4.

4.4.3 Voltammetry

Voltammetry is a process often lumped together with EIS descriptions and theory, but its not really the same. Whereas EIS uses small signal analysis across a wide range of frequencies, voltammetry uses a slowly changing voltage at only one frequency, ramping the EDLC back and forth across its advertised voltage range. The *scan-rate* measures of how fast the voltage changes. As the voltage changes, the resulting current is measured and a current versus voltage plot looking like Fig. 4.6 is created. Based on the plot, internal parametric information might be obtained.

Voltammetry is presented here as an additional method that might be used to obtain parametric data but at this point in time, little information is obtained. Like EIS, the best

data is obtained when electrical access to internal components is available. For now, the voltammetry concept is presented along with a short illustration of how the capacitance of a measured device can be obtained.

A word of caution: because EDLCs have a very low internal resistance, applying a fast scan rate, or large voltage differential, to the EDLC terminals can result in a *lot* of current being absorbed or released and potentially can cause equipment damage. The risk of human injury is minimal though, due to the low EDLC voltage. There is however, a risk of fire as high currents can generate significant heat very quickly.

4.4.3.1   Estimating Capacitance

For an ideal capacitor, when the applied voltage changes at a constant rate over time, its time derivative is a constant. Assuming the capacitance is a constant, the current must then also be constant. By slightly re-arranging Eq. (1.3), the capacitance C is easily solved for

$$C = I\frac{\mathrm{d}t}{\mathrm{d}V}. \tag{4.15}$$

An example is performed using the Randles cell from Fig. 4.1(a), with $C = 150\,\mathrm{F}$, $R_\mathrm{s} = .001\,\Omega$, and $R_\mathrm{p} = 100\,\mathrm{k}\Omega$. Several scan rates are used to generate the four plots shown in Fig. 4.6. In Fig. 4.6(a), a fast scan rate is used to demonstrate the high currents required when the applied voltage changes quickly. Figures 4.6(b), and (c), show a slower scan-rate and much more manageable currents of 150 A, and 15 A[3]. Figure 4.6(d), with its very slow scan-rate, shows what looks like a thick line of current which can be attributed, at such a slow scan-rate, to a typical capacitor charge curve. If left at a single voltage, the amount of charging current eventually decays to zero as the device is charged and it's the decaying current that is observed. The higher scan-rates test simply do not provide enough time to observe significant current decay. There is a relation between the rate of current decay and the internal resistance but at this time, it is not investigated further.

---

[3]High currents can easily be obtained at the low EDLC voltages as power dissipation will be minimal. Cell test equipment such as an Arbin BT-2000 can easily handle currents exceeding 300 A.
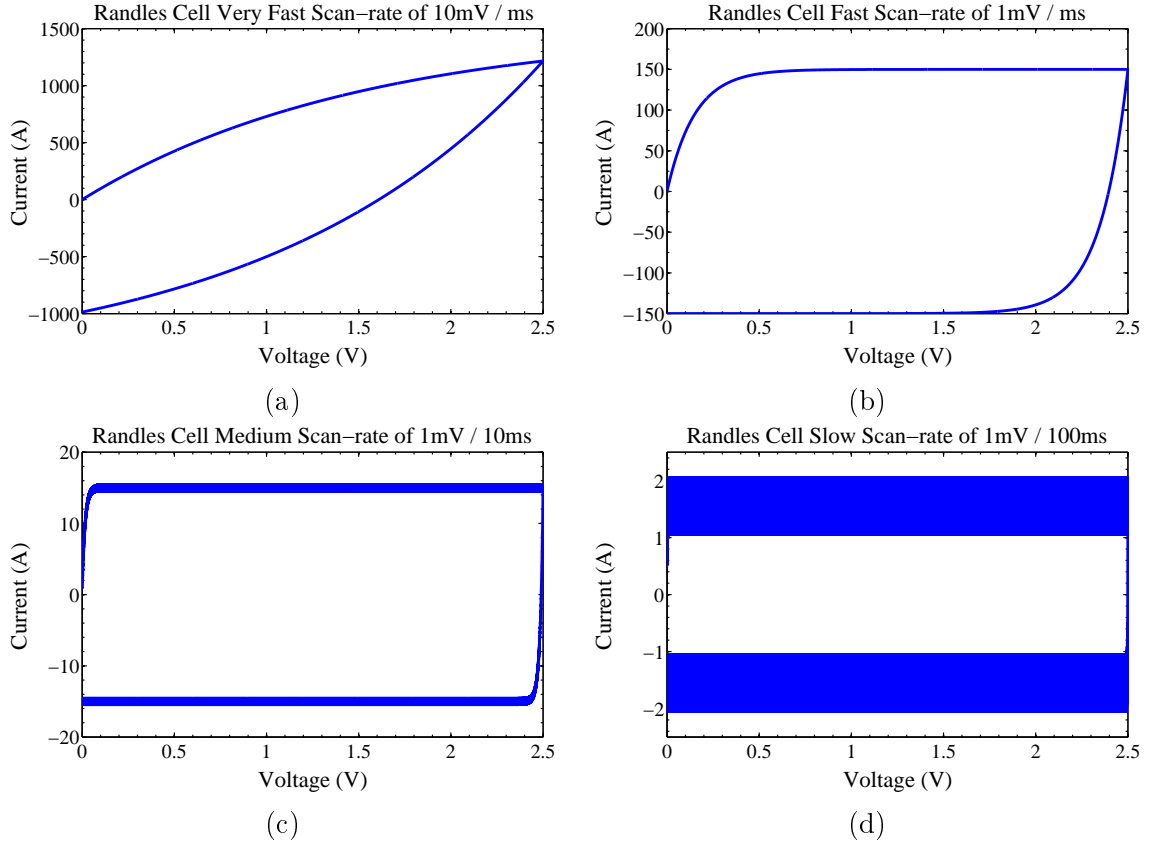
Figure 4.6: Voltammetry illustration: (a) Scan-rate $10\,\mathrm{mV\,ms^{-1}}$ (b) Scan-rate $1\,\mathrm{mV\,ms^{-1}}$ (c) Scan-rate $1\,\mathrm{mV\,10\,ms^{-1}}$ (d) Scan-rate $1\,\mathrm{mV\,100\,ms^{-1}}$

Figure 4.6(c) shows an average current of $15\,\mathrm{A}$ and with a scan-rate of $1\,\mathrm{mV\,10\,ms^{-1}}$. The capacitance is

$$C = I\frac{\mathrm{d}t}{\mathrm{d}V} = (15\mathrm{A})\frac{0.01}{0.001}\frac{\mathrm{s}}{\mathrm{V}} = 150\,\mathrm{F}$$

which is exactly the value used to create the plot. The simple Randles cell obviously provides a voltammetry plot in rectangular form but it does not model non-idealities such as diffusion, electrolyte concentration, or faradaic current. With a real EDLC or even with a more realistic model, observing how the shape of the plot changes is as it is cycled through its voltage range is worthy of additional study and is presented as an area of future work in Chap. 7.
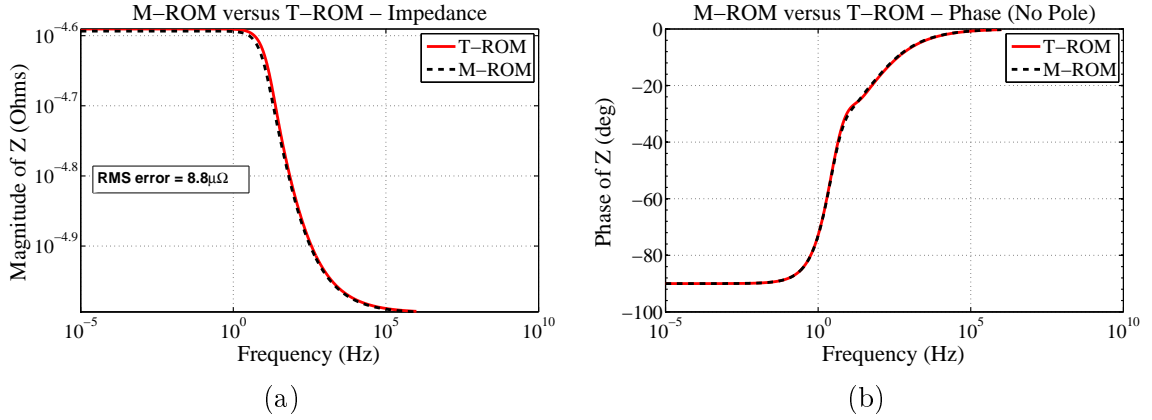
Figure 4.7: EIS comparison of T-ROM versus M-ROM: (a) Impedance (b) Phase

4.5 Parameter Extraction and Optimization

Four circuit-like variables, R_{ss}, R_i, and C_{total}, have now been obtained by physical measurement and one more, R_{sep} has been estimated by using half of R_i. When the four variables are used to create an M-ROM, its output is nearly the same as the T-ROM output, as shown in the Bode plot of Fig. 4.4. Because the equation forms of R_{ss}, R_i, and C_{total} are mathematically equivalent to the T-ROM variables, the RMS error between their two outputs can be attributed to primarily errors in measurement. In this test case, there is no *noise* or other non-accounted for behaviors and both the impedance and phase plots match quite almost identically with an RMS impedance error of only $8\,\mu\Omega$. As will be seen, the optimized impedance error will be about 1000 times smaller.

To obtain an even better set of measured values, the measured data is compared to the known *control* data which, in the real world, is EIS data taken from a real EDLC but here, the control data is simply the T-ROM output. By using a non-linear minimization algorithm, the four measured circuit-element values can be changed slightly to give near perfect results. An iterative approach compares the least squares difference between the simulated EIS data and the measured EIS data and slightly modifies the measured data values before repeating the comparison. If the comparison indicates less error, the current parameter values are saved, and the process then continues eventually converging to a minimal error solution. The algorithm for parameter manipulation is the Levenberg-Marquardt Algorithm (LMA) [63]

and although the algorithm itself is not the focus of this dissertation, it is quite interesting,
The general optimization process is described next.

4.5.1 Optimization Process

The optimization process begins with the set of parameters: R_{ss}, R_{i}, R_{sep}, and C_{total}. These
parameters, as measured and whether accurate or inaccurate, form the *starting* point of the
optimization process. The objective function, or the function to be minimized, is the RMS
difference between the two EIS data sets taken from: (1) the transfer function developed for
the M-ROM, and (2) the transfer function developed for the T-ROM. Both equations are
shown here and referred to as *measured* and *true*.

$$Meaured = (R_{\text{i}} - R_{\text{sep}})\left(1 + \frac{2}{\Upsilon(\text{s})\sinh(\Upsilon(s))}\right) + (3R_{\text{ss}} - 2R_{\text{i}} - R_{\text{sep}})\frac{\coth(\Upsilon(s))}{\Upsilon(s)} \quad (4.16)$$

$$+ R_{\text{sep}} - \frac{2}{sC_{\text{tot}}}, \quad (4.17)$$

$$True = \frac{2L}{A(\kappa + \sigma)} + \frac{L_{\text{sep}}}{A\kappa_{\text{sep}}} + \frac{4L\kappa\sigma + 2L(\kappa^2 + \sigma^2)\cosh(\Upsilon(s))}{A\Upsilon(s)\kappa\sigma(\kappa + \sigma)\sinh(\Upsilon(s))} - \frac{2}{sCaL}. \quad (4.18)$$

The residue, as shown, has been removed from both functions.

$$True\,Res_0 = \lim_{s \to 0} sH(s) = \frac{2}{CaAL}$$

$$Measured\,Res_0 = \frac{2}{C_{\text{tot}}}.$$

EIS is performed on both equations and impedance magnitude data generated for both. The
data is differenced, and the RMS calculated. The LMA, then modifies, R_{ss}, R_{i}, R_{sep}, and
C_{total}, and a new RMS error is calculated. If the new error is smaller than the previous,
the values for the parameters are saved as the new best set. The process is repeated until a
minimal RMS is achieved or a maximum number of attempts have been made. The process is
sensitive to the *initial starting parameters* and there is no guarantee of minimal convergence.
When finished, the LMA will return the best matching parameter set of R_{ss}, R_{i}, R_{sep}, and
C_{total}, that it could find.

4.5.2 Optimization Results

Table 4.2 contains three versions of five values: R_{ss}, R_{i}, R_{sep}, $C_{\text{Electrode}}$, and C_{total}. The
calculated column is obtained by direct substitution of the true internal parameters into the

TABLE 4.2: Circuit element summary of optimization

Parameter	Equation	Calculated	Measured	Optimized
R_{ss}	$\frac{2L(\kappa+\sigma)}{3A\kappa\sigma} + R_{\text{sep}}$	$25.679\,\mu\Omega$	$25.5\,\mu\Omega$	$25.679\,\mu\Omega$
R_{i}	$\frac{2L}{A(\kappa+\sigma)} + R_{\text{sep}}$	$10.117\,\mu\Omega$	$10.1\,\mu\Omega$	$10.117\,\mu\Omega$
R_{sep}	$\frac{L_{\text{sep}}}{A\kappa_{\text{sep}}}$	$10.000\,\mu\Omega$	$5.5\,\mu\Omega$	$10.000\,\mu\Omega$
C_{total}	$C_{\text{total}} = aACL,$	$12062.5\,\text{F}$	$12072\,\text{F}$	$12062.5\,\text{F}$
$C_{\text{Electrode}}$	$C_{\text{total}} = 2aACL,$	$24125\,\text{F}$	$24144\,\text{F}$	$24125\,\text{F}$

five equations as derived in Sect. 4.3. The *measured* column is simply the measurement circuit element values. The *optimized* column shows the measured parameters as modified by the optimization process. The optimized values match identically with the calculated values. Because the measured values are somewhat subject to human measurement, several slightly different sets of *measured values* were tested and in all cases, the optimization process returned identical values. The results of the optimization can be seen in Fig. 4.8 and Fig. 4.9 comparing optimized and unoptimized parameter sets.

4.5.3 M-ROM Validation

Using the optimized parameter values from Table 4.2, the EIS, or Bode plots, of the measured and true transfer equations have been shown to match. The next step is to match the output of the M-ROM, using the optimized parameters, to the output of the T-ROM using truth data. Before executing the Chap. 3 DRA process however, there are some minor edits that should be noted.

First, in step one of the DRA, the first term of the estimated discrete-time impulse response $h[1]$, or $h*[1]$, is set to the steady-state resistance by

$$h*[1] = \lim_{s \to 0} H*(s) = \frac{2L(\kappa + \sigma)}{3A\kappa\sigma} + R_{\text{sep}}$$

$$h*[1] = R_{\text{ss}}.$$
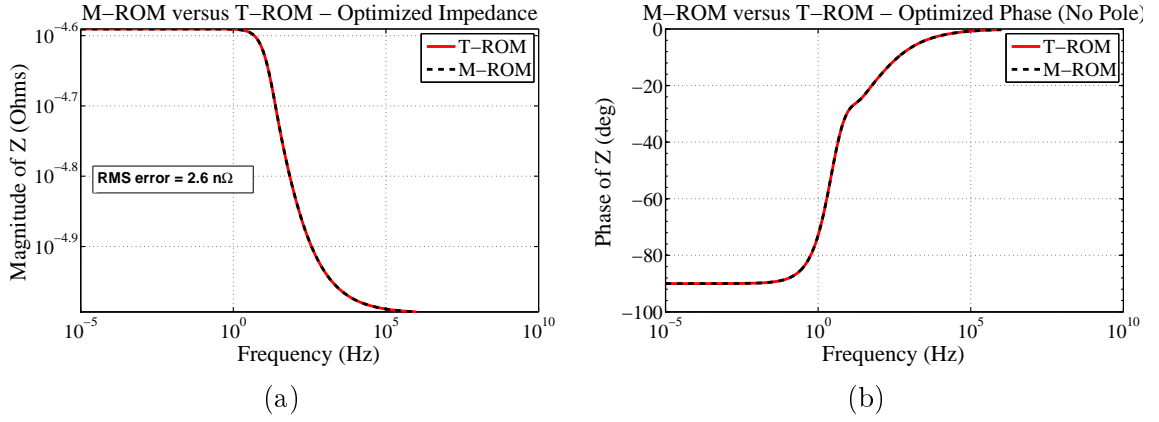
Figure 4.8:   M-ROM versus T-ROM impedance : (a) Non-optimized (b) Optimized
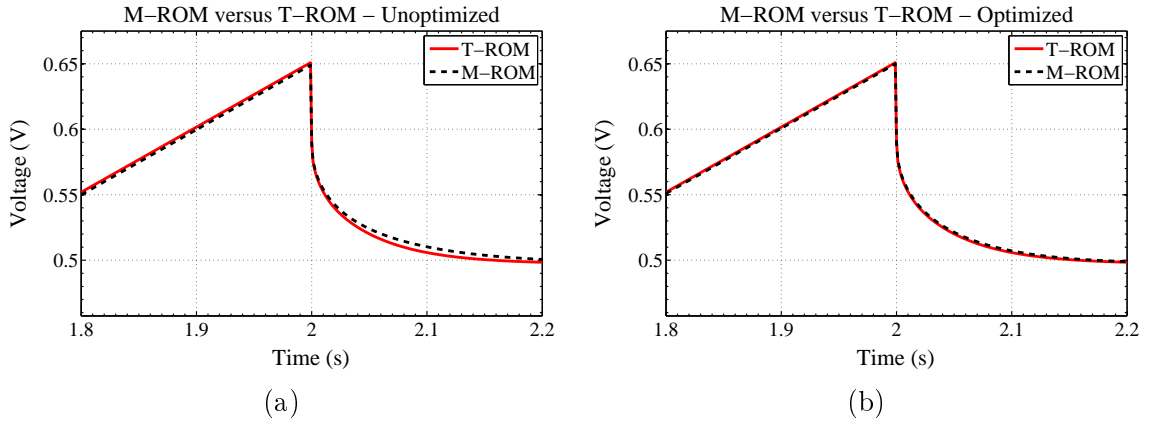
Figure 4.9:   M-ROM versus T-ROM region of error: (a) Non-optimized (b) Optimized

Second, in step four, the feed-through, or $\widehat{D}$ term, in the state-space, is recognized as, and set to, the instantaneous resistance given by

$$\widehat{D} = \frac{2L}{A\left(\kappa + \sigma\right)} + R_{\text{sep}}$$

$$\widehat{D} = R_{\text{i}}.$$

Third, the residue defined in measured terms, $res_0 = \frac{2}{C_{\text{total}}}$, is added back to augment the C matrix. As there are no other special considerations for the DRA, the T-ROM and M-ROM can now both be implemented and their outputs compared in both time and frequency domains as shown in Figs. 4.8, and 4.9(b). The RMS error is now only few nΩ!

4.5.4   Internal Conductivity Values

Without a way to fill Table 4.1 with real EDLC data, simulations that dig deeper into internal behaviors and states cannot be performed. None of the values though, can be directly measured with just voltage and currents but it *is possible*, to obtain at least a representation of the three conductivity parameters if considered across the entire EDLC. As used in Table 4.1, they are *specific* values having units of $\mathrm{S\,m^{-1}}$ and without internal dimensional details, actual values cannot be determined.

Therefore three pseudo-new variables called *total-value* variables are introduced. These pseudo-new variables, κ_{total}, σ_{total}, and κ_{s-tot}, can all be defined using the internal parameters L, A, a, σ, κ, and κ_{sep}. Then Eqs. (4.5), (4.6), (4.8), and (4.3), can be applied to obtain expressions, and numeric values for each of κ_{total}, σ_{total}, and κ_{s-tot}.

To motivate the idea, consider that any given material will have some amount of *total-resistance*, $R = \frac{L}{A}\rho$ where L, A, and ρ, are the material length, cross sectional area, *and* specific resistivity [37]. As the reciprocal of *total-resistance*, the *general* equation for *total-conductivity* is defined by

$$\sigma_{\mathrm{tot}} = \frac{A}{L}\sigma_{specific},\tag{4.19}$$

where the units of σ_{tot} are siemens and those of $\sigma_{\mathrm{specific}}$ are $\mathrm{s\,m^{-1}}$.

Equation (4.19) is then applied to the three specific conductivities used in Table 4.1 to give

$$\kappa_{\mathrm{total}} = \frac{A}{L}\kappa,$$
$$\sigma_{\mathrm{total}} = \frac{A}{L}\sigma$$
$$\kappa_{\mathrm{s\text{-}total}} = \frac{A}{L_{\mathrm{sep}}}\kappa_{\mathrm{sep}} = \frac{1}{R_{\mathrm{sep}}}.$$

The separator is assumed to have the same cross sectional area as the electrode, and as its resistance has already been identified, the *total conductivity* for the separator is easily determined. The conductivities in the solid and solution part of the electrode remain to be determined.

Starting with Eqs. (4.6) and (4.4), minus the separator, the total-conductivities in the electrodes are substituted giving

$$R_{\text{steady}} = \frac{2L\left(\kappa + \sigma\right)}{3A\kappa\sigma} = \frac{2LA\kappa + 2AL\sigma}{3A^2\kappa\sigma} = \frac{2\frac{A}{L}\kappa + 2\frac{A}{L}\sigma}{3\frac{A}{L}\kappa\frac{A}{L}\sigma} = \frac{2\kappa_{\text{total}} + 2\sigma_{\text{total}}}{3\kappa_{\text{total}}\sigma_{\text{total}}}$$

$$R_{\text{instant}} = \frac{2L}{A\left(\kappa + \sigma\right)} = \frac{2}{\frac{A}{L}\left(\kappa + \sigma\right)} = \frac{2}{\kappa_{\text{total}} + \sigma_{\text{total}}}.$$

R_{sep} is then added to arrive at

$$R_{\text{i}} = \frac{2}{\kappa_{\text{total}} + \sigma_{\text{total}}} + R_{\text{sep}}$$

$$R_{\text{ss}} = \frac{2}{3}\frac{\kappa_{\text{total}} + \sigma_{\text{total}}}{\kappa_{\text{total}}\sigma_{\text{total}}} + R_{\text{sep}}.$$

Since the optimized values for R_{sep} , R_{i} , and R_{ss}, are known, there are now two equations with only two unknowns, κ_{total} and σ_{total}, that can easily be determined. Additional rearranging gives

$$\frac{R_{\text{i}} - R_{\text{sep}}}{2} = \frac{1}{\kappa_{\text{total}} + \sigma_{\text{total}}}$$

$$\frac{3\left(R_{\text{ss}} - R_{\text{sep}}\right)}{2} = \frac{\kappa_{\text{total}} + \sigma_{\text{total}}}{\kappa_{\text{total}}\sigma_{\text{total}}},$$

and just a bit more algebra results in two quadratics for κ_{total} and σ_{total}

$$\sigma_{\text{total}}^2 + \left(\frac{2}{R_{\text{sep}} - R_{\text{i}}}\right)\sigma_{\text{total}} + \left(\frac{4}{3\left(R_{\text{i}} - R_{\text{sep}}\right)\left(R_{\text{ss}} - R_{\text{sep}}\right)}\right) = 0$$

$$\kappa_{\text{total}}^2 + \left(\frac{2}{R_{\text{sep}} - R_{\text{i}}}\right)\kappa_{\text{total}} + \left(\frac{4}{3\left(R_{\text{i}} - R_{\text{sep}}\right)\left(R_{\text{ss}} - R_{\text{sep}}\right)}\right) = 0.$$

R_{i}, R_{sep}, and R_{ss}, are now just coefficients in two quadratic equations and as the equations are identical, only one quadratic equation needs to be solved with its roots being the two conductivities. Setting

$$a = 1$$

$$b = \frac{2}{R_{\text{sep}} - R_{\text{i}}}$$

$$c = \frac{4}{3\left(R_{\text{i}} - R_{\text{sep}}\right)\left(R_{\text{ss}} - R_{\text{sep}}\right)},$$

Parameter	Equation	True Value (From Equation)	Non-optimized (R_{ss}, R_{i}, R_{sep})	Optimized (R_{ss}, R_{i}, R_{sep})
κ_{total}	$\frac{A}{L}\kappa$	$42\,626\,\mathrm{S}$	$30\,8023\,\mathrm{S}$	43000
σ_{total}	$\frac{A}{L}\sigma$	$1.705\times10^{7}\,\mathrm{S}$	complex result	$1.705\times10^{7}\,\mathrm{S}$
$\kappa_{\mathrm{s\text{-}tot}}$	$\frac{1}{R_{\mathrm{sep}}}$	$100\,000\,\mathrm{S}$	complex result	$100\,000\,\mathrm{S}$

TABLE 4.3:   Total conductivity within the EDLC ROM

then the roots are found by

$$\sigma_{\mathrm{total}} \text{ and } \kappa_{\mathrm{total}} = \frac{-b \pm \sqrt{b^2 - 4ac}}{2a} \text{and} = \frac{-\frac{2}{R_{\mathrm{sep}} - R_{\mathrm{i}}} \pm \sqrt{\left(\frac{2}{R_{\mathrm{sep}} - R_{\mathrm{i}}}\right)^2 - 4\frac{4}{3(R_{\mathrm{i}} - R_{\mathrm{sep}})(R_{\mathrm{ss}} - R_{\mathrm{sep}})}}}{2},$$

(4.20)

Reference sources generally agree the conductivity of solid activated carbon is considerably higher than that of the electrolyte. Therefore, σ_{total} is set to the larger result and κ_{total} to the smaller. If the roots come back as being complex, there is an error as both conductivities must be positive numbers. Complex numbers should not occur with the optimized parameter values but could easily occur with the non-optimized values.

Table 4.3 can now be populated by referencing conductivity data from Table 4.1. The *true value* column is obtained by evaluating the appropriate equation and setting the cross sectional area A to 1. The *non-optimized* column is obtained by applying the appropriate unoptimized data to the corresponding equation. Two results came back as complex. Finally, the *optimized* column uses the optimized values of R_{ss}, R_{i}, and R_{sep} to evaluate Eq. (4.20) and the results are nearly exactly the same as the *true* value column.

Finally, it should be noted that all transfer functions developed in Chap. 3, can be expressed and evaluated using the three total value conductivities although that process is not performed here.

4.6 Summary

The primary goal of this chapter was to develop a simple, non-destructive process to easily identify a set of EDLC parameters suitable for executing a ROM. The process converts the internal-parameter based transfer function to a circuit-element based form that can be evaluated from a step response. Current and voltage measurements were shown to easily provide sufficiently accurate values for the circuit-element based transfer function. The process was first applied to a simple Randles cell, then was extended to the complex EDLC physics-based model. The M-ROM output and T-ROM output validated well, but after the M-ROM parameters were optimized, validated almost perfectly.

EIS was used in the parameter identification process and was shown to be quite useful in the optimization portion. Voltammetry was also introduced as a potential source of internal parametric information, but was not used beyond its introduction. An optimization process was carried out to obtain best fit circuit-element parameters and from these, total-value parameters were obtained for the internal conductivities. The outputs of the M-ROM and T-ROM indicate the circuit-element approach to obtaining internal parameters is solid.

The *total-value* parameter set is good to have but it does not give the actual *specific*-conductivity values, or other values such as the interfacial double layer surface area. Determining these additional, *specific* parameters, will require internal dimensional information which is the focus of the first part of Chap. 5 where an EDLC will be opened and dimensional information obtained.

CHAPTER 5

Application to Commercial EDLCs

5.1 Introduction

Chapters 3 and 4 derived and simulated EDLCs using only *truth or control* data for the T-ROM, and only measured and optimized data for the M-ROM. It was shown that circuit-element data can be collected using only simple current and voltage measurements and when optimized, gives almost identical results to the truth data. Numeric values for the total device capacitance, conductivity in the solid, the electrolyte, and in separator were also obtained. For many applications and simulations, the M-ROM, with no additional modifications would likely be sufficient. If however, a designer needed to have an understanding of the internal component behavior under various conditions, or the internal state of the EDLC at any particular location or time, additional information is required. The primary goal of this chapter is to extend the results from Chap. 4 and to completely identify as many, if not all, the parameters listed in Table 4.1.

To accomplish the complete parameter identification, Chap. 5 is split into the following three major sections:

Deconstruction: A "Maxwell 150 F Boostcap EDLC", (BCAP), is deconstructed and individual component measurements are taken to estimate physical dimensions such as electrode length, width, height, quantities of carbon used in each electrode, and how much electrolyte is present. The measured data, along with data taken from various handbooks, literature, and online references, is then used to estimate non-measurable parameters such as the specific interfacial surface area a.

BCAP Measurement: The simple voltage and current measurements as described in Chap. 4 are performed on the BCAP and a new M-ROM data set is developed and the

output compared with the actual BCAP responses. Parameter optimization is considered and as many parameters as possible are obtained. The dimensional information obtained from the deconstruction is utilized to obtain *specific* parameter values for all Table 4.1 entries.

Parameter Extraction and Optimization: Data from all sources are compiled, compared, and the overall process discussed.

5.2 Deconstruction of a Maxwell 150 F EDLC

Tearing an actual device apart and analyzing its internal components is one method of identifying physical properties such as weights and dimensions. These dimensions and weights will lead to volumes and estimations of how much of a particular material is present. With materials knowledge and properties obtained from data-tables or other sources, estimates are made about the double layer interfacial surface area and capacitance. The term *estimate* is used because there is a level of uncertainty even though all measurements are repeated several times to be as accurate as possible.

Equipment used to measure device parameters was limited to a ruler for large dimensions, electronic calipers for thickness, and standard laboratory scales for weights. Additional laboratory techniques and equipment such as X-ray diffraction (XRD) and a scanning electron microscope (SEM), could be used to more-accurately determine electrode composition, surface area, and the actual micro-pore structure. Those techniques and processes, while potentially useful, are outside the scope of this dissertation.

5.2.1 EDLC Components

The BCAP is a sealed, aluminum container enclosing two identical electrodes, a separator, and an electrolyte. The basic construction process is to first fabricate the electrodes, then create a roll with each electrode separated by the separator paper. Figure 5.1 illustrates the construction.

There are other packaging materials present such as the plastic end cap and the aluminum casing but these are discarded after weighing. The constituent materials of a BCAP
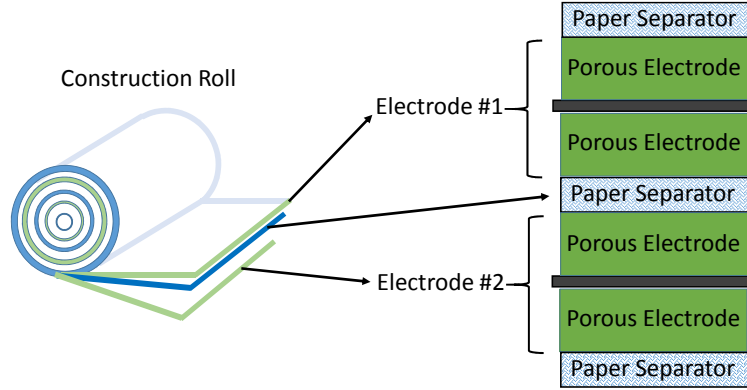
Figure 5.1: EDLC construction schematic

EDLC are estimated or assumed based on several documents [13, 25, 64] and summarized here:

- Electrodes - Assumed to be activated carbon with unknown binders and other additives. They have an approximate weight of 5.8 g per electrode including any residual salts, binders, and additives. The electrodes are double sided meaning the etched aluminum current collector has activated carbon on both sides. This does not affect the model performance or conceptual schematics from Chap. 2..

- Electrolyte salt or solute - Tetraethylammonium tetrafluoroborate. Cannot distinguish from carbon electrode without additional testing.

- Electrolyte solvent - Acetonitrile. Approximately 5.56 g measured by the difference between unopened EDLC and opened EDLC allowed to dry,

- Current collectors - Etched aluminum foil - Approximately 1.7 g per electrode not including the external leads or welded contact strips.

- Separator - Thin paper membrane weighing about 0.42 g.

TABLE 5.1: Maxwell Boostcap 150 F - construction data

Component	Variable	Value	Units
Un-opened device	-	29.22	g
After overnight drying	-	23.66	g
Packaging materials	-	7.56	g
Paper separator	-	0.42	g
Welded aluminum strips (each)	-	0.17	g
Total electrode weight (no strips)	-	15	g
Individual electrode weight	-	7.5	g
Separator width	w_s	4.5	cm
Separator height	h_e	66	cm
Separator thickness	L_{sep}	0.005	cm
Electrode width	w_e	4	cm
Electrode height	h_e	62	cm
Electrode thickness (double sided)	l_e	0.026	cm

5.2.2 Deconstruction Process

To obtain measurements safely, the BCAP was first allowed to completely discharge by shorting its terminals overnight. After an initial unopened weighing, the EDLC was disassembled, the components laid out, and allowed to dry overnight in a well ventilated location. The dried weight was recorded thus giving the weight of the solvent. Inactive components such as the casing, plastic end caps, and aluminum leads were also weighed before being discarded. The remaining parts consisted of only the two electrodes and separator. Measurements of these were taken giving weight, width, thickness, and height of each. The measured data is summarized in Table 5.1.

Also included are several pictures showing the deconstruction process and parts.

5.2.3 Electrode Length and Cross Section

The T-ROM from Chap. 3, requires both the length of the separator, L_{sep}, and the electrode, L. The total conductivity estimates described in Chap. 4 require the cross sectional area A and length L of the electrode. Deconstruction yields all required dimensions for the separator and electrodes. Widths and heights are easily measured with a ruler while the length, or thickness, is obtained by folding the material several times before measuring

<center>(a)</center>

<center>(b)</center>

Figure 5.2: BCAP: (a) Unopened BCAP (b) Opened with coils visible
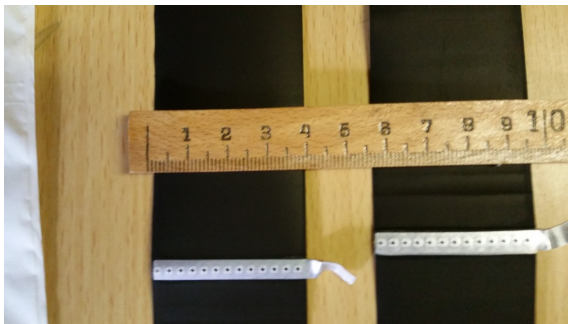
<center>(a)</center>
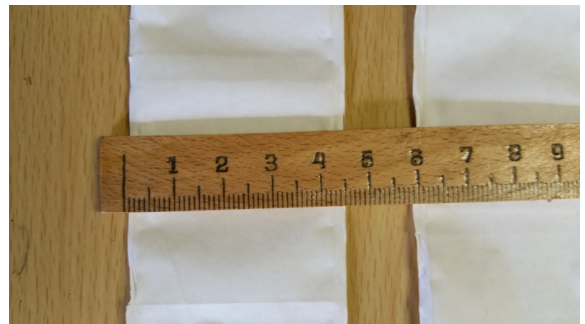
<center>(b)</center>

Figure 5.3: BCAP: (a) Electrodes and welded strips (b) Separator
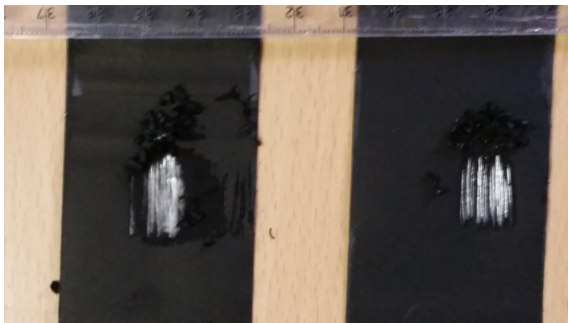
<center>(a)</center>
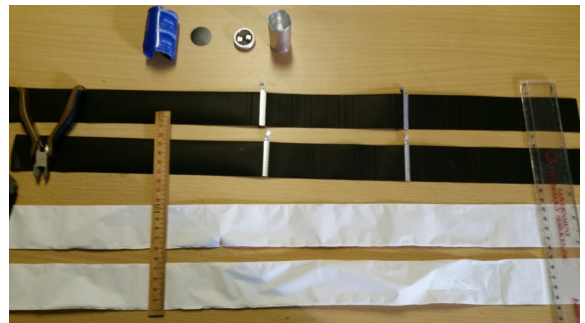
<center>(b)</center>

Figure 5.4: BCAP: (a) Aluminum current collector (b) Everything

with an electronic micrometer. The thickness is then divided by the number of folds. The electrode itself is slightly more complex as the aluminum foil current collector is coated with activated carbon material on *both* sides. Using an *assumed* aluminum foil thickness of $1 \, \text{mil} = 0.0254 \, \text{mm}$, and dividing by two gives the estimated length of

$$L = \frac{l_{\text{e}} - 0.0254 mm}{2} = \frac{(0.26 \, \text{mm} - 0.0254 \, \text{mm})}{2} = 0.01173 \, \text{cm}.$$

The cross sectional area of the separator and electrodes is then estimated, from data in Table 5.1 as

$$A_{\text{electrode}} = h_{\text{e}} \times w_{\text{e}} = 62 \, \text{cm} \times 4 \, \text{cm} = 248 \, \text{cm}^2$$

$$A_{\text{separator}} = h_{\text{s}} \times w_{\text{s}} = 66 \, \text{cm} \times 4.5 \, \text{cm} = 297 \, \text{cm}^2.$$

While the separator has a slightly larger surface area than the electrode, the electrode surface area will be used for both because any ions that cross the separator must come from the electrodes therefore all references to the cross sectional area will be $A = A_{\text{electrode}}$. The total electrode volume is also calculated as

$$Vol_{\text{electrode}} = (A_{\text{electrode}}) (l_{\text{e}}) = \left(248 \, \text{cm}^2\right) (0.026 \, \text{cm}) = 6.448 \, \text{cm}^3$$

5.2.4 Interfacial Double Layer Surface Area

Because it is microscopic and porous in nature, the interfacial surface area a of the DL cannot be directly measured with the simple methods used previously. To experimentally obtain an exact or nearly exact value would require additional methods and/or equipment as mentioned at the beginning of this section and is outside the scope of this dissertation. There is however, another way to obtain an educated estimate for the interfacial surface area by using material property values from data-sheets, handbooks, and online references [17,19,53,54,65]. These sources give the surface area of activated carbon per gram to be anywhere from $250 \, \text{m}^2 \, \text{g}^{-1}$ to $3000 \, \text{m}^2 \, \text{g}^{-1}$ depending on manufacturing methods, source of the activated carbon, and additional additives or binding agents.

Estimating the amount of carbon present, by weight, is accomplished by first removing the welded aluminum contact tabs from the electrodes leaving only the double sided carbon

coated aluminum foil current collectors, along with any[1]residual salts, additives, or other agents, left behind after the acetonitrile solvent has evaporated. Knowing aluminum has a standard weight of $2700 \, \text{kg} \, \text{m}^{-3}$ [66], and again *assuming* a $1 \, \text{mil} = 0.0254 \, \text{mm}$ foil thickness, the volume of aluminum can be estimated and its total weight calculated, per electrode, as

$$Aluminum \Rightarrow \left(2700 \frac{\text{kg}}{\text{m}^3}\right) \left(\frac{\text{m}^3}{1\,000\,000\,\text{cm}^3}\right) (248 \, \text{cm}^2) (0.00254 \, \text{cm}) = 1.7 \, \text{g}_{\text{alum}}.$$

Subtracting the aluminum weight from the measured electrode weight gives the weight of the carbon as

$$Activated\,Carbon = 7.5 \, \text{g} - 1.7 \, \text{g} = 5.8 \, \text{g}_{\text{carbon}}.$$

Again, note that additives such as binders, dried electrolyte salts, etc., are all included in the carbon weight as they cannot be easily disassociated from the electrode without a process such as XRD.

As mentioned previously, various sources list the specific surface area of activated carbon to range anywhere from $250 \, \text{m}^2 \text{g}^{-1}$ to $3000 \, \text{m}^2 \text{g}^{-1}$ which is a *huge* range and the resulting propagation error is potentially large. A partial solution is found by referencing a Maxwell data-sheet stating *an approximate* value of $2000 \, \text{m}^2 \text{g}^{-1}$ [13]. As this value is well with the accepted range, the value $2000 \, \text{m}^2 \text{g}^{-1}$ will be used to help populate Table 4.1.

Now the surface area per amount of carbon can be used to *estimate* the interfacial DL surface area for *each* of the two electrodes

$$a_{\text{dl}} = (5.8 \, \text{g}_{\text{carbon}}) \left(2000 \frac{\text{m}^2}{\text{g}}\right) = 11600 \, \text{m}^2 = 134 \times 10^6 \, \text{cm}^2,$$

where a_{dl} is no longer a *specific* value but rather a total value.

5.2.5 Electrode Capacitance

The capacitance of a porous electrode depends primarily on the specific capacitance of the DL and, of course, the actual DL surface area which relies on the amount of carbon present and its specific surface area. Just as with activated carbon surface area, there are

---

[1]The BCAP device is assumed to use an etched aluminum foil to increase the aluminum surface area as well as give better adhesion to the activated carbon. Some devices also have used an aluminum fiber cloth [8].

numerous sources giving the specific capacitance of activated carbon ranging from $40\,\mathrm{F\,g^{-1}}$ to $250\,\mathrm{F\,g^{-1}}$ [20, 67–69]. Given the estimated $5.8\,\mathrm{g}$ of activated carbon per electrode, *each* electrode could have a capacitance anywhere from $250\,\mathrm{F}$ to $1450\,\mathrm{F}$ and as the electrodes are in series, the total capacitance is halved and therefore could range from $125\,\mathrm{F}$ to $725\,\mathrm{F}$. The BCAP has an advertised value of $150\,\mathrm{F}$ which falls in the expected range, although at the lower end.

Using Eq. (4.9), with the minimum and maximum capacitance, the *specific* electrode capacitance can now be calculated, between the minimum and maximum values as

$$\frac{C_{min}}{a_{\mathrm{dl}}} \leq C \leq \frac{C_{max}}{a_{\mathrm{dl}}}$$
$$\frac{125\,\mathrm{F}}{134 \times 10^6\,\mathrm{cm^2}} \leq C \leq \frac{725\,\mathrm{F}}{134 \times 10^6\,\mathrm{cm^2}}$$
$$9.33 \times 10^{-7}\,\mathrm{F\,cm^2} \leq C \leq 5.4 \times 10^{-6}\,\mathrm{F\,cm^2}.$$

As with the interfacial surface area a_{dl}, the estimate for capacitance is largely dependent on which references are chosen. Estimating the capacitance by deconstruction is therefore probably not the optimal method but it can indeed be accomplished.

5.3   Circuit Element Measurement of a Maxwell EDLC

The second part of this chapter implements the methods from Chap. 4 on the BCAP to determine the four parameters: R_{ss}, R_{i}, R_{sep}, and C_{total}. The step response, EIS, and voltammetry are all used.

5.3.1   Step Response

The step response is obtained during either the constant current charge or discharge of a BCAP. The charge-discharge cycles consist of a series of $5\,\mathrm{s}$ constant current pulses across the advertised current range of the BCAP, from $10\,\mathrm{A}$, up to $55\,\mathrm{A}$, in $5\,\mathrm{A}$ increments. All testing in this section was carried out at approximately room temperature, or $20^{\mathrm{o}}\mathrm{C}$.

Test Setup

The BCAP to be tested was connected to an Arbin BT-2000 capable of providing the needed current and voltages. Heavy gauge copper wire was soldered to the BCAP terminals and connected to high current test leads to minimize wire and contact resistance. A DATAQ DI-148U data-logger, sampling the terminal voltage at 1 kHz, was connected across the terminals.

Test Procedure

To obtain a step response to a constant current, the pulse input shown in Fig. 5.5(a) is applied to the BCAP and the measured response shown in Fig. 5.5(b). The pulse cycle consisted of 10 s at 0 V, a 5 s constant current charge, 10 s of rest, meaning no current is applied and the voltage is allowed to float, then 5 s of constant current discharge, another 10 s of rest, and finally 10 s at 0 V. The initial current pulse amplitude was set to 10 A and then increased by 5 A per iteration, up to and including the maximum advertised allowable current of 55 A. As mentioned in Chap. 2, red plots are MATLAB generated while the blue contain the measured BCAP response data.

5.3.1.1 Low Current

Figure 5.6(a) shows the regions of interest in the BCAP response data and the plots in Figs. 5.6(b), (c), and (d), show the measurements of the voltages, leading to initial values

(a)   (b)
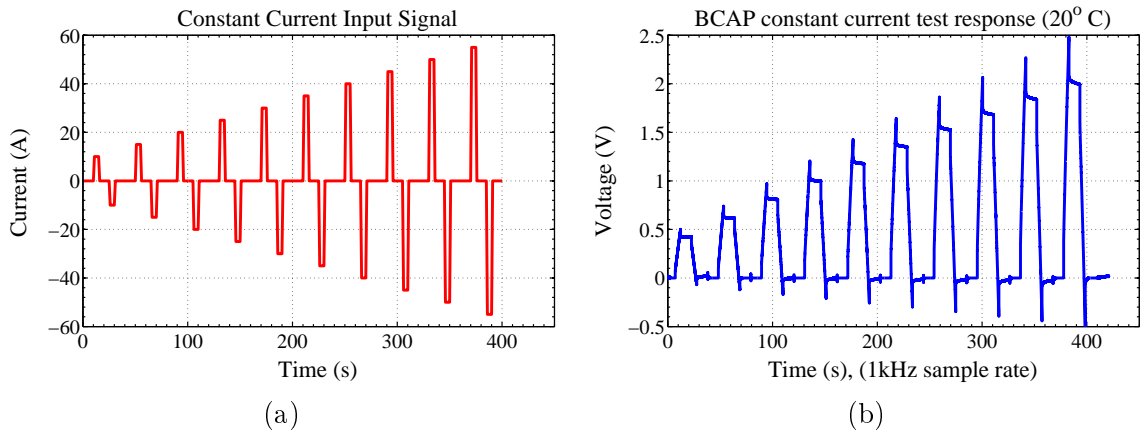
Figure 5.5:   Constant current test: (a) Input from 10 A to 55 A, and (b) Output
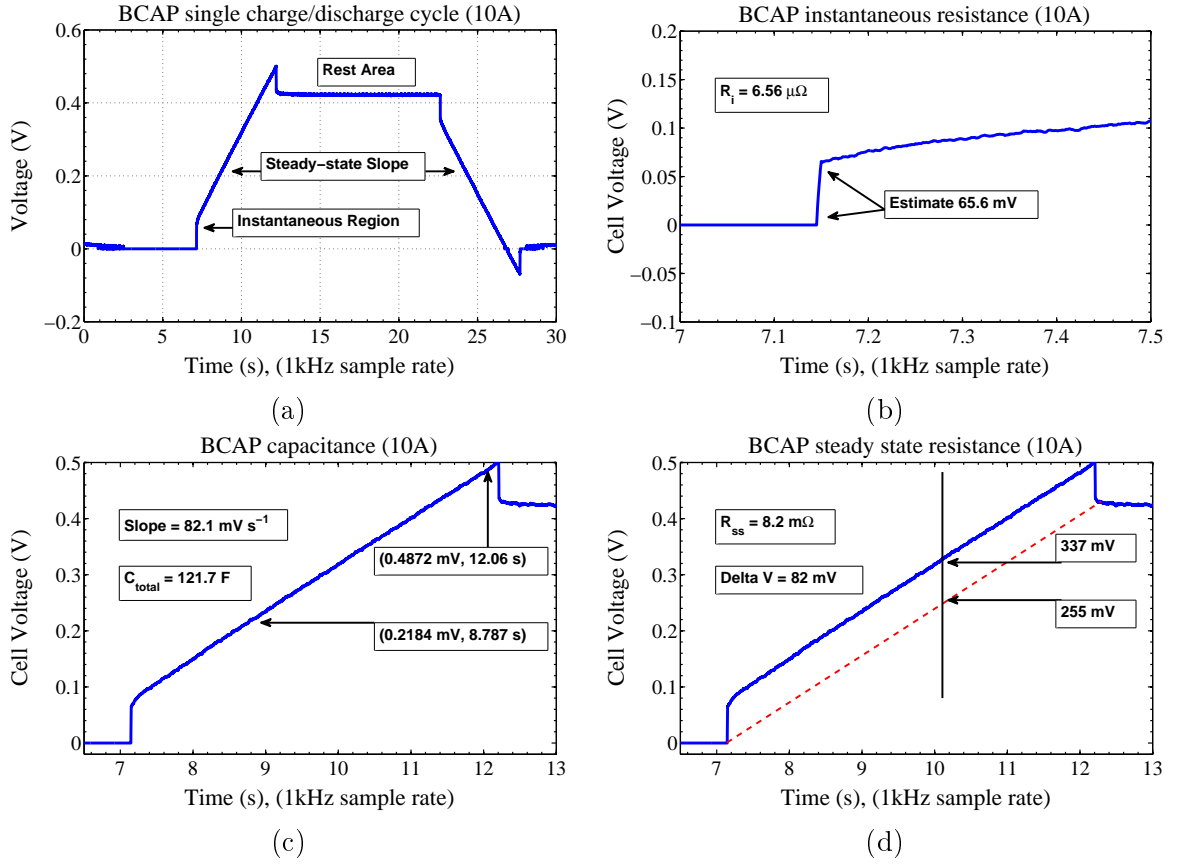
Figure 5.6: EDLC step response: (a) Response of complete cycle, (b) Instantaneous resistance, (c) Capacitance estimation, and (d) Charge curve for steady-state resistance

for R_{ss}, C_{total}, and R_{i}. All Fig. 5.6 plots were taken using an applied current pulse amplitude of 10 A. Approximate 12.5 mV of a dc bias, likely introduced by calibration errors between the Arbin system and the data logger was removed.

The four measured circuit-element parameters are the steady state resistance

$$R_{\mathrm{ss}} = \frac{82\,\mathrm{mV}}{10\,\mathrm{A}} = 8.2\,\mathrm{m\Omega},$$

the instantaneous resistance,

$$R_{\mathrm{i}} = \frac{65.6\,\mathrm{mV}}{10\,\mathrm{A}} = 6.56\,\mathrm{m\Omega},$$

and using half of the the smaller of R_{ss} and R_{i}, gives an initial separator resistance of

$$R_{\mathrm{sep}} = \frac{6.05\,\mathrm{mV}}{2} = 3.28\,\mathrm{m\Omega}.$$

The total device capacitance is measured to be

$$C_{\text{total}} = \frac{I_{\text{dc}}}{\text{slope}} = \frac{10\,\text{A}}{.0821} = 121.7\,\text{F}.$$

5.3.1.2   High Current

Two of the earliest DL researchers, Louis Gouy and David Chapman, independently made the observation that at higher currents, the DL capacitance was not constant as predicted. Their observations led to the first significant re-development of the Helmholtz model. A special consideration was therefore given to the 55 A portion of the test cycle. A summary of all ten current measurements of the BCAP is first given in Table 5.2, and in Chap. 6, is extended to the entire *temperature* range. For now, the 55 A measurements are given as

$$R_{\text{ss}} = 9.0\,\text{m}\Omega$$

$$R_{\text{i}} = 6.43\,\text{m}\Omega$$

$$C_{\text{total}} = 135.4\,\text{F},$$

and

$$R_{\text{sep}} = \frac{6.43\,\text{mV}}{2} = 3.22\,\text{m}\Omega.$$

From Fig. *5.7*, there are two observations. First, the capacitance is about 10% higher than that of the same device at room temperature. Second, there is a noticeable outward bow seen in the charging porting of the high current plot that is not evident in the low current plot. This observation may lead to a source of error as the *high current* slope measurement now depends on which two points are used, while at *low current*, almost any pair of points can be used.

A possible explanation for this type of behavior is that at high current, internal electrode pores not normally accessed, might be forced open from the high numbers of moving charges in the electrolyte. This is an area for future investigation, but for now, the present state of the physics-based model does not reflect either of these two observations.

The derivative of the time-domain step response is shown in Fig. 5.8 and also shows a non-constant term during the steady state region when the slope *should* be constant.
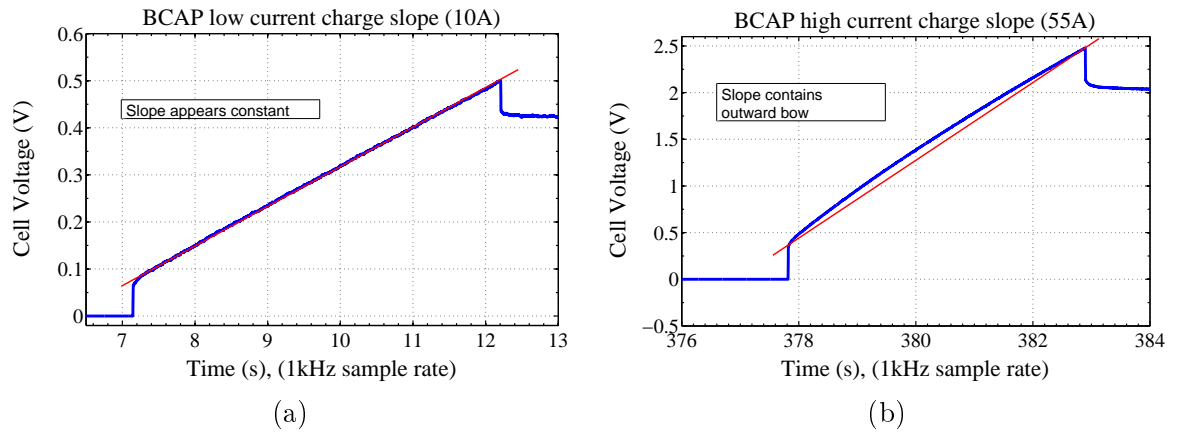
Figure 5.7: Slope during charge: (a) Low current (10 A) (b) High current (55 A)
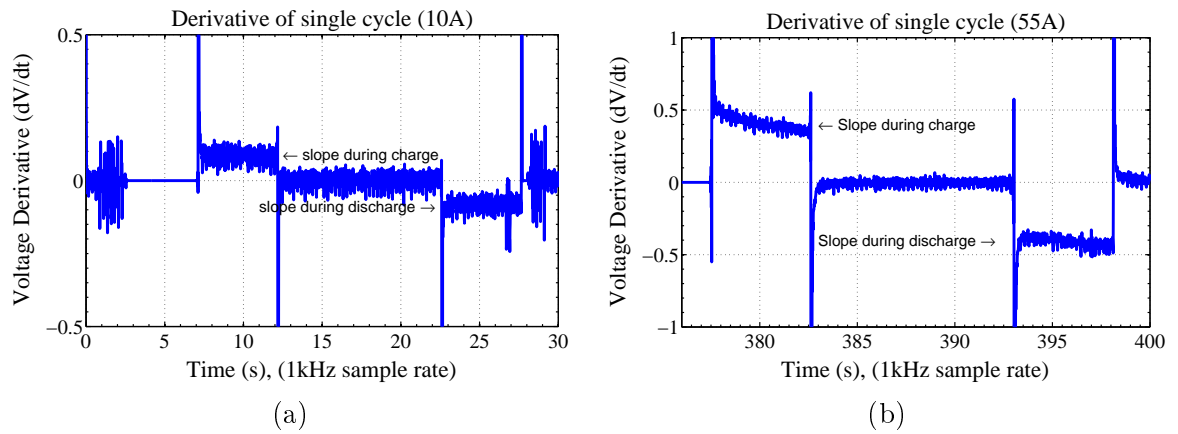
Figure 5.8: Derivative of charge-discharge curve: (a) At 10 A (b) At 55 A

TABLE 5.2:   BCAP measured data summary

	10 A	15 A	20 A	25 A	30 A	35 A	40 A	45 A	50 A	55 A
R_{ss} mΩ	8.2	8.0	8.3	8.4	8.8	8.8	8.9	8.9	9.0	9.0
R_i mΩ	6.56	6.33	6.33	6.11	6.38	6.39	6.36	6.39	6.45	6.43
R_{sep} mΩ	3.28	3.16	3.16	3.05	3.19	3.19	3.18	3.19	3.22	3.22
C_{total}(F)	120.5	121.7	123.4	125.1	127.6	129.4	130.9	131.9	133.9	135.4

5.3.1.3   Step Response Summary

A nice feature of the pulse test is that it steps through the entire advertised operating range of the BCAP in increments of 5 A per iteration. Table 5.2 provides a summary across a wide range of currents. The slope used for capacitance was taken from a point near the peak of the cycle and a point about in the middle of the cycle. The steady-state resistance used a point in the middle of the cycle. The term steady-state, as defined in Chap. 4, is still used but at high currents seems to no longer be a true steady-state.

5.3.2   Electrochemical Impedance Spectroscopy

A Gamry Reference 3000 Potentiostat system with a maximum current capability of 3 A was used to conduct potentiostatic testing of the BCAP. An identical series of tests were performed, each with a different dc bias voltage, across the advertised voltage range of the BCAP.

Test Setup and Procedure

The setup for a two electrode cell configuration with a Gamry Instruments potentiostat system is simple. The reference and counter electrode leads are connected to the negative terminal of the BCAP while the working electrode and sense leads are connected to the positive terminal. To minimize any lead wire effects, all leads were connected as close to the EDLC as possible. All tests were conducted at room temperature, across the frequency range of 100 kHz to 100 μHz. It may also be noted that tests at low frequencies will take a significant amount of time

The EDLC was charged to a particular dc voltage and allowed to remain at that particular dc voltage for a minimum of 10 minutes to ensure it was fully charged. The

potentiostat was set to the matching dc voltage and a small sinusoidal ac signal of $1\,mV$ RMS was applied to the BCAP.

5.3.2.1   EIS Results

When comparing results for EIS tests at varying dc bias points, there was very little change in the response. EIS was conducted over a range of dc voltages including: $0.1\,V$, $0.4\,V$, $0.7\,V$, $1.0\,V$, $1.3.0\,V$, $1.6\,V$, $1.9\,V$, $2.2\,V$, and $2.7\,V$, and the results are shown in Fig. 5.9. These results suggest there is no pressing need to modify the model to account for dc conditions and is also supported by the likely application of EDLCs to high current and power systems such as EVs, and not small signal filtering. Therefore the test at a dc bias of $1\,V$, is used to illustrate the results.

Figure 5.10 shows a typical Bode plot with impedance magnitude and phase and three immediate observations are noted. First, there is clearly an integrator pole at zero as indicated by the low frequency plot growing exponentially. Second, when the phase is near zero, the impedance seems to be just slightly below $10\,m\Omega$, equating well to the steady-state resistance measured earlier. Third, as the frequency increases, the phase does not level off after reaching zero, and near $1\,kHz$ increases with an approximate slope of 25° per decade. At the point where the high frequency slope begins, the impedance is in the $8\,m\Omega$ range, equating well to the instantaneous resistance, also measured earlier.

The high frequency phase shift is *possibly* due to wire lead inductance from the test leads but could also be due to other effects. It is *not* presently modeled by the original set of PDEs, or the ROMs, and would also be a candidate for further study. There is no Warburg impedance *evident* in these plots, however the Warburg impedance is a low frequency effect and were the frequency lowered sufficiently, could be expected to appear.

5.3.3   Voltammetry

An Arbin BT-2000 test system was used for voltammetry testing as described in Chap. 4 across the entire advertised BCAP temperature range of $-40\,^{\circ}C$ to $80\,^{\circ}C$. Chapter 6 contains the full set of temperature plots along with a brief discussion.
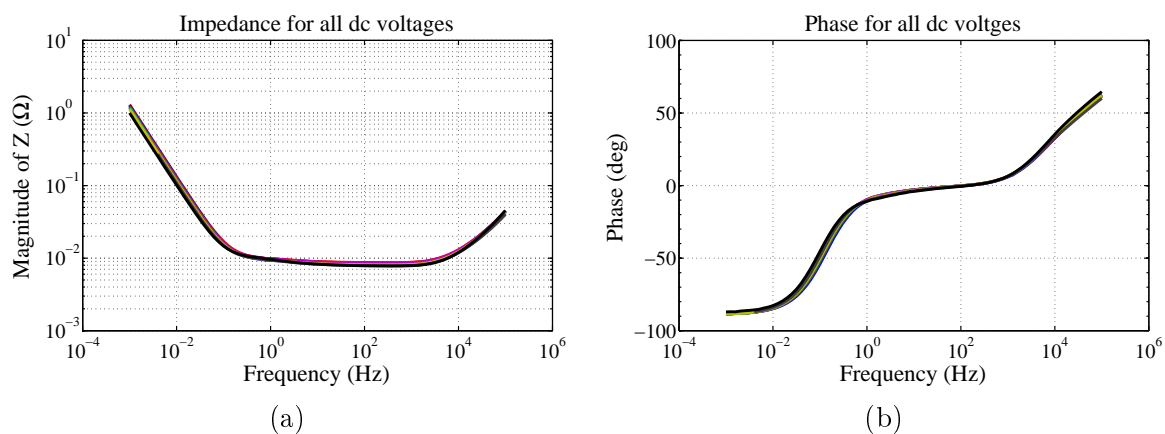
Figure 5.9: EIS at multiple dc bias voltages: (a) Impedance magnitude (b) Phase
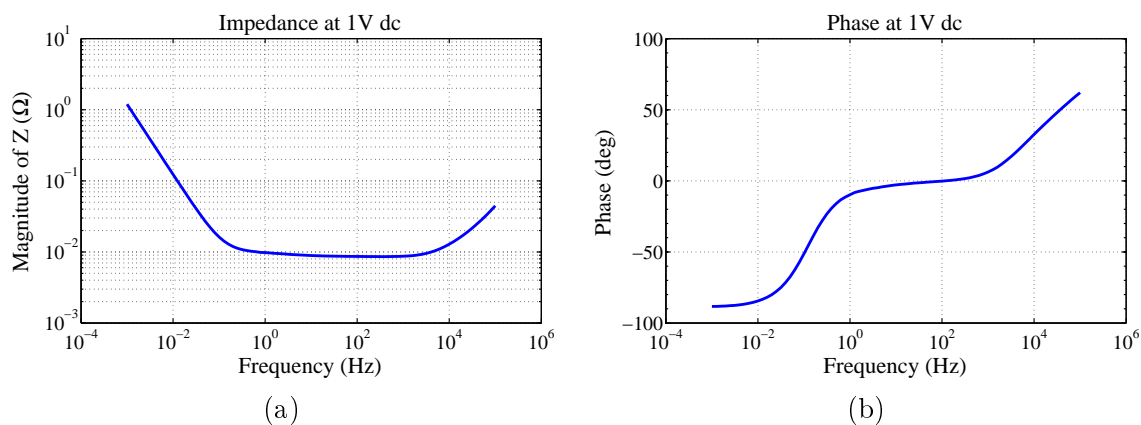
Figure 5.10: Bode plot at 1V dc: (a) Impedance magnitude (b) Phase
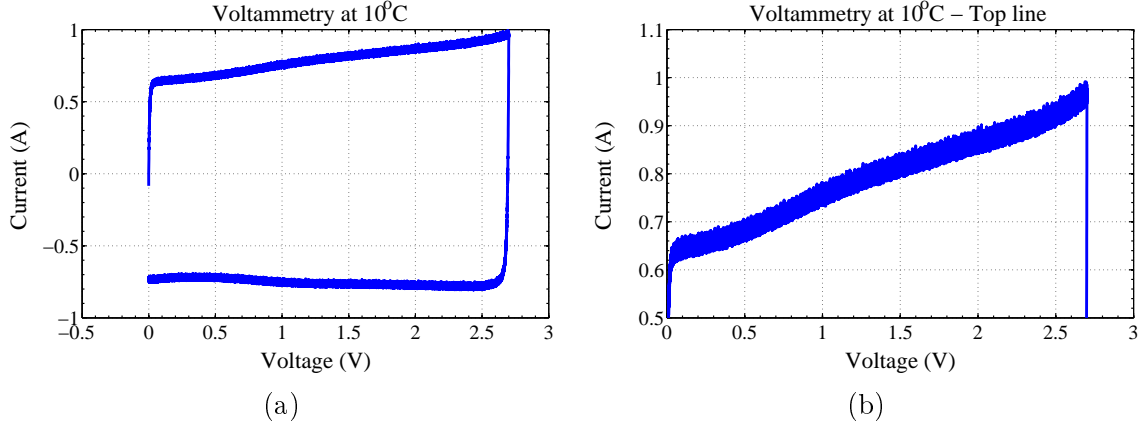
Figure 5.11: Voltammetry of BCAP - scan rate of $5\,\mathrm{mV\,s^{-1}}$: (a) Entire cycle (b) closeup of top line

Test Setup and Procedure

A pair of low current Arbin test leads were used as the high current leads have a slower data sampling rate and lower resolution. A scan-rate of $5\,\mathrm{mV\,s^{-1}}$ was used to sweep across the voltage range. Future voltammetry tests should be accomplished at multiple scan-rates but is left as an additional task that was not completed.

Figure 5.11 shows the full voltammetry plot and a zoom to just the top half of the plot. Because the EDLC is a real device and has non-ideal properties, the plot is *not* purely rectangular. There is nearly a 50 % increase in current from the low voltage to the high voltage range. The capacitance will therefore be determined near the two voltage extremes to obtain a range of values. Using the slope as the inverse of the scan-rate, $\frac{\mathrm{d}t}{\mathrm{d}V}$, and the estimated current, the capacitance at low voltage is given by

$$C = I\frac{\mathrm{d}t}{\mathrm{d}V} = (650\,\mathrm{mA})\left(\frac{1}{0.005}\right) = 130\,\mathrm{F},$$

while at high voltage it becomes

$$C = I\frac{\mathrm{d}t}{\mathrm{d}V} = (950\,\mathrm{mA})\left(\frac{1}{0.005}\right) = 190\,\mathrm{F}.$$

This range of possible capacitance values is clearly in line with the $150\,\mathrm{F}$ value as advertised by Maxwell and also further stresses the need to account for the capacitance that is clearly *not a constant.*

The increasing current *might* be partially explained by considering the device is not given sufficient time between voltage steps, defined by the scan-rate, to fully charge to the new voltage. Thus, when the next step occurs, it must not only charge to the new voltage but also catch up to where it left off from the previous voltage. The topic is worthy of further study and will be presented in the future works section of Chap. 7.

5.4   Parameter Extraction and Optimization

The previous section implemented three separate tests on a BCAP and obtained all the circuit-element measurements needed to implement an M-ROM. The M-ROM output can then be compared the BCAP output and the parameters optimized as was carried out in Chap. 4.

5.4.1   BCAP versus M-ROM with Unoptimized data

The four, unoptimized, circuit-element values just obtained are summarized in Table 5.3, and used to generate an M-ROM whose output will is compared with the real BCAP data. The EIS data indicates the frequency at which data is taken is quite significant. The steady-state resistance should be taken when the frequency is near zero while the instantaneous resistance measured at a high frequency, if possible.

Both of the M-ROM versus BCAP plots in Fig. 5.12 indicate a good, but not excellent, correlation between the M-ROM output and the BCAP response. A close look at the plots suggests the initial steady-state resistance measured values is slightly incorrect causing the instantaneous voltage drop error at the end of the pulse to be magnified. The error then propagates to subsequent parts of the plot.

TABLE 5.3:   BCAP measured data summary

	Step Response	EIS	Voltammetry
R_{ss}	$8.2\,\mathrm{m\Omega}$	$9\,\mathrm{m\Omega}$	-
R_i	$6.56\,\mathrm{m\Omega}$	$8\,\mathrm{m\Omega}$	-
R_{sep}	$3.28\,\mathrm{m\Omega}$	$4\,\mathrm{m\Omega}$	-
C_{tot}	$121.7\,\mathrm{F}$	-	$130-190\,\mathrm{F}$
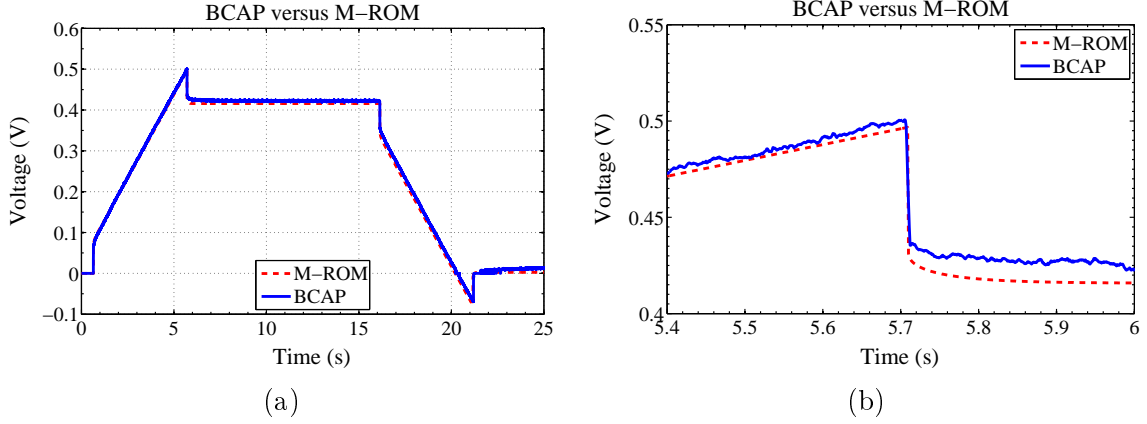
Figure 5.12:   M-ROM versus BCAP unoptimized: (a) Full cycle (b) End of response region

Additional error is introduced because the Arbin system is not as accurate, timing wise, as MATLAB. The MATLAB M-ROM simulation used a charge pulse of 5000 ms where the Arbin used a charge time of around 5100 ms. A very slight difference but one that can be significant over several cycles. The MATLAB script was manually edited to lengthen its step input time to almost match the start and stop time of the measured data. This does not change the actual error but at least partially removes a simulation artifact. In any case, it is clear the two plots agree rather well suggesting the measured data *process* is on target.

5.4.2   BCAP versus M-ROM with Optimized data

Following the procedures from Chap. 4, the four circuit element values now need to be optimized using the EIS data from the BCAP. This will fine tune the four measured values and provide a much improved M-ROM. Figure 5.13 shows the unoptimized EIS comparison to the BCAP. Comparing the two plots, there clearly is a high frequency response behavior the M-ROM simply does not model and the region will be omitted from the optimization process. therefore attempting to optimized over that region. Therefore the optimization will only consider frequencies up to about 100 Hz and, until the high frequency phase behavior has been resolved with the original PDE model, the most significant error will likely be with the impulse, or instantaneous resistance value.
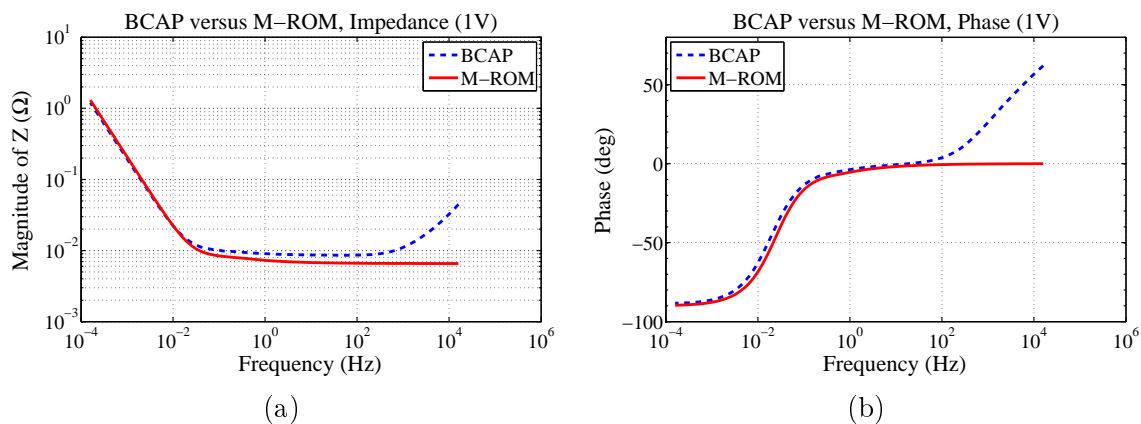
Figure 5.13:   EIS - BCAP versus M-ROM - Unoptimized
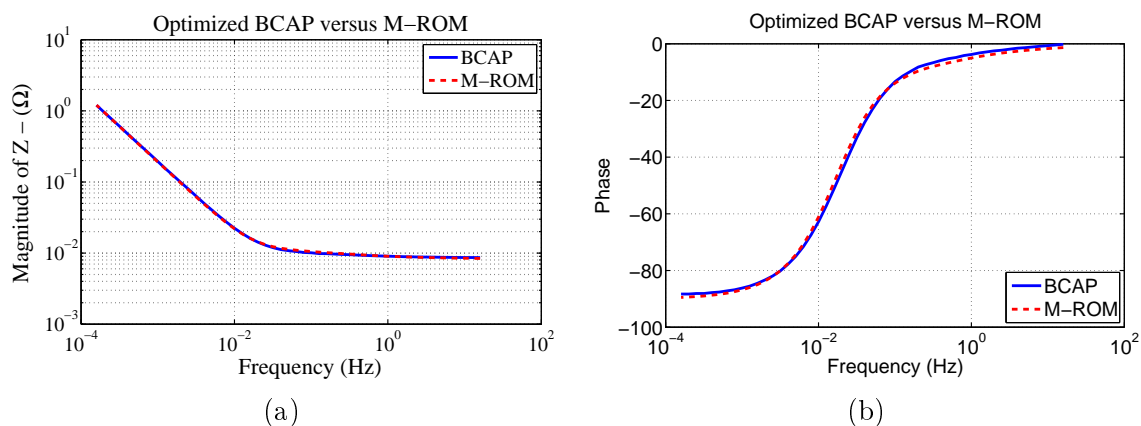
Figure 5.14:   EIS - BCAP versus M-ROM - Optimized

TABLE 5.4:   Circuit element summary of optimization

Parameter	Measured	Optimized
R_{ss}	$8.2\,\mathrm{m\Omega}$	$10.6\,\mathrm{m\Omega}$
R_{i}	$6.56\,\mathrm{m\Omega}$	$8.8\,\mathrm{m\Omega}$
R_{sep}	$3.28\,\mathrm{m\Omega}$	$4.9\,\mathrm{m\Omega}$
C_{total}	$121.7\,\mathrm{F}$	$132.1\,\mathrm{F}$
$C_{Electrode}$	$243.4\,\mathrm{F}$	$264.1\,\mathrm{F}$

Figure 5.14 shows the optimized M-ROM matching quite well with the BCAP, but not nearly as well as the prediction from Chap 4 suggested. Table 5.4 contains the unoptimized and optimized measured parameters.
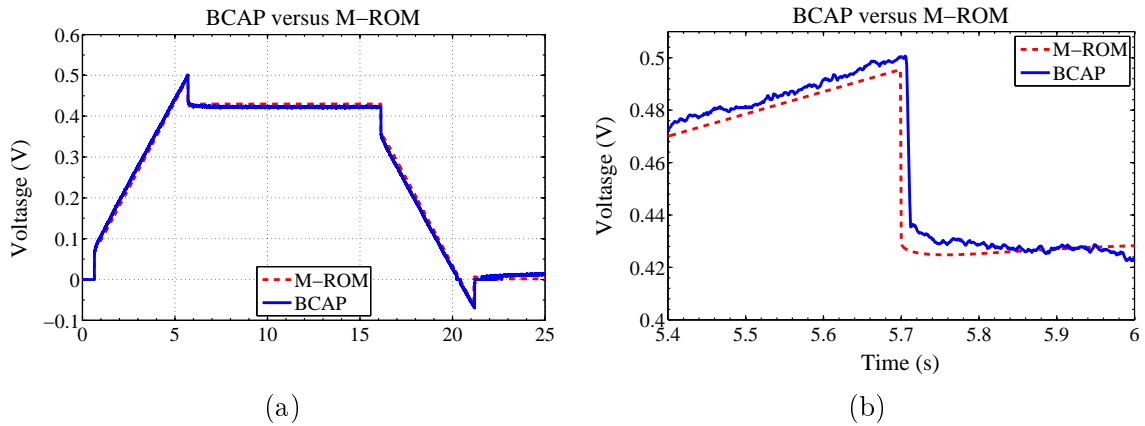
Figure 5.15:   M-ROM versus BCAP Optimized: (a) Full cycle (b) End of response region

After optimization, the M-ROM output is expected to almost perfectly match that of the BCAP response. In this case however, the optimization seemed to make the comparison worse, see Fig. 5.15, and here is where a problem occurs.   When optimizing measured parameters, the same physical device should be used. There is a problem however as the devices used to create the EIS data and the step response data were not the exact same device. They are both BCAP 150F EDLCs made by Maxwell—just not the same device. This is evident by the M-ROM that was optimized using EIS from one device to compare against a step test done on a different device.

5.4.3   BCAP Derived Parameters

Because the unoptimized data shows a much better fit than the optimized data due to the use of two different EDLCs for the two different tests, the conductivity parameter identification will use the unoptimized data. The *process* is the same regardless of which set of data is used. For future reference, using the same device for both EIS and pulse tests is required to make the optimization process meaningful. Some of the internal parameter values such as the specific conductivities should not vary significantly from device to device while others, like the double layer surface area or specific capacitance could well vary from device to device.

5.4.3.1 Parameters in Total Value Form

R_i, R_sep, and R_ss makeup the coefficients used to solve two identical quadratic equations with two unknowns, σ_total and κ_total. The quadratic, Eq. (4.20) is restated here

$$\frac{-b \pm \sqrt{b^2 - 4ac}}{2a} \Rightarrow \frac{-\frac{2}{R_\mathrm{sep}-R_\mathrm{i}} \pm \sqrt{\left(\frac{2}{R_\mathrm{sep}-R_\mathrm{i}}\right)^2 - 4\frac{4}{3(R_\mathrm{i}-R_\mathrm{sep})(R_\mathrm{ss}-R_\mathrm{sep})}}}{2} \Rightarrow \sigma_\mathrm{total} \text{ and } \kappa_\mathrm{total}.$$

Solving for σ_total and κ_total yields the total solid conductivity as

$$\sigma_\mathrm{total} = 406.5041\,\mathrm{s},$$

and the total conductivity in the solution as

$$\kappa_\mathrm{total} = 203.25\,\mathrm{s},$$

and the conductivity in the separator is estimated as

$$\kappa_\mathrm{s\text{-}tot} = \frac{1}{R_\mathrm{sep}} = 304.87\,\mathrm{s}.$$

C_total was measured earlier and its *total value* across the entire cell is

$$C_\mathrm{total} = aACL = 121.7\,\mathrm{F}.$$

5.4.3.2 Parameters in Specific Value Form

Since the internal dimensions were also measured earlier, the specific values of the conductivities and capacitance can be obtained by using the cross sectional area A, and the lengths L and L_sep to solve

$$\kappa_\mathrm{total} = \frac{A}{L}\kappa,$$
$$\sigma_\mathrm{total} = \frac{A}{L}\sigma$$
$$\kappa_\mathrm{s\text{-}total} = \frac{A}{L_\mathrm{sep}}\kappa_\mathrm{sep} = \frac{1}{R_\mathrm{sep}},$$

along with values for the cross sectional area A, and lengths L and L_sep, now become

$$\kappa = \frac{L}{A}\kappa_\mathrm{total} = \frac{0.001173\mathrm{cm}}{248\mathrm{cm}^2}203.25\,\mathrm{s} = 0.0009613\,\mathrm{s\,cm}^{-1}$$
$$\sigma = \frac{L}{A}\sigma_\mathrm{total} = \frac{0.001173\mathrm{cm}}{248\mathrm{cm}^2}406.5041\,\mathrm{s} = 0.001923\,\mathrm{s\,cm}^{-1}$$
$$\kappa_\mathrm{sep} = \frac{L}{A}\kappa_\mathrm{s\text{-}total} = \frac{0.005\mathrm{cm}}{248\mathrm{cm}^2}304.87\,\mathrm{s} = 0.00615\,\mathrm{s\,cm}^{-1}.$$

TABLE 5.5:   Final BCAP parameter values

Parameter	Description	Final Values	Units
σ	Specific solid conductivity in the electrode	0.001923	$\mathrm{s\,cm^{-1}}$
σ_{total}	Total solid conductivity in the electrode	406.5041	s
κ	Specific electrolyte conductivity in the electrode	0.0009613	$\mathrm{s\,cm^{-1}}$
κ_{total}	Total electrolyte conductivity in the electrode	203.25	s
L	Length of electrode	0.01173	cm
C	Specific capacitance	1.82×10^{-6}	$\mathrm{F\,cm^{-2}}$
L_{s}	Length of separator	0.005	cm
κ_{sep}	Specific conductivity in the separator	0.00615	$\mathrm{s\,cm^{-1}}$
$\kappa_{\mathrm{s\text{-}total}}$	Total conductivity in the separator	304.87	s
a	Specific interfacial electrode area	87×10^6	$\mathrm{cm^2\,cm^{-3}}$
a_{dl}	Interfacial electrode area	134×10^6	$\mathrm{cm^2}$
A	Cross sectional area	248	$\mathrm{cm^2}$

The last remaining values are the specific interfacial double layer surface area and specific capacitance. Neither of these values can be individually obtained therefore one must be estimated to determine the other. An estimated value for a_{dl} was obtained in Sect 5.2.4. This value is now used to obtain specific values for a and C.

$$a = \frac{a_{dl}}{AL} = \frac{134 \times 10^6\,\mathrm{cm^2}}{(248\,\mathrm{cm^2})\,(0.00615\,\mathrm{cm})} = \frac{87 \times 10^6\,\mathrm{cm^2}}{\mathrm{cm^3}},$$

and the specific capacitance C, now given by

$$C = \frac{C_{\mathrm{Electrode}}}{a_{dl}} = \frac{243.4\,\mathrm{F}}{134 \times 10^6\,\mathrm{cm^2}} = 1.82 \times 10^{-6}\,\mathrm{F\,cm^{-2}}.$$

Table 5.5 now contains all information needed to create a new T-ROM. It should be noted, however, the interfacial surface area a_{dl} is very much an estimate as derived in the deconstruction section at the beginning of this chapter.

5.4.3.3 Maxwell BCAP Data-sheet

Reviewing the official Maxwell BCAP data-sheet [70] provides only a minimal level of validation for the data in Table 5.5. The data sheet lists the maximum ESR, at dc, as $14\,\text{m}\Omega$. Other data is purely performance related and does not *confirm* or *deny*, any of the other internal parameters. Neither is there a tolerance specification or a relation showing operation under high current conditions.

The data-sheet does however, give an indication that some of the tests conducted in this chapter may have exceeded recommended operating limits and may not have been conducted under the same conditions as used for the data-sheet values. While every effort was made to remain in the advertised operating ranges, there were several times, during the initial test setup, that either voltage or current limits were exceeded. The tests were modified when violations occurred however, it is possible, but unlikely due to the minimal time spent out of specifications, that internal cell damage could have occurred.

5.5 Summary

This chapter began with a deconstruction of a commercially available EDLC to obtain internal dimensional data. Ideally, this data allows the derivation of *specific* internal parameter values. A T-ROM can be created using derived BCAP internal parameters that should validate well with any M-ROM created from only the four measured circuit-element parameters, and also with a real EDLC.

The ideal case however, however, is not what generally happens. EDLC performance characteristics, such as capacitance, are likely to differ from part to part. Internal parameters and components, such as the electrolyte and electrode compositions, are assumed to be consistent, but, as they interact with the separator and solid electrode, small manufacturing differences or defects, may cause noticeable differences in part to part performance.

Two recommendations are therefore made: (1) For simple modeling, use the measurable circuit-element data to create an M-ROM that will provide very good, but not perfect, data. (2) If the T-ROM level of modeling accuracy is required, perform EIS and pulse testing on the actual device to be used.

The methods performed in this chapter illustrate the general accuracy of the modeling *process* via the circuit-element approach. In certain cases, where the same device is used for both measuring and modeling efforts, nearly all internal component values can be identified. The circuit-element method would likely be preferred over the more detailed internal parameter method when systems such as EVs or other large energy storage are considered.

Chapter 6 presents an extension that takes the ambient temperature, for all current levels, into account.

CHAPTER 6

Extending the Model with Environmental Temperature Effects

6.1 Introduction

EDLCs are generally advertised to be capable of operating between $-40\,^{\circ}\text{C}$ and $80\,^{\circ}\text{C}$. Tests to this point have all been performed at room temperature, approximately $20\,^{\circ}\text{C}$, and none of the models have accounted for temperature in any way. The general behavior of an EDLC can be expected to change with ambient, or operating temperature, and it would be desirable that the model included at least a minimal temperature dependance.

The majority of EDLC thermal studies and literature consists of modeling heat generation and its transfer out of the EDLC [71, 72]. Others have considered local phenomena such as the electrolyte conductivity at different temperatures [73, 74]. The efforts of Pilon [75–77], also using a physics based model, is somewhat similar to similar to the work in this dissertation. His modern physics models start with a description similar to that shown in Chap. 2, Fig. 2.4 and take a somewhat similar approach, minus the DRA. For thermal analysis though, he goes the route of heat generation and dissipation.

This chapter provides a simple method to extend the previously introduced. Operation at very high, or very low, temperature may cause accelerated aging or degradation possibly leading to a reduced lifetime. A decreased capacitance, rise in internal resistance, and a decrease in the self-discharge resistance, might all occur. If control systems are able to predict what operating conditions are the most harmful, they might be able to mitigate such conditions but they cannot do so without accurate models.

The effect of heat generation and dissipation are specifically *not* considered but instead, the effect on *performance* is noted and methods to modify the appropriate ROMs are given. This chapter is split into three main sections:

- Physical effects of temperature on components. A brief look at which components are most likely to be affected by thermal variation and additionally, how the variations might affect the performance of the device.

- Temperature testing. The BCAP is cycled through the pulse test as done in Chap. 5 but this time in 20°C increments between the temperature range of -40°C and 80°C. At each temperature, the instantaneous and steady-state resistances are measured using the methods from Chap. 4. The capacitance is also measured and recorded. A brief data analysis discussion is included.

- ROM modification. With a good understanding of how the measured values change with temperature, appropriate changes to the model can be made. Simple changes such as just adding a temperature coefficient, or complex modifications such as including the temperature as a system PDE variable along with location and time.

6.2   Temperature, Components, and Properties

If the EDLC behavior changes over temperature, it may not be clear exactly which part of the device is causing the changes and therefore, it is prudent to discuss probable temperature effects on the individual components, materials, and electrical properties such as capacitance.

6.2.1   Temperature Effect on Individual Components and Materials

Current Collector and Metal Leads

Resistivity in aluminum varies less than $5\,\text{n}\Omega\,\text{m}$ [53,54], over the standard temperature range of operation of -40°C to 80°C. Although even a small amount of resistance will have *some* effect, it would take an extremely high current to have a *significant* effect. If a 100 A current, nearly double the maximum advertised current for a BCAP, were applied, the aluminum

components would only be responsible for a maximum voltage variation of around $5\,\mu$V. This amount of voltage change is obscured by the much larger electrolyte and separator voltages.

Activated Carbon part of Electrode

There are only a few studies on the temperature dependence of the of activated carbon by itself [73, 74]. With a room temperature resistivity of approximately $3.5 \times 10^{-5}\,\Omega$m, they indicate temperature changes on the order of $0.01 \times 10^{-5}\,\Omega$m per 10°C [78]. This leads to the conclusion that there is only a very small temperature dependence in the solid part of the electrode.

Electrolyte

The conductivity of the electrolyte is left as the primary source of performance variance over temperature. Unwanted electrochemical reactions in the electrolyte such as oxidation, if they occur, are generally accelerated at higher temperatures as suggested by the Arrhenius equation. Ravdel [79], performed a study on the conductivity of electrolytes used in lithium-ion batteries. Their results indicate an increase in conductivity as temperature increases. They also observed that conductivity does *not* follow the Arrhenius equation as predicted. The electrolyte itself may freeze, or, at high temperatures, becomes more conductive allow ions to flow more easily. If changes in temperature do cause an increase or decrease in conductivity, is it a linear or non-linear change? Linear changes are simple to model, but non-linear data may require other methods. [80].

Separator

The porous separator *material* is *assumed* to not vary significantly over temperature changes although it is possible its pores could shrink or grow. The separator resistance, on the other hand, is based on the electrolyte conductivity within the separator and is *likely* to change with temperature.

Physical Dimension

There are no materials in an EDLC that should demonstrate any significant changes in physical size due to temperature. Physical dimensions are not expected to vary significantly with temperature although thermal expansion could occur as the temperature increases.

Interfacial Double Layer Surface Area

The surface area a, as defined in earlier chapters, is not likely to change significantly as it is made of activated carbon. What *might* change however, is the pore size as the electrode expands and contracts, even slightly.

6.2.2   Temperature Effect on Device Properties

Capacitance

Because capacitance is defined in terms of current and the change in voltage over a specific time, a change in conductivity of the electrolyte can be expected to cause a change in capacitance and should be observable in the step response. Additionally, it is possible, that at high temperatures, the carbon electrode material could expand slightly, making small pores in the porous electrode even smaller. The ions in the electrolyte, at different temperatures, may themselves have larger or smaller ionic radii and might also be more or less mobile. These factors could both potentially affect the device capacitance.

Resistance and Conductivity

Resistance to the flow of electrons in the metal or activated carbon solid phase is not significantly temperature dependent; therefore those components are not considered. Ionic flow however, in a battery or EDLC, is very dependent on the conductivity of the electrolyte which has been shown to have a clear temperature relation [79]. As resistivity is the inverse of conductivity, resistance is expected to decrease as temperature increases while conductivity increases with temperature.

6.3 Temperature and Performance Measurements

The pulse cycle input from Chap. 4, was repeated across the full allowable temperature range of the BCAP. Tests were conducted across $-40\,^{\circ}$C to $80\,^{\circ}$C in increments of $20\,^{\circ}$C, while applied currents ranged from $5\,$A to $55\,$A. Although the BCAP data-sheet indicates $-40\,^{\circ}$C as the lower limit, the electrolyte, acetonitrile freezes at $-43\,^{\circ}$C so care must be taken at low temperatures.

All tests were conducted in a thermal chamber. Starting at $20\,^{\circ}$C, the temperature was raised and lowered in 20° increments, to cover the required testing range of: $-40\,^{\circ}$C, $-20\,^{\circ}$C, $0\,^{\circ}$C, $20\,^{\circ}$C, $40\,^{\circ}$C, $60\,^{\circ}$C, and $80\,^{\circ}$C. A minimum of one hour was allowed for the BCAP to acclimate to each new temperature. The pulse test and analysis procedure is the same as that used described in Sect. 4.4.

6.3.1 Pulse Response Summary

For each test cycle, capacitance, steady-state resistance, and instantaneous resistance were measured. For ease of interpreting the plots, the legends only list several data series. Capacitance versus temperature and current are given in Fig. 6.1 and Table 6.1, steady-state resistance measurements in Fig. 6.2 and Table 6.2, and the instantaneous resistance data in Fig. 6.3 and Table 6.2.

Capacitance Variation

The capacitance, as expected, shows an increase with increasing current of roughly $8\,$F per $10\,^{\circ}$C. Figure 6.1(b) also shows a peak value at $0\,^{\circ}$C and a minimum value at $20\,^{\circ}$C,

TABLE 6.1: Capacitance (F) with varying current and temperature

	10 A	15 A	20 A	25 A	30 A	35 A	40 A	45 A	50 A	55 A
$-40\,^{\circ}$C	120.6	123.6	128.4	132.2	136.2	139.9	138.4	140.2	141.6	143.1
$-20\,^{\circ}$C	121.1	124.1	128.0	132.1	136.7	140.1	142.5	144.1	145.7	146.8
$0\,^{\circ}$C	118.5	122.8	127.1	133.1	137.0	140.4	143.7	144.9	147.2	147.8
$20\,^{\circ}$C	120.5	121.7	123.4	125.1	127.6	129.4	130.9	131.9	133.9	135.4
$40\,^{\circ}$C	117.6	120.4	122.0	125.0	127.7	130.0	132.2	134.1	135.5	137.0
$60\,^{\circ}$C	116.7	120.8	122.9	125.7	128.3	130.6	133.3	135.3	137.0	139.1
$80\,^{\circ}$C	117.4	120.5	123.5	126.1	129.7	132.0	134.3	136.3	138.9	141.1
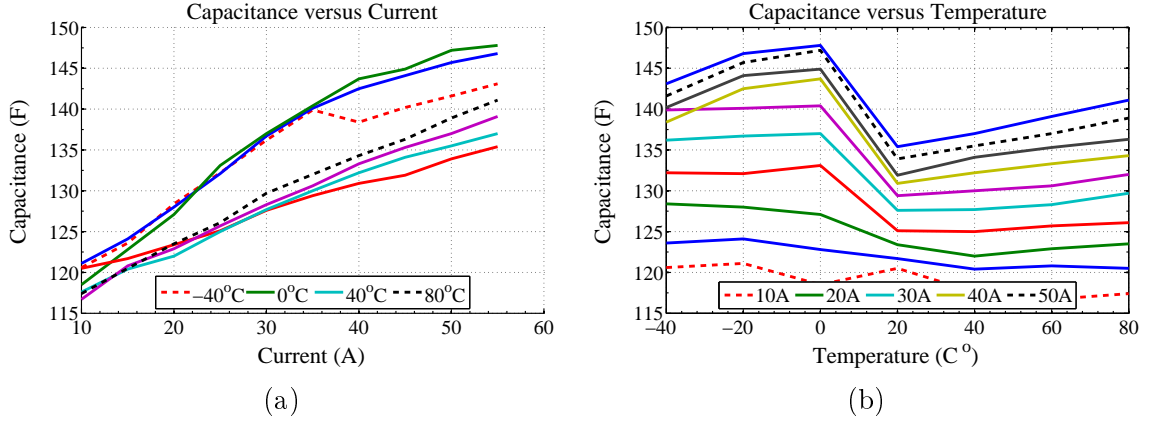
Figure 6.1: Capacitance: (a) Versus current, and (b) Versus temperature

TABLE 6.2: Steady state resistance (mΩ) with varying current and temperature

	10 A	15 A	20 A	25 A	30 A	35 A	40 A	45 A	50 A	55 A
−40 °C	10.6	10.9	11.5	11.7	11.9	12.0	11.1	10.8	10.6	10.4
−20 °C	9.2	9.6	10.0	10.4	10.9	11.1	11.1	10.9	10.8	10.7
0 °C	8.2	8.8	9.5	10.3	10.5	10.7	10.9	10.6	10.7	10.5
20 °C	8.2	8.0	8.3	8.4	8.8	8.8	8.9	8.9	9.0	9.0
40 °C	7.8	8.2	8.3	8.7	9.0	9.0	9.1	9.2	9.1	9.2
60 °C	7.8	8.3	8.5	8.8	9.0	9.2	9.3	9.4	9.4	9.6
80 °C	8.2	8.3	8.8	9.0	9.4	9.5	9.6	9.6	9.8	9.9

suggesting there are at least two temperature dependent internal parameters contributing to the capacitance.

Steady-State Resistance Variation

The steady-state resistance shows an increase until about 40 A at which point the increase seems to taper off. The resistance shows a marked drop at lower temperatures with a sudden turn around near 20 °C. Above this temperature, the conductance slowly rises indicating a the temperature exerts a somewhat stronger influence than current.

Instantaneous Resistance Variation

The Instantaneous resistance seems to show a very slight dependance at low and high currents but looks to be rather flat in the middle range. The same holds for the low and high temperatures, there is a flat region in the middle and an increase towards both extremes.
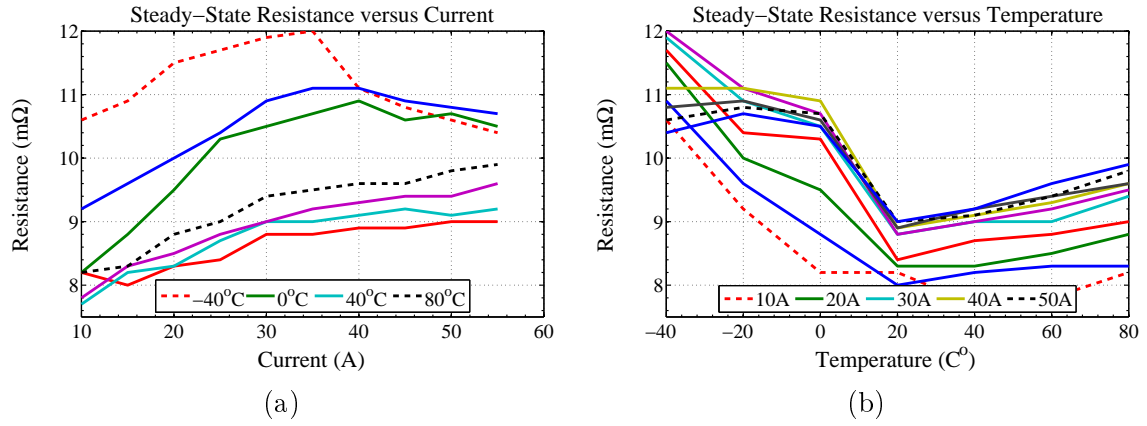
Figure 6.2:   Steady-state resistance: (a) Versus current, and (b) Versus temperature

	10 A	15 A	20 A	25 A	30 A	35 A	40 A	45 A	50 A	55 A
$-40\,^{\circ}$C	6.41	6.77	6.78	6.76	6.7	6.65	6.8	6.55	6.39	6.35
$-20\,^{\circ}$C	6.32	6.31	6.42	6.1	6.37	6.27	6.27	6.15	6.15	5.8
$0\,^{\circ}$C	6.27	6.31	6.27	6.23	6.25	6.33	6.23	6.22	6.14	6.18
$20\,^{\circ}$C	6.56	6.33	6.33	6.11	6.38	6.39	6.36	6.39	6.45	6.43
$40\,^{\circ}$C	6.05	6.56	6.34	6.42	6.44	6.10	6.45	6.40	6.40	6.46
$60\,^{\circ}$C	6.00	6.51	6.51	6.42	6.54	6.14	6.51	6.56	6.61	6.60
$80\,^{\circ}$C	6.075	6.36	6.6	6.67	6.65	6.71	6.71	6.64	6.76	6.47

TABLE 6.3:   Instantaneous resistance with varying current and temperature

Figure 6.3:   Instantaneous resistance: (a) Versus current, and (b) Versus temperature
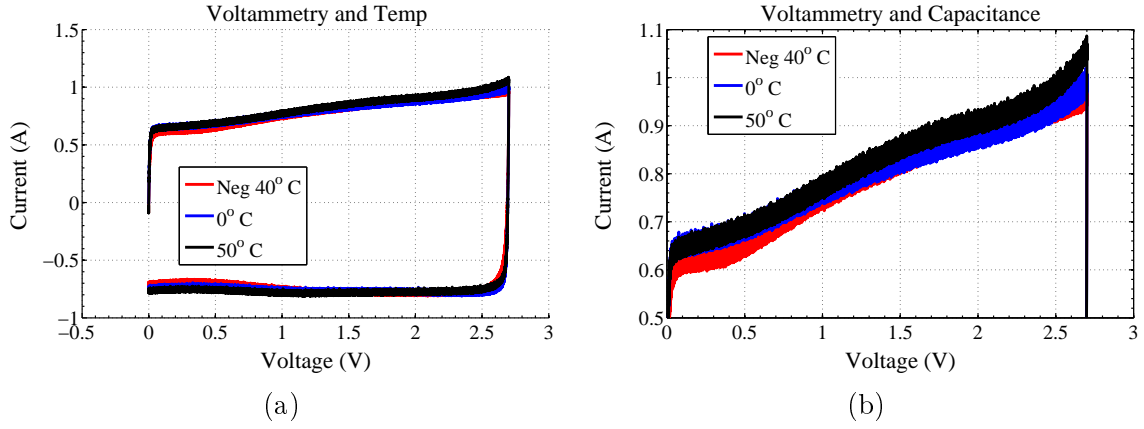
Figure 6.4: Voltammetry at: (a) $-40\,^{\circ}$C, $0\,^{\circ}$C, and $50\,^{\circ}$C, and (b) Closeup of top line

6.3.2 Voltammetry and Temperature Summary

Voltammetry testing was introduced in Chap. 4 but only one set of data was shown. Here, the results of voltammetry tests using a scan-rate of $5\,\text{mV}\,\text{s}^{-1}$ and a temperature range of: $-40\,^{\circ}$C, $-20\,^{\circ}$C, $-10\,^{\circ}$C, $0\,^{\circ}$C, $10\,^{\circ}$C, $30\,^{\circ}$C, $40\,^{\circ}$C, and $50\,^{\circ}$C, are summarized. Data from the higher temperature tests was corrupted and not available. The voltammetry plots show only a minimal change with temperature and therefore only plots for the lowest, highest, and zero temperatures are shown.

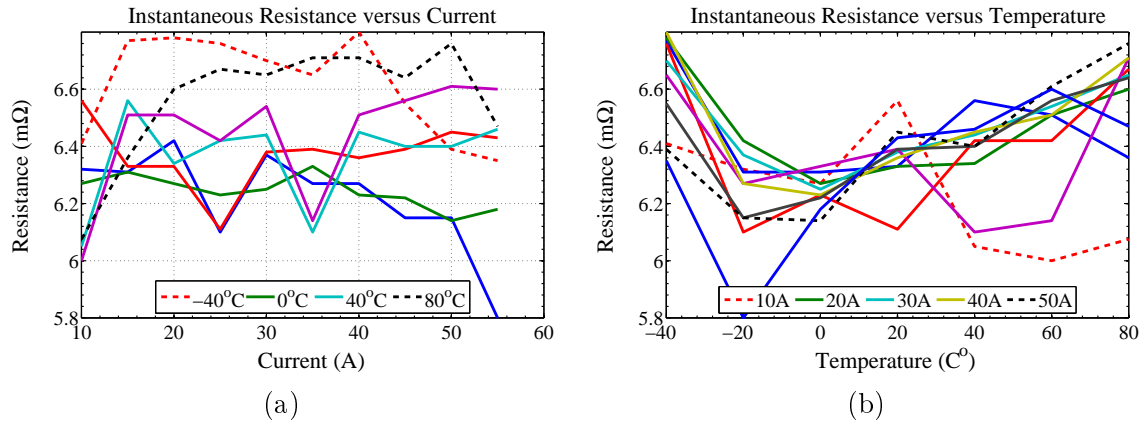Figure 6.4(a) shows the full voltammetry plot, and Fig. 6.4(b) shows a closeup of only the top line in (b). The 50 °C test shows the greatest variation between charge and discharge current while the $-40\,^{\circ}$C shows the least variation. It is also clear the capacitance increases with voltage as indicated by the rising current as the voltage also rises. The middle of Fig. 6.4(b) shows the least variance in current between temperatures and is a good place to measure capacitance.

Table 6.4 gives a good summary of the estimated capacitance at three very different temperatures and at three voltage locations in Fig. 6.4(b). The capacitance is determined at 0.4 V, 1.5 V, and 2.6 V using

$$C = I\frac{\mathrm{d}t}{\mathrm{d}V}.$$

Clearly there is an increasing capacitance as the temperature increases and the capacitance at different voltage points also indicates an increased current, hence an increased

TABLE 6.4:	Capacitance versus Temperature and Voltage		
	0.4 V	1.5 V	2.6 V
$-40\,^{\circ}$C	128 F	162 F	187 F
$0\,^{\circ}$C	136 F	164 F	190 F
$50\,^{\circ}$C	136 F	170 F	202 F

capacitance. To better understand the voltammetry data, the tests need to be accomplished at additional scan rates, both higher and lower. The apparent increase in capacitance might be due only to the fact that the capacitor is not allowed to fully charge at each step and so as the voltage increases, the current has to try and *catch-up*. Low scan-rates may indicate true capacitance much more clearly than high scan-rates.

6.3.3 Temperature and EIS

EIS was not performed at any temperature other than 20°C.

6.3.4 Error Analysis

During the test procedures described above, there are several sources of possible error that may have influenced results:

(1) The device was allowed to acclimate for a minimum of one hour at each temperature prior to testing. While it is a small device about the size of a C-cell battery, the ambient temperature might not have been given sufficient time to percolate through the entire EDLC. A test specification sheet from Maxwell suggested a minimum of 6 hours of a temperature soak prior to testing.

(2) The data-logger introduced a dc bias of approximately 12 mV likely due to calibration differences between the data-logger and the Arbin test system. The bias is easily removed in MATLAB at the beginning of the data processing steps and if it is indeed a calibration problem, no other error is introduced. If, however, the bias is the result of an actual test-setup problem, the possible error could have a larger effect when current was applied.

(3) As the applied current increases, the charge curve begins to develop a noticeable outward curve or bulge during the steady-state charge. Because the slope of the steady-state region is used for capacitance calculations, small deviations in the calculated values may occur depending on which points are used to determine the slope.

(4) The thermal voltammetry testing was carried out over several weeks time and it was not until several months, post test, that the thermal chamber was discovered to be functioning incorrectly. These tests were not re-accomplished and it is possible the voltammetry data, at the higher temperatures, may be skewed. This problem does not extend to the pulse response tests as a separate thermal chamber was used.

6.4   ROM Parameter Modifications

Clearly there is both a current magnitude dependence as well as temperature dependence. As this chapter is titled *Extending the Model with Environmental Temperature Effects*, only temperature modifications to the models will be discussed and those modifications reflecting *current* variations, although interesting, will be left as a future work.

There are two general approaches to changing the model. First, the original set of PDEs can be modified to include temperature as an additional function parameter along with distance x, and time t. This process would require a significant amount of rework to re-develop the Chap. 3 transfer functions.

A second approach is based on the idea that the electrolyte conductivity is the primary parameter affected by ambient temperature and the specific capacitance is the second most affected. Up to now, κ and κ_{sep}, and C, have all been considered constants; however if the temperature profile can be fully obtained and written in a piecewise form, κ, κ_{sep}, and C, can all be re-written to account for thermal variation.

Therefore new equations will need to be developed, for the two electrolyte conductivities along the lines of

$$C \Rightarrow \alpha_1 C$$

$$\kappa \Rightarrow \alpha_2 \kappa$$

$$\kappa_{\text{sep}} \Rightarrow \alpha_3 \kappa_{\text{sep}},$$

where the new terms are defined, piecewise, over the temperature T as

$$T_1 \leq \alpha_1, \alpha_2, \alpha_3 \leq T_2$$

$$T_2 \leq \alpha_1, \alpha_2, \alpha_3 \leq T_3$$

$$T_3 \leq \alpha_1, \alpha_2, \alpha_3 \leq T_3,$$

and using as many *pieces* of T as desired.

The piecewise temperature modeling of the four M-ROM measured parameters follows a similar approach with

$$R_{\text{ss}} \Rightarrow \beta_1 R_{\text{ss}}$$

$$R_{\text{i}} \Rightarrow \beta_2 R_{\text{i}}$$

$$C_{\text{total}} \Rightarrow \beta_3 C_{\text{total}},$$

where β is the temperature dependent value.

6.5   Summary

This chapter discussed the temperature dependence of an EDLC. Device components were individually considered with respect to their expected behavior and only the specific conductivities of the electrolyte and the specific capacitance were determined to be significantly affected by ambient temperature. Temperature tests were conducted across the advertised operating range and the pulse response test conducted at particular temperatures. The results were not linear as expected but rather indicated a non-linear temperature dependence.

Two methods to account for the non-linearity in the ROM models were discussed with the preferred method being the piecewise redefining of the specific conductivities and specific capacitance.

CHAPTER 7

Conclusions and Future Work

This dissertation focuses on the creation and optimization of a reduced order model of a electrochemical double layer capacitor. Chapter 3 presented the ROM derivation by first developing transfer functions, and subsequently developing a discrete-time state-space implementation through the use of the discrete-time realization algorithm as introduced previously by Lee [4]. Though validation against a numerical PDE implementation, the ROM was shown to be accurate with only a small error that was mostly attributed to a simulation artifact.

Chapter 4, introduced a method to re-write the ROM in terms of circuit-element parameters. While not true circuit elements, they can be obtained through measurements taken from the response of an EDLC. Using these measured values, an M-ROM was created and shown to be a nearly identical match to the control data generated by the Chap. 3 ROM. With a validated process, the development of the M-ROM can be extended to modeling a commercially available EDLC. Additionally, a process was introduced to identify nearly all of the internal parameters of an EDLC.

Chapter 5 described a simple device deconstruction process to obtain dimensional data needed to completely estimate nearly all internal parameters. The specific capacitance and interfacial double layer surface area cannot be disambiguated without additional materials testing methods. The Chap. 4 process was then used on a Maxwell Boostcap EDLC, and with the dimensional data also now available, was able to not only create a M-ROM that matched the behavior of the real device, but also completely identified values for all of the internal parameters.

Finally, as the original PDE model does not consider temperature, sets of Chap. 4 data were collected from the real device as it was cycled across its advertised temperature range.

An analysis was accomplished and an easy method to add temperature to the model was presented.

This dissertation presented an approach to modeling of an EDLC that improves on previous models by using techniques from lithium-ion cell modeling. The techniques have been shown to be sound, and when validated against real devices, show a very close match. There is however, additional work that might be accomplished to further improve the M-ROM and T-ROM EDLC models developed here.

7.1 Future Work

7.1.1 Areas for Model Refinement

While the M-ROM as presented performs well in some conditions, it clearly needs some additional work to improve its performance. There are several areas that immediately come forward as relevant future work areas.

High current effects: Add the effect of high current behaviors to the M-ROM. Chapter 6 clearly indicates a noticeable performance difference when the EDLC is operated at high current levels. The primary parameter affected is the capacitance which implies there is a change, somehow, in the effective double layer surface area. In the M-ROM, the steady-state resistance is also affected. The current M-ROM does not account for the high current capacitance differences.

Model generalization: Generalize the optimization process. As became evident in Chap. 5, measured values, especially those taken in EIS studies, can vary from device to device, even with the same part number and from the same manufacturer. This variance makes the optimization difficult in a general sense. Optimized data from one part is unlikely to exactly match optimized data from another part.

Voltammetry: Expand on the applicability of using voltammetry methods to better understand the behaviors and characteristics of the internal components. Voltammetry, in Chap. 5, quickly indicated the changing current as the applied voltage increased. This is also related to the high-current effect area for model refinement.

High frequency behavior: During the EIS study of the real device, there was a high frequency phase shift not accounted for by the M-ROM. Because the primary location of error on the time-domain results occurs directly after the input signal changes, this area would be a prime target of additional investigation.

7.1.2   Additional Observations, Applications, and Notes

EDLCs find their most likely use to be with applications requiring large currents such as battery systems in EVs. As with batteries, however, they will have to be stacked in series, and will require a voltage monitoring system. The M-ROM may provide a very good start to the development of such a system.

Leakage current has not been addressed but may not be a relevant issue. EDLCs used with battery systems would be primarily concerned with sinking or sourcing the occasional high current. In this application, the EDLCs are not meant for long term storage.

Finally, the study of how EDLCs degrade over time is somewhat relevant. Because they do not *die* as quickly as lithium-ion cells, this area is not as crucial; however it is worth considering.

Bibliography

[1] "Porous electrode SEM image," http : / / chemistry . stackexchange . com / questions / 11042 / how-does-activated-carbon-bind-the-adsorbate, last accessed Apr 20, 2015.

[2] "Alumina SEM image," http : / / wwwen . uni . lu / media / images/, last accessed Apr 10, 2015.

[3] E. Dowgiallo and J. Hardin, "Perspective on ultracapacitors for electric vehicles," *IEEE Aerospace and Electronic Systems Magazine*, vol. 10, no. 8, pp. 26–31, 1995.

[4] J. Lee, A. Chemistruck, and G. Plett, "Discrete-time realization of transcendental impedance models, with application to modeling spherical solid diffusion," *Journal of Power Sources*, vol. 1, p. 134, 2012.

[5] "Basic construction of aluminum electrolytic capacitors," www . rubycon . co . jp / en / products / alumi / pdf / Construction . pdf, last accessed Mar 26, 2015.

[6] F. Posey and T. Morozumi, "Theory of potentiostatic and galvanostatic charging of the double layer in porous electrodes," *Journal of the Electrochemical Society*, vol. 113-2, pp. 176–184, 1966.

[7] A. Johnson and J. Newman, "Desalting by means of porous electrodes," *Journal of the Electrochemical Society*, vol. 118, pp. 510–517, Mar 1971.

[8] C. Fahramandi, "Method of making a high performance ultracapacitor," US Patent 6 059 847, 2000.

[9] H. Becker , "Low voltage electrolytic capacitor," US Patent 2 800 616, 1954.

[10] R. Rightmire, "Electrical energy storage apparatus," US Patent 3 288 641, 1966. [Online]. Available: {UnitedStatesPatent3 , 288 , 641}

[11] "A brief history of supercapacitors," www . cantecsystems . com / ccrdocs / brief-history-of-supercapacitors . pdf, last accessed Mar 30, 2015, August 2007.

[12] Tecate Group, "What is an ultracapacitor," http : / / www . tecategroup . com / app _ notes / 0 _ Tecate _ Group _ What % 20is % 20an % 20ultracapacitor . pdf, last accessed, 23 Apr, 2015.

[13] "Maxwell Product Guide," http : / / www . maxwell . com / products / ultracapacitors / docs / 1014627 _ boostcap _ product _ guide . pdf, last accessed, Jan 13, 2015.

[14] R. Signorelli, D. Ku, J. Kassakian, and J. Schindall, "Electrochemical double-layer capacitors using carbon nanotube electrode structures," *Proceedings of the IEEE.11*, vol. 11, pp. 1837–1847, 2009.

[15] P. Simon and A. Burke, "Nanostructured carbon double layer capacitance and more," *The Electrochemical Society Interface*, 2008.

[16] B. Conway, *Electrochemical Supercapacitors: Scientific Fundamentals and Technological Applications*. Springer US, 1999.

[17] E. Yanes, S. Grats, and A. Stalcup, "Tetraethylammonium tetrafluoroborate: a novel electrolyte," *The Royal Society of Chemistry*, vol. 125, pp. 1919–1923, 2000.

[18] A. Yoshida, K. Imoto, H. Yoneda, and A. Nishino, "An electric double-layer capacitor with high capacitance and low resistance." *IEEE Transactions on Components, Hybrids, and Manufacturing Technology*, vol. 15, pp. 133–138, 1992.

[19] M. UE, K. Ida, and S. Mori, "Electrochemical properties of organic liquid electrolytes based on quaternary ion salts for EDLCs," *Journal of Electrochemical Society*, vol. 141, no. 11, p. 2989, 1994.

[20] A. Schneuwly and R. Gallay, "Properties and applications of supercapacitors from the state-of-the-art to future trends," *Proceeding PCIM*, 2000.

[21] K. Tonurist, T. Thomberg, A. Janes, T. Romann, V. Sammelselg, and E. Lust, "Influence of separator properties on electrochemical performance of electrical double-layer capacitors," *Journal of Electroanalysis*, vol. 689, pp. 8–20, 2013.

[22] C. Lin, J. Ritter, and B. Popov, "A mathematical model of an electrochemical capacitor with double layer and faradaic processes," *Journal of the Electrochemical Society*, vol. 149, no. 9, pp. 3168–3175, 1999.

[23] H. Kim and B. Popov, "A mathematical model of oxide/carbon composite electrode for supercapacitors," *Journal of the Electrochemical Society*, vol. 150, no. 9, pp. A1153 – A1160, 2003.

[24] B. Conway, "Transition from supercapacitor to battery behavior in electrochemical energy storage," *Journal of the Electrochmical Society*, vol. 138-6, pp. 1539–1548, 1991.

[25] Maxwell Technologies, "Ultracapacitor safety data sheet (MSDS)," http : / / www . maxwell . com / products / ultracapacitors / downloads, last accessed, 23 Apr, 2015, 2013.

[26] "Acetonitrile," http : / / scorecard.goodguide.com/chemical-profiles/html/acetonitrile. html, last accessed Mar 18, 2015.

[27] C. Farahmandi, "A mathematical model of an electrochemical capacitor with porous electrodes," *Electrochemical Society Proceedings*, vol. 96-25, pp. 167–179, 1997.

[28] V. Srinivasan and J. Weidner, "Mathematical modeling of electrochemical capacitors," *Journal of the Electrochemical Society*, vol. 146, no. 5, pp. 1650–1658, 1999.

[29] J. Marie-Francoise, H. Gualous, and A. Berthon, "Supercapacitor thermal and electrical behavior modeling using ANN," *IEEE Proceedings. Electrical Power Applications*, vol. 153-2, pp. 255–261, 2006.

[30] R. Martin, J. Quintana, A. Ramos, and I. Nuez, "Modeling EDLCs, from classical to fractional impedance," *IEEE*, 2008.

[31] H. Helmholtz, "Some laws concerning the distribution of electric currents in volume conductors with applications to experiments on animal electricity." *Proceedings of the IEEE*, vol. 92, pp. 868–870, 1853, Reprinted in English, 2004.

[32] L. Patton and E. Zalta, "Hermann von Helmholtz," http : / / plato . stanford . edu / archives / fall2014 / entries / hermann-helmholtz/, last accessed 22 Apr, 2015, 2014.

[33] D. Chapman, "A contribution to the theory of electrocapillarity," *Philosophical Magazine Series 6*, vol. 25, pp. 475–481, 1913.

[34] G. Gouy, "Constitution of the electric charge at the surface of an electrolyte," *Journal of Physical Theory and Applications*, vol. 9, pp. 457–468, 1910.

[35] D. Grahame, "The electrical double layer and the theory of electrocapillarity," *Chemical Reviews*, vol. 41(3), pp. 441–501, Dec 1947.

[36] O. Stern, "The theory of the electrolytic double layer," *Elektrochemical Angew Physical Chemistry*, vol. 30, pp. 508–516, 1924.

[37] A. Yu, V. Chapot, and J. Zhang, *Electrochemical Supercapacitors for Energy Storage and Delivery.* CRC Press, 2013.

[38] J. Kang, J. Wen, S. Jayaram, A. Yu, and X. Wang, "Development of an equivalent circuit model for EDLCs with distinct electrolytes," *Electrochimica Acta*, vol. 115, pp. 587–598, 2014.

[39] J. Bockris, M. Devanthat, and K. Mueller, "On the structure of charge interfaces," *Proceedings of the Royal Society of London*, vol. 274, p. 55, 1963.

[40] L. Shi and M. Crow, "Comparison of ultracapacitor electric circuit models," *IEEE*, 2008.

[41] R. Spyker and R. Nelms, "Classical equivalent circuit parameters for a EDLC," *IEEE Transactions on Aerospace and Electronic Systems*, vol. 36, 2000.

[42] Gamry Instruments, "Application note on equivalent circuits," http : / / www . gamry . com / application-notes, last accessed, 22 Apr 2015.

[43] P. Zoltowski, "On the electrical capacitance of interfaces exhibiting constant phase element behavior," *Journal of Electoanalytical Chemistry*, vol. 443, no. 1, pp. 149–154, Feb 1998.

[44] J. Jorcin, M. Orazem, N. Pebere, and B. Tribollet, "CPE behavior by local electrochemical impedance spectroscopy," *Electrochimica Acta*, vol. 51, no. 8-9, pp. 1473–1479, Jan 2006.

[45] M. Abouzari, F. Befkemeier, G. Schmitz, and D. Wilmer, "On the physical intrepretation of constant phase elements," *Solid State Ionics*, vol. 180, pp. 922–927, 2009.

[46] J. Newman and W. Tiedemann, "Porous electrode theory with battery applications," *Journal of American Institute of Chemical Engineers*, vol. 21-1, pp. 25–41, 1975.

[47] W. Tiedemann and J. Newman, "Double layer capacity determination of porous electrodes," *Journal of Electrochemical Society*, vol. 1, pp. 70–74, 1975.

[48] T. Yeu and R. White, "Mathematical model of a lithium polypyrrole cell," *Journal of the Electrochemical Society*, vol. 137, no. 5, pp. 1327–1336, May 1990.

[49] L. Andrews, *Elementary Partial Differential Equations*. Academic College Press, 1986.

[50] B. Ho and R. Kalman, "Effective construction of linear state variable models from input/output functions," *Regelungstechnik*, vol. 14, no. 12, pp. 545–548, 1966.

[51] A. Namisnyk, "A survey of electrochemical supercapacitor technology," University of Technology, Sydney, Tech. Rep., 2013.

[52] M. Halper and J. Ellenbogen, "Supercapacitors: A brief overview," *Nanosystems Group, MITRE Corp.*, 2006.

[53] D. Lide, Ed., *CRC Handbook of Chemistry and Physics, 84thed.* CRC Press, 2003.

[54] J. Dean, *Lange's Handbook of Chemistry (15th)*. McGraw-Hill, 1999.

[55] Gamry Instruments., "Basics of Electrochemical Impedance Spectroscopy," http : / / www . gamry . com / application-notes /

basics-of-electrochemical-impedance-spectroscopy/, last accessed, 22 Apr, 2015, 2005.

[56] N. Cogger and N. Evans, "An introduction to electrochemical impedance measurement," http : / / www . solartronanalytical . com / literature / index . aspx, last accessed 22 Apr 2015, 1999.

[57] "Testing electrochemical capacitors, part I," http : / / www . gamry . com / application-notes/testing-electrochemical-capacitors-part-1-cyclic-voltammetry-and-leakage-current/, last accessed Apr 1, 2015.

[58] "Testing electrochemical capacitors, part II," http : / / www . gamry . com / application-notes/testing-electrochemical-capacitors-part-2-cyclic-charge-discharge-and-stacks/, last accessed Apr 1 2015.

[59] "Testing electrochemical capacitors, part III," http : / / www . gamry . com / application-notes/testing-electrochemical-capacitors-part-3-electrochemical-impedance-spectroscopy/ last accessed Apr 1, 2015.

[60] A. Lasia, B. Conway, J. Bockris, and R. White, "Electrochemical impedance spectroscopy and its applications," *Kluwer Academic-Plenum Publishers*, vol. 32, pp. 143–248, 1999.

[61] A. Lasia, "Modeling of impedance of porous electrodes," *Modern Aspects of Electrochemistry*, vol. 43, pp. 67–137, Aug 2008.

[62] F. Beguin and E. Frackowiac, Eds., *Supercapacitors: Materials, Systems and Applications*. Wiley-VCH, 2013.

[63] M. Lourakis, "A brief description of the Levenberg-Marquardt algorithm," www . ics . forth . gr / ~lourakis / levmar / levmar . pdf, last accessed 15 Mar, 2015, Feb 2005.

[64] Maxwell Technologies, "Test procedures for capacitance, ESR, leakage current and self discharge characterization of UltraCapacitors," http : / / www.maxwell.com / products / ultracapacitors / downloads, last accessed 22 Apr, 2015, 2013.

[65] C. Lin, H. Popov, and C. Ploehn, "Modeling the effects of electrode composition and pore structure on the operating performance of EDLCs," *Journal of the Electrochemical Society*, vol. 149, no. 2, pp. A167–A175, 2002.

[66] "Aluminum," http : // www.aqua-calc.com/page/density-table/substance/Aluminum, last accessed Apr 1, 2015.

[67] A. Pandolfo and A. Hollenkamp, "Carbon properties and their role in supercapacitors," *Journal of Power Sources*, vol. 157, pp. 11–27, 2006.

[68] E. Pollak, I. Genish, G. Salitra, and A. Soffer, "The dependence of the electronic conductivity of carbon colecular sieve electrodes on their charging states," *Journal of Physical Chemistry*, vol. 110, pp. 7443–7448, 2006.

[69] L. Wang, M. Toyoda, and M. Inagaki, "Dependence of electric double layer capacitance of activated carbons on the types of pores and their surface areas," *New Carbon Materials*, vol. 23, no. 2, pp. 111–115, 2008.

[70] Maxwell Technologies, "HC series ultracapacitor datasheet," http : // www.tecategroup. com / capacitors / datasheets / maxwell / HC _ series . pdf, last accessed, 22 Apr, 2015.

[71] H. Gualous, F. Rafik, R. Gallay, A. Crausaz, and A. Berthon, "Frequency, thermal and voltage supercapacitor characterization and modeling," *Journal of Power Sources*, vol. 165, pp. 928–934, 2006.

[72] J. Schiffer, D. Linzen, and D. Sauer, "Heat generation in double layer capacitors," *Journal of Power Sciences*, vol. 160, pp. 765–772, 2006.

[73] R. Buerschaper, "Thermal and electrical conductivity of graphite and carbon at low temperatures," *Journal of Applied Physics*, vol. 15, no. 452, 1944.

[74] A. Barroso-Bogeat, M. Alexandre-Franco, C. Gonzalez, A. Garcia, and V. Serrano, "Temperature dependance of the electrical conductivity of activated carbons prepared from vine shoots by physical and chemical activation methods," *Microporous and Mesoporous Materials*, vol. 209, pp. 90–98, 2015.

[75] A. d'Entremont and L. Pilon, "First order thermal model of commercial EDLCs," *Applied Thermal Engineering*, vol. 67, pp. 439–446, 2014.

[76] H. Wang and L. Pilon, "Accurate simulations of electric double layer capacitance of edlcs," *Journal of Physical Chemistry*, vol. 115, pp. 16 711–16 719, 2011.

[77] H. Gaulous, D. Bouquain, A. Berthon, and J. Kauffmann, "Experimental study of supercapacitor serial resistance and capacitance variations with temperature," *Journal of Power Sources*, vol. 123, pp. 86–93, 2003.

[78] G. Elert, "Resistivity of carbon, amorphous," http : // hypertextbook . com / facts / 2007 / DanaKlavansky . shtml, last accessed, Apr 10, 2015.

[79] B. Ravdel, K. Abraham, and R. and C. Marsh, "Temperature dependence of the conductivity of lithium-ion battery electrolytes," www . electrochem . org / dl / ma / 200 / pdfs / 0097 . pdf, last accessed, 22 Apr, 2015.

[80] Bibby Scientific, "The effect of temperature on conductivity measurement," http : // www . jenway . com / notes _ Conductivity _ Meters . asp, last accessed 22 Apr 2015.

List of Symbols, Abbreviations, and Acronyms

Abbreviations and Acronyms

BE-ROM   DRA implementation using the best available or estimated parametric data

BCAP   Commercially available Maxwell BoostCap 150 F EDLC

CB   Circuit Based

CPE   Constant Phase Element

DL   Double Layer

DRA   Discrete-time Realization Algorithm

EDL   Electric Double Layer, used interchangably with DL

EDLC   Electrochemical Double Layer Capacitor

EIS   Electrochemical Impedance Spectroscopy

ESR   Equivalent Series Resistance

EV   Electric Vehicle

FOM   Full Order Model

LMA   Levenberg-Marquardt Algorithm

M-ROM   DRA ROM implementation using measured EDLC values

PDE   Partial Differential Equation

ROM   Reduced Order Model

SVD   Singular Value Decomposition

T-ROM   DRA ROM implementation using theoretical or *guessed* values

List of Symbols

A Cross sectional area of electrode, m^2

a Interfacial surface area, or double layer surface area, of porous electrode, $m^2 m^{-3}$

C Capacitance per unit area, $F m^{-2}$

C Capacitance, F

C_{total} Total capacitance of an EDLC, F

d Thickness of dielectric in electrostatic capacitor, m

E Energy stored in a capacitor, J

F Farad

F Faraday's constant, $96\,487\,C\,mol^{-1}$

$H(s)$ Laplace domain transfer function

$H^*(s)$ Laplace domain transfer function with a pole at the origin removed

$h_d[n]$ Approximation to the continuous time impulse response at sample n (sampling period of T_1)

h_s Discrete-time system step response with sampling period of T_s.

h_{step} Approximation to the continuous-time step response (sampling period of T_1)

h_e Height of the electrode as physically measured, m

h_s Height of the electrode as physically measured, m

I_{cell} Cell current density, $\mathrm{A\,m^{-2}}$

I_{dc} Constant current, A

i_{app} Applied cell current, A

i Current, A

i_e Ionic current density in the solution phase of an electrode, $\mathrm{A\,m^{-2}}$

i_n Double layer current density per interfacial area, $\mathrm{A\,m^{-2}}$

i_s Electronic current density in the solid phase of an electrode, $\mathrm{A\,m^{-2}}$

L Length of the electrode, m

l_{e} Measured length of the BCAP's aluminum foil, double sided electrode, m

L_{sep} Length of the separator between electrodes, m

R_{i} EDLC total instantaneous resistance, Ω

R_{instant} EDLC instantaneous resistance of single electrode, Ω

R_{sep} Separator resistance, Ω

R_{ss} EDLC steady-state resistance, Ω

R_{steady} Resistance of EDLC electrodes, Ω

$\mathbf{res}_0$ Residue of poles of transfer function at $s = 0$

T Temperature, K

v_{cell} Voltage across an entire EDLC, V

v_{sep} Voltage across the separator, V

$v_{\text{electrode}}$ Voltage across a single electrode, V

w_{e} Width of the electrode as physically measured, m

w_s	Width of the separator as physically measured, m
x	l-d linear coordinate across the cell, m

Matrices

A	State transition matrix of the state-space model
B	Input matrix of the state-space model
C	Output matrix of the state-space model
D	Input-output coupling matrix of the state-space model
x	State of state-space model
y	Linear output of state-space model

Greek

ε	Term to denote volume percentage of solid or electrolyte in electrode, unitless
ϵ	Relative permittivity of material, unitless
ϕ_e	Potential in electrolyte region of electrode, V
ϕ_s	Potential in solid region of electrode, V
κ	Effective conductivity of electrolyte part of electrode, $\mathrm{S\,m^{-1}}$
κ_total	Total electrolyte conductivity in the EDLC, S
κ_sep	Effective conductivity of electrolyte in separator region, $\mathrm{S\,m^{-1}}$
$\kappa_\mathrm{s\text{-}tot}$	Effective conductivity of electrolyte in separator region, S
σ	Effective conductivity of solid part of electrode, $\mathrm{S\,m^{-1}}$
σ_total	Total solid conductivity in the EDLC, S

η Overpotential defined as $\eta(x,t) = \phi_s - \phi_e$, V

$\widetilde{\eta}$ Overpotential with initial condition $\eta(x,t) = \phi_s - \phi_e - \eta_0$, V

$\overline{\widetilde{\eta}}$ Overpotential in Laplace domain V